Three-Dimensional Microstructure of Solid Oxide Fuel Cell Anode: Observation, Quantification, and Application to Numerical Analysis

Masashi KISHIMOTO

2013

A dissertation submitted in partial fulfillment of the requirements
for the degree of Doctor of Philosophy

Department of Aeronautics and Astronautics
Graduate School of Engineering
Kyoto University

Contents

Acknowledgments

It is my great pleasure to express my sincere appreciation to all people who supported me throughout my Ph.D work in the Thermal Engineering Laboratory of Kyoto University.

First of all, my heartfelt appreciation goes to professor Hideo Yoshida, whose invaluable guidance and suggestion from his substantial experience greatly helped me to broaden my scope of interest and find clues to tackle with challenging issues. I am greatly indebt to associate professor Hiroshi Iwai for invaluable assistance and guidance from his sharp insights on the research topic, which were significantly helpful to deepen the discussion. I would also like to show my appreciations to assistant professor Motohiro Saito for his generous assistance and arrangement of the laboratory. Thanks are expressed here to the members of the Thermal Engineering Laboratory, particularly to Mr. Daisuke Hayashi, Mr. Ryo Tanaka, and Mr. Kosuke Miyawaki for research collaborations. The five-year academic life in the laboratory will definitely be my unforgettable memory.

I received generous support from professor Koichi Eguchi, associate professor Toshiaki Matsui, assistant professor Hiroki Muroyama, and the member of the Catalyst Design Engineering Laboratory in Kyoto University. The observation technique using the FIB-SEM system was developed mainly through the discussion with them. I would like to express my appreciation to Mr. Ryo Kishida, Mr. Yuichi Mikami, and Mr. Masaru Kubota for the maintenance management of the FIB-SEM system. Special thanks go to Dr. Hirofumi Sumi for the generous and useful advice in experiments. I owe a very important debt to professor Nobuhide Kasagi, Naoki Shikazono, and the member of the Frontier Energy Laboratory in the University of Tokyo. Their invaluable suggestions were really helpful to develop the numerical simulation model of SOFC anodes. Special thanks are also expressed here to associate professor Kyosuke Kishida in the Property Control of Crystaline Materials Labo-

ratory in Kyoto University, who gave me useful direction for the sample preparation in the FIB-SEM observation. I would also express my thanks to the alumnus of the Heat Transfer Laboratory of Kyoto University for their invaluable comments and advices in academic conferences and for the kind invitation to their laboratory.

Finally, I would like to express my heartfelt thanks to my family for their understanding, financial support, and constant encouragement throughout my study.

Chapter 1

Introduction

1.1 Background

Solid oxide fuel cells (SOFCs) are promising energy conversion systems because they can directly convert chemical energy of fuels into electrical energy in a highly-efficient manner. SOFCs are operated in relatively higher temperature compared with other types of fuel cells such as polymer electrolyte fuel cells (PEFCs) because commonly-used ceramic electrolyte shows sufficient ionic conductivity at more than about 600 °C. Such high operating temperature provides both advantages and disadvantages to the SOFCs. The main advantage is that they don't require precious catalyst such as platinum to enhance the electrochemical reaction in the electrodes, which can significantly reduce the production cost and give them strong competitiveness in the renewable energy market. Moreover, they can effectively use surplus heat generated from the system for combined heat and power (CHP) system and hydrogen production by steam reforming of various hydrocarbon fuels, which contribute to enhancing the total energy efficiency of the system. On the other hand, high temperature challenges a selection of the materials used in the system; conventional metal-based materials are not usually applicable. In addition, difference in heat expansion coefficients among the materials can distort the cell configuration, lowering the reliability of the system.

Through the decades of research and development assisted by Japanese government, SOFC systems finally appeared in the market in the last couple of years. In October 2011, JX Nippon Oil & Energy Co. produced a household-use SOFC system with a 700W stack module fueled by LP gas or city gas [1]. The total energy efficiency of 87% (LHV) was achieved with

the inclusion of the electricity generation efficiency of 45%. In April 2012, Osaka Gas Co. also produced a similar system with 700W SOFC module [2]. The total energy efficiency reaches to 90% (LHV) with the electricity generation efficiency of 46.5%. However, for the full-scale introduction of the SOFC systems to the renewable energy market, there still remains several issues to be overcome, such as the reduction of the initial purchasing cost and the guarantee of the long-term reliability.

Electrodes are the core components of SOFC systems and determine a great part of the system efficiency and reliability. They consist of porous materials, which often contain three phases: electron-conductive phase, oxide-ion conductive phase, and the pore phase for gas diffusion. The electrochemical reaction inside the electrodes is considered to occur around the three-phase boundary (TPB), which is the facing point of the three phases. Therefore, the electrodes are expected to contain as much TPB as possible to provide abundant electrochemical reaction site. At the same time, for the sufficient transport of chemical species to and from the TPB, contiguous pathways of the three phases need to be secured; the lack of any one of these pathways results in making the TPB inactive. Therefore, the microstructure of the porous electrodes has a critical impact on the performance of the electrodes.

Numerous researches have been conducted to optimize the electrode structure at nano- to meso-scale order. For example, optimization of the solid-phase compositions and the particle diameters are of great interest for achieving higher TPB density and better connectivity [3–5], which can be regarded as an optimization at a micro-scale order. At a nano-scale order, recent development of the impregnation technique has made it possible to introduce nanoparticles into the electrode structure, which can drastically increase the reaction site in the electrodes [6]. Meso-scale structure control such as the introduction of corrugated structures on the electrode-electrolyte interface is also employed to increase the volumetric current generation [7].

In addition, performance degradation, which is a significant barrier to the commercialization of the SOFCs, is often attributed to the morphologic changes in the porous structure, such as sintering/coarsening [8–10] and redox of metal catalysts [11–14], steam-anode interactions [15], deactivation of metal catalysts by impurities such as chromium and surfer [16, 17], and carbon deposition when hydrocarbon fuels are supplied [18–20]. Therefore, various degradation phenomena associated with the microstructural changes need to be con-

sidered in the attempt to optimize the porous electrodes.

Historically, the insights on the electrode microstructure had been bound to rely on two-dimensional cross-sectional microscope techniques such as scanning electron microscopy (SEM) and transparent electron microscopy (TEM). The obtained information was highly important for the microstructural optimization; however, it is essentially impossible to obtain three-dimensional information of the complex porous structure, such as connectivity of the porous components and the distribution of the TPB lines. Although there are several theories to predict the three-dimensional configuration of the porous structure from the two-dimensional images, such as those based on the concept of contiguity [21–23], they require assumptions for structural configuration; and hence, cannot precisely predict the three-dimensional configuration of the porous components. Consequently, any analysis based on such models inevitably includes some extent of uncertainty associated with the structure model.

Recently, development of state-of-the-art tomography techniques such as focused ion beam and scanning electron microscopy (FIB-SEM) and X-ray computed tomography (XCT) enables the direct observation of the three-dimensional microstructure of the porous electrodes at nano-scale resolution. In the FIB-SEM, the focused ion beam (FIB) is used to conduct a nano-scale sectioning of a target volume followed by an image acquisition with the scanning electron microscope (SEM). Repetition of the FIB milling and the SEM observation provides a sequential set of images of a target volume, which can be reconstructed into three-dimensional microstructure of the porous electrodes. The first application of the FIB tomography to SOFC electrodes was reported by Wilson et al. [24], who demonstrated the potential of the technique for the characterization of the real porous microstructure such as phase connectivity, tortuosity factor, and the distribution of the TPB lines. The paper posed a significant impact on the SOFC community and the application of the FIB technique has been rapidly increasing in the recent years [25–28]. The quantitative data evaluated from the three-dimensional microstructure are expected to be the key to investigating the relationships between the porous microstructure and the performance/durability of the SOFC electrodes; and hence, the optimization of the porous structure can be significantly promoted.

As one of the applications of the obtained three-dimensional microstructure, development

of a reliable simulation technique is strongly required to investigate the microstructural effect on the performance and degradation. Detailed information inside the complex porous structure, such as the distribution of the gas concentration and the charge-transfer current can be obtained, some of which are not accessible in experiments. From the parametric study on various operating conditions and microstructural parameters, rate-limiting process in the SOFC electrodes can be identified, which are significantly valuable in optimizing the cell configuration and the electrode microstructure. Before the three-dimensional structure became available, almost all of the numerical models were bound to rely on porous models [29–31]. As a result, the numerical model contains uncertainty in the applicability of the porous models as well as that of the transport and electrochemical models, which makes it difficult to validate the numerical model as a whole. Thus, the recent advances in the three-dimensional observation techniques are highly expected to exclude the uncertainty of the structure model and increase the reliability on the simulation model.

The main objective of this study is summarized into three parts: (i) direct observation of the three-dimensional microstructure of the SOFC anode using the FIB-SEM technique and development of the quantification methods for characterizing the obtained porous microstructure, (ii) development of a reliable simulation technique using the obtained microstructure, and (iii) application of the developed simulation model to predict the anode performance and to propose a optimization policy for the anode fabrication.

1.2 Outline of the Thesis

Chapter 2 presents the state-of-the-art tomography technique for the observation of SOFC electrodes using the FIB-SEM system. Image processing techniques to handle the obtained SEM images and the quantification methods for characterizing the three-dimensional porous structure are also proposed.

Chapter 3 presents the one-dimensional numerical simulation of the porous anodes with the microstructural parameters obtained in chapter 2. The validity of the proposed model is investigated through the comparison with experimental results under various operating conditions. For the fundamental understanding of the effect of the microstructure on the anode performance, sensitivity analysis is conducted using the proposed model.

Chapter 4 presents the development of a fundamental technique required for the three-dimensional numerical simulation in porous structures. Structure models are developed to maintain the quality of the original structural information obtained with the FIB-SEM in the grid system. The effect of the models on the numerical simulation is investigated through a diffusion analysis, and their effect and applicability are evaluated.

Chapter 5 presents the effect of the composition ratio of Ni-YSZ anodes on the anode performance through electrochemical characterization, microstructural analysis, and three-dimensional numerical simulation. A simple optimizing policy for SOFC anodes is proposed through the discussion.

Chapter 6 presents the study aiming to predict the active thickness in the porous anodes. The characteristic length with respect to the oxide-ion conduction, which is defined by the ratio between the effective oxide-ion conductivity and the electrochemical reaction rate, is introduced as a key parameter to predict the thickness of the active thickness. The relationships between the characteristic length and the active thickness is investigated thought the one-dimensional numerical analysis.

Chapter 7 summarizes the major conclusions of this study and offers suggestions for future works.

Bibliography

[1] JX Nippon Oil & Energy Co., Press release, http://www.noe.jx-group.co.jp/newsrelease/2011/20110915_01_0950261.html

[2] Osaka Gas Co., Ltd., Press release, http://www.osakagas.co.jp/company/press/pr_2012/1196121_5712.html

[3] J.H. Lee, H. Moon, H.W. Lee, J. Kim, J.D. Kim, K.-H. Yoon, Quantitative Analysis of Microstructure and its Related Electrical Property of SOFC Anode, Ni-YSZ Cermet, *Solid State Ionics* **148** (2002) 15–26.

[4] L. Holzer, B. Münch, B. Iwanschitz, M. Cantoni, Th. Hocker, Th. Graule, Quantitative Relationships Between Composition, Particle Size, Triple Phase Boundary Length and Surface Area in Nickel-Cermet Anodes for Solid Oxide Fuel Cells, *Journal of Power Sources* **196** (2011) 7076–7089.

[5] J.H. Yu, G.W. Park, S. Lee, S.K. Woo, Microstructural Effects on the Electrical and Mechanical Properties of Ni-YSZ Cermet for SOFC Anode, *Journal of Power Sources* **163** (2007) 926–932.

[6] S.P. Jiang, Nanoscale and Nano-Structured Electrodes of Solid Oxide Fuel Cells by Infiltration: Advances and Challenges, *International Journal of Hydrogen Energy* **37** (2012) 449–470.

[7] A. Konno, H. Iwai, M. Saito, H. Yoshida, A Corrugated Mesoscale Structure on Electrode-Electrolyte Interface for Enhancing Cell Performance in Anode-Supported SOFC, *Journal of Power Sources* **196** (2011) 7442–7449.

[8] L. Holzer, B. Iwanschitz, Th. Hocker, B. Münch, M. Prestat, D. Wiedenmann, U. Vogt, P. Holtappels, J. Sfeir, A. Mai, Th. Graule, Microstructure Degradation of Cermet Anodes for Solid Oxide Fuel Cells: Quantification of Nickel Grain Growth in Dry and in Humid Atmospheres, *Journal of Power Sources* **296** (2011) 1279–1294.

[9] M.H. Pihlatie, A. Kaiser, M. Mogensen, M. Chen, Electrical Conductivity of Ni-YSZ

Composites: Degradation Due to Ni Particle Growth, *Solid State Ionics* **189** (2011) 82–90.

[10] M. Shah, P.W. Voorhees, S.A. Barnett, Time-Dependent Performance Changes in LSCF-Infiltrated SOFC Cathodes: The Role of Nano-Particle Coarsening, *Solid State Ionics* **187** (2011) 64–67.

[11] M. Pihlatie, A. Kaiser, M. Mogensen, Redox Stability of SOFC: Thermal Analysis of Ni-YSZ Composites, *Solid State Ionics* **180** (2009) 1100–1112.

[12] H. Sumi, R. Kishida, J.Y. Kim, H. Muroyama, T. Matsui, K. Eguchi, Correlation Between Microstructural and Electrochemical Characteristics during Redox Cycles for Ni-YSZ Anode of SOFCs, *Journal of The Electrochemical Society* **157**(12) B1747–B1752.

[13] H. Monzón, M.A. Laguna-Bercero, Redox-Cycling Studies of Anode-Supported Microtubular Solid Oxide Fuel Cells, *International Journal of Hydrogen Energy* **37** (2012) 7262–7270.

[14] P.R. Shearing, R.S. Bradley, J. Gelb, F. Tariq, P.J. Withers, N.P. Brandon, Exploring Microstructural Changes Associated with Oxidation in Ni-YSZ SOFC Electrodes Using High Resolution X-ray Computed Tomography, *Solid State Ionics* **216** (2012) 69–72.

[15] T. Matsui, R. Kishida, J.Y. Kim, H. Muroyama, K. Eguchi, Performance Deterioration of Ni-YSZ Anode Induced by Electrochemically Generated Steam in Solid Oxide Fuel Cells, *Journal of The Electrochemical Society* **157**(5) (2010) B776–B781.

[16] K. Haga, S. Adachi, Y. Shiratori, K. Itoh, K. Sasaki, Poisoning of SOFC Anodes by Various Fuel Impurities, *Solid State Ionics* **179** (2008) 1427–1431.

[17] K. Sasaki, K. Haga, T. Yoshizumi, D. Minematsu, E. Yuki, R. Liu, C. Uryu, T. Oshima, T. Ogura, Y. Shiratori, K. Ito, M. Koyama, K. Yokomoto, Chemical Durability of Solid Oxide Fuel Cells: Influence of Impurities on Long-Term Performance, *Journal of Power Sources* **196** (2011) 9130–9140.

[18] H. He, J.M. Vohs, R.J. Gorte, Carbonaceous Ceposits in Direct Utilization Hydrocarbon SOFC Anode, *Journal of Power Sources* **144** (2005) 135–140.

[19] V. Alzate-Restrepo, J.M. Hill, Effect of Anodic Polarization on Carbon Deposition on Ni/YSZ Anodes Exposed to Methane, *Applied Catalysis A: General* **342** (2008) 49–55.

[20] H. Sumi, P. Puengjinda, H. Muroyama, T. Matsui, K. Eguchi, Effects of Crystal Structure of Yttria- and Scandia-Stabilized Zirconia in Nickel-Based SOFC Anodes on Carbon Deposition and Oxidation Behavior, *Journal of Power Sources* **196** (2011) 6048–6054.

[21] J. Gurland, The Measurement of Grain Contiguity in Two-Phase Alloys, *Transactions of the Metallurgical Society of AIME* **212** (1958) 452–455.

[22] Z. Fan, A.P. Miodownik, P. Tsakiropoulos, Microstructural Characterization of Two Phase Materials, *Material Science and Technology* **9** (1993) 1094–1100.

[23] K.R. Lee, S.H. Choi, J. Kim, H.W. Lee, J.H. Lee, Viable Image Analyzing Method to Characterize the Microstructure and the Properties of the Ni/YSZ Cermet Anode of SOFC, *Journal of Power Sources* **140** (2005) 226–234.

[24] J.R. Wilson, W. Kobsiriphat, R. Mendoza, H.Y. Chen, J.M. Hiller, D.J. Miller, K. Thornton, P.W. Voorhees, S.B. Adler, S.A. Barnett, Three-Dimensional Reconstruction of a Solid-Oxide Fuel-Cell Anode, *Nature Materials* **5** (2006) 541–544.

[25] P.R. Shearing, J. Golbert, R.J. Chater, N.P. Brandon, 3D Reconstruction of SOFC Anodes Using a Focused Ion Beam Lift-Out Technique, *Chemical Engineering Science* **64** (2009) 3928–3933.

[26] H. Iwai, N. Shikazono, T. Matsui, H. Teshima, M. Kishimoto, R. Kishida, D. Hayashi, K Matsuzaki, D. Kanno, M. Saito, H. Muroyama, K. Eguchi, N. Kasagi, H. Yoshida, Quantification of SOFC Anode Microstructure Based on Dual Beam FIB-SEM Technique, *Journal of Power Sources* **195** (2010) 955–961.

[27] D. Gostovic, J.R. Smith, D.P. Kundinger, K.S. Jones, E.D. Wachsman, Three-Dimensional Reconstruction of Porous LSCF Cathodes, *Electrochemical and Solid-State Letters* **10**(12) (2007) B214–B217.

[28] N. Vivet, S. Chupin, E. Estrade, T. Piquero, P.L. Pommier, D. Rochais, E. Bruneton,

3D Microstructural Characterization of a Solid Oxide Fuel Cell Anode Reconstructed by Focused Ion Beam Tomography, *Journal of Power Sources* **196** (2011) 7541–7549.

[29] J.H. Nam, D.H. Jeon, A Comprehensive Micro-Scale Model for Transport and Reaction in Intermediate Temperature Solid Oxide Fuel Cells, *Electrochimica Acta* **51** (2006) 3446–3460.

[30] H. Zhu, R.J. Kee, Modeling Distributed Charge-Transfer Processes in SOFC Membrane Electrode Assemblies, *Journal of The Electrochemical Society* **155**(7) (2008) B715–B729.

[31] D. Chen, W. Bi, W. Kong, Z. Lin, Combined micro-scale and macro-scale modeling of the composite electrode of a solid oxide fuel cell, *Journal of Power Sources* **195** (2010) 6598–6610.

Chapter 2

Direct Three-Dimensional Observation of SOFC Anodes with Focused Ion Beam and Scanning Electron Microscope Technique

2.1 Introduction

Conventional electrodes used for SOFCs are composite porous material consisting of electron-conductive phase, oxide-ion-conductive phase, and gas-diffusive phase. The electrochemical reaction in the electrodes is considered to occur around the contact area of the three phases, which is called thee-phase boundary (TPB). The highly complex nature of the porous structure allows the active reaction site to spread into the electrode bulk, increasing the volumetric current generation.

The composite electrodes have several requirement for reliable operation. First, they must be thermally and chemically stable during long-time operation, which is usually under high temperature and strongly reducing or oxidizing atmosphere. Second, they should match the thermal expansion coefficient to the electrolyte material to prevent mechanical failure during thermal cycling in start-up/shut-down sequences. Third, they should have enough tolerance to various impurities in the supplied gas, such as sulfur and chlorine. Finally, cost issue is also significant considering the current economic situation and the competition against other energy devices.

In order to satisfy these requirements, not only the development of new materials but also

the optimization of the porous microstructure has been of great interest to manufacturers of the SOFCs. To achieve higher activity for the electrochemical reaction, electrodes are expected to contain as much TPB as possible providing abundant reaction site. However, not all TPB can work as a reaction site; for the sufficient transport of chemical species to and from the TPB, contiguous pathways of the porous components must be secured. Fig. 2.1 schematically shows the electrochemical reaction in the Ni-YSZ anode associated with the transport of various chemical species. For the delivery of the fuel to the TPB and the evacuation of the gaseous reactants, the contiguous pore network is required from the anode surface. Similarly, a connected pathway of the electron-conductive Ni phase is required from the TPB to the anode surface to lead the generated electrons to the external circuit via the current collector. Moreover, a percolation of the ion-conducting YSZ phase is also necessary from the anode-electrolyte interface. The lack of any one of these results in making the TPB inactive. It is obvious that the influence of the electrode microstructure on SOFC performance is significantly large; numerous research efforts have been devoted to find the optimal microstructure of the electrodes to achieve higher performance and longer durability.

Historically, the attempts to optimize the electrode microstructure had highly depended on trial-and-error-based experiments because the insight on the microstructure was confined to the conventional cross-sectional observation [1, 2]. Since the three-dimensional information of the real electrodes was not easily accessible, various porous models were developed to mimic the three-dimensional porous structure, such as the general effective media (GEM) theory [3], the concept of contiguity [4–6], the random-resistor network model [7, 8], the random-packing-spherical model [9, 10], and the stochastic reconstruction method [12]. These models played an important role for qualitative investigation of the porous electrodes through simulating various transport and electrochemical reaction in the model structures [10–12]. However, the limitations of these models are obvious because they require assumptions for structural configuration such as homogeneous and monodispersed particles. Therefore, they cannot precisely predict the states of the three-dimensional percolation of the porous components, which is highly important to consider the electrochemical activity of the TPB.

Recently, with state-of-the-art tomography techniques such as focused ion beam and scanning electron microscopy (FIB-SEM), three-dimensional microstructure of the porous

electrodes can be obtained at nano-scale resolution. Focused ion beam (FIB) tomography uses an ion beam to conduct a nano-scale sectioning of a target volume followed by an image acquisition with an scanning electron microscope (SEM). Repetition of the FIB milling and the SEM observation provides a sequential set of images of a sample volume, which can be reconstructed into three-dimensional microstructure of the porous electrodes. The quantitative data obtained from the three-dimensional structure are expected to be the key to investigating the relationships between the porous microstructure and the electrode performance; and hence, the optimization of the porous structure can be significantly promoted. The strong potential of this tomography technique has been attracting great interest from the researchers in the SOFC community [13–17].

In the present chapter, direct observation technique using the FIB-SEM system and following image processing and quantification techniques employed to the three-dimensional microstructure of the SOFC anodes will be presented. First, the mechanical configuration and the observation procedures with the FIB-SEM system will be explained. Next, the image processing procedure for image alignment, segmentation, and three-dimensional reconstruction will be presented. Then, various technique to quantify microstructural parameters that characterize the porous structure, such as volume fraction, percolation probability, tortuosity factor, and TPB density will be proposed. Finally, the results for four different Ni-YSZ anodes will be presented and compared for the fundamental understanding of the complex nature of the porous anodes.

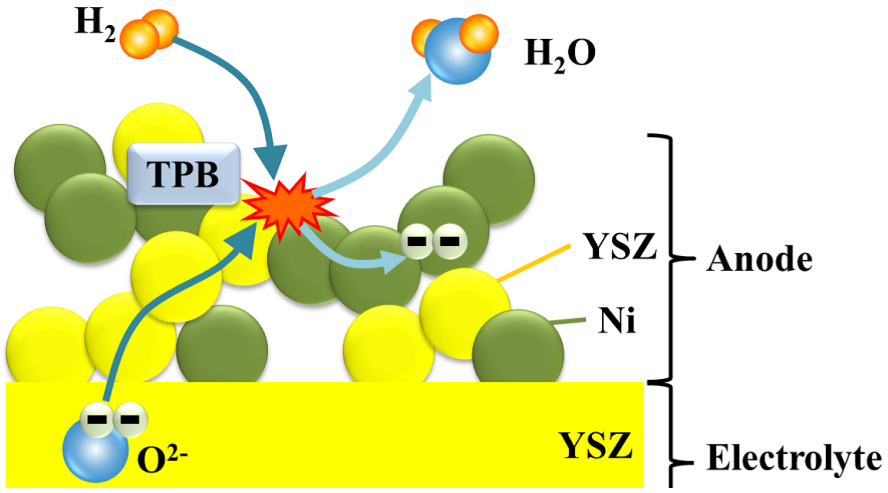

Fig. 2.1. Transport phenomena and electrochemical reaction in Ni-YSZ anode.

2.2 Direct Observation of Three-Dimensional Microstructure of SOFC Anode

2.2.1 Sample preparation

In this study, a conventional Ni-YSZ|YSZ|LSM button cell is examined. Fig. 2.2 shows the schematic picture of the SOFC button cell used in this study. A disk of 8 mol% YSZ (yttria-stabilized zirconia, Tosoh Co., 24 mm in diameter, 500 μm in thickness) is used as an electrolyte. The Ni-YSZ anode is fabricated on the YSZ disk as follows.

1. NiO powder (Wako Pure Chemical Industries, Ltd.) and YSZ powder (Tosoh Co.) are mixed with zirconia balls (ϕ4.0mm) and ball-milled for 24 h along with ethanol to disperse the particles.
2. The ethanol is evaporated using a hot stirrer, and the resultant powder is pre-sintered at 1400 °C for 5 h.
3. Pre-sintered powder is ground with an automatic milling equipment for 3 h.
4. Carbon black (Asahi Carbon Co., SB300) is used as a pore former for some of the anode samples; in such cases, the above wet milling process is repeated.
5. The resultant powder is mixed with polyethylene glycol to form a slurry.
6. The slurry is screen-printed on the YSZ electrolyte and sintered at 1400 °C for 5 h.

In this study, four different anodes are fabricated: Ni:YSZ = 70:30, 50:50, and 30:70 without pore former, and Ni:YSZ = 50:50 with pore former.

$(La_{0.8}Sr_{0.2})_{0.97}MnO_3$ (LSM) is used as a cathode material, which is fabricated on the other face of the YSZ disk as follows.

1. Metal acetates are dissolved in water considering the required molar ratio of the metals.
2. The water is dried off using a hot stirrer, followed by the calcination at 300 °C for 1 h.
3. Ball-milling with zirconia balls (ϕ4.0 mm) for 24 h.
4. The resultant powder is mixed with polyethylene glycol to form a slurry.
5. The slurry is screen-printed on the other face of the electrolyte and sintered at 1150 °C for 5 h.

A platinum wire (ϕ0.2mm) is attached around the side edge of the electrolyte disk to use it as a reference electrode.

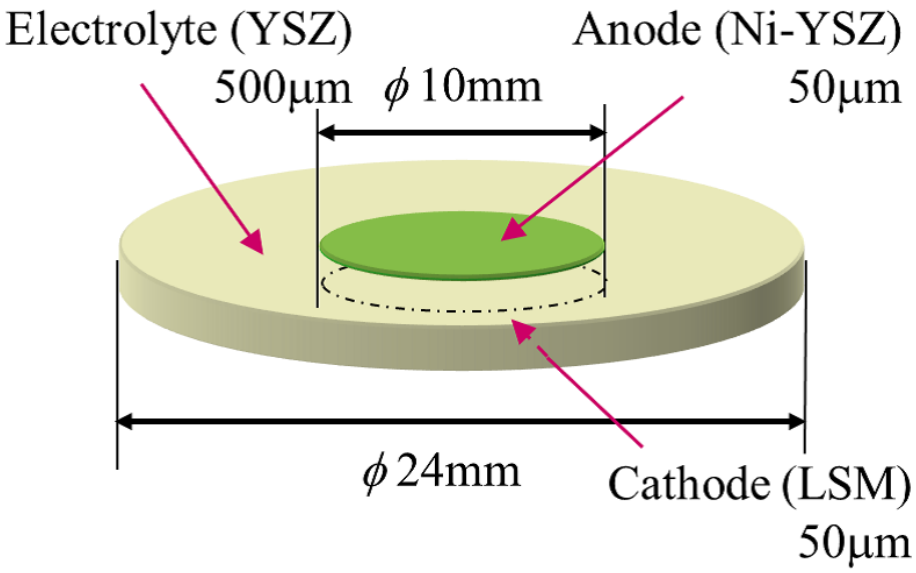

Fig. 2.2. Schematic picture of the SOFC button cell.

2.2.2 Electrochemical characterization

Schematic picture of the experimental setup for the electrochemical measurement of the button cells is shown in Fig. 2.3. First, the cell is sandwiched by alumina tubes with Pyrex glass rings, and heated up to the testing temperature by an electric furnace. Second, the anode is reduced under hydrogen atmosphere at 1000 °C for 1 h. Third, the power generation with potentiostatic load is conducted for 3 h at the terminal voltage 0.7 V to stabilize the initial performance. Feeding gas is humidified hydrogen (3% H_2O – 97% H_2) and air (79% N_2 – 21% O_2) to the anode and cathode, respectively. A total gas flow rate is 100 ml/min at both electrode sides. The fuel mixture is prepared by bubbling hydrogen through water, whose temperature is precisely controlled with an electric heater. Finally, under various fuel and temperature conditions, current-voltage characteristics and AC impedance characteristics are measured between the anode and the reference electrode using the Solartron 1287 electrochemical interface and the Solartron 1255 frequency analyzer. The applied frequency is in the range of 0.1 Hz to 1 MHz.

2.2.3 FIB-SEM observation

After the electrochemical characterization, the cell is cooled down in a reductive atmosphere. Then, the porous anode is infiltrated with epoxy resin (Marumoto Struers KK)

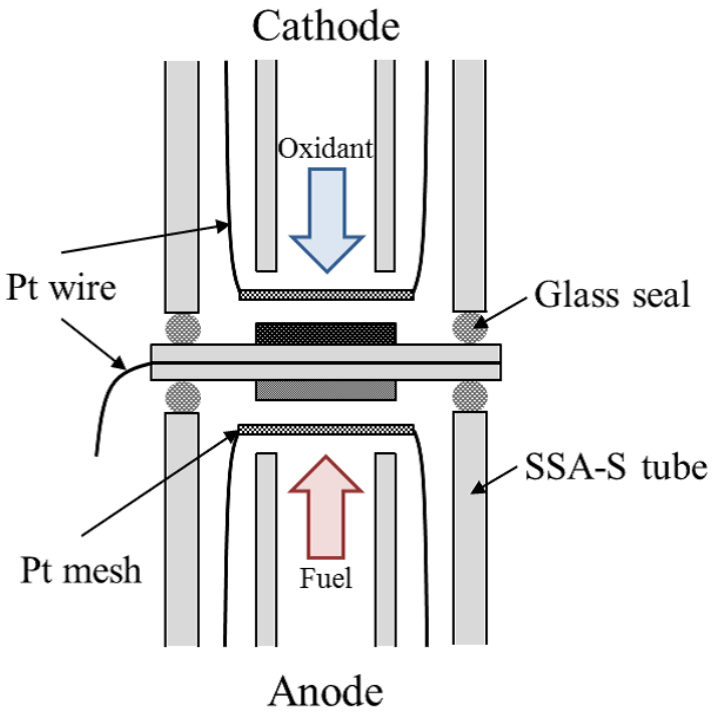

Fig. 2.3. Schematic picture of the experimental setup.

under vacuum condition so that the pores of the anode can be easily distinguished during the SEM observation. The infiltrated samples are cut and mechanically polished with sandpaper and diamond paste to prepare them for the FIB-SEM observation. Fig. 2.4(a) shows the prepared specimen for the FIB-SEM observation, where the transparent material is the epoxy resin. Fig. 2.4(b) shows the specimen setup on the microscope stage. To prevent the charge-up during the observation, the excessive part of the epoxy is removed as much as possible. Moreover, the specimen surface is coated with silver paste (Fujikura Kasei Co. Ltd, DOTITE D-500) to improve the electric conductivity of the specimen.

The three-dimensional microstructure of the Ni-YSZ anode is observed by the FIB-SEM system (NVision 40), which is equipped with a Gemini FE-SEM column (Zeiss), a zeta FIB column (SIINT), and a multichannel gas injection system (SIINT). Fig. 2.5 schematically shows a typical setting for the FIB-SEM observation. In this system, two beams have a coincident angle of 54°. An in-lens secondary electron detector is used for the microstructural observation with an acceleration voltage around 2 kV. Fig. 2.6 shows an example of the obtained cross-sectional images. Under the above imaging condition, a clear contrast

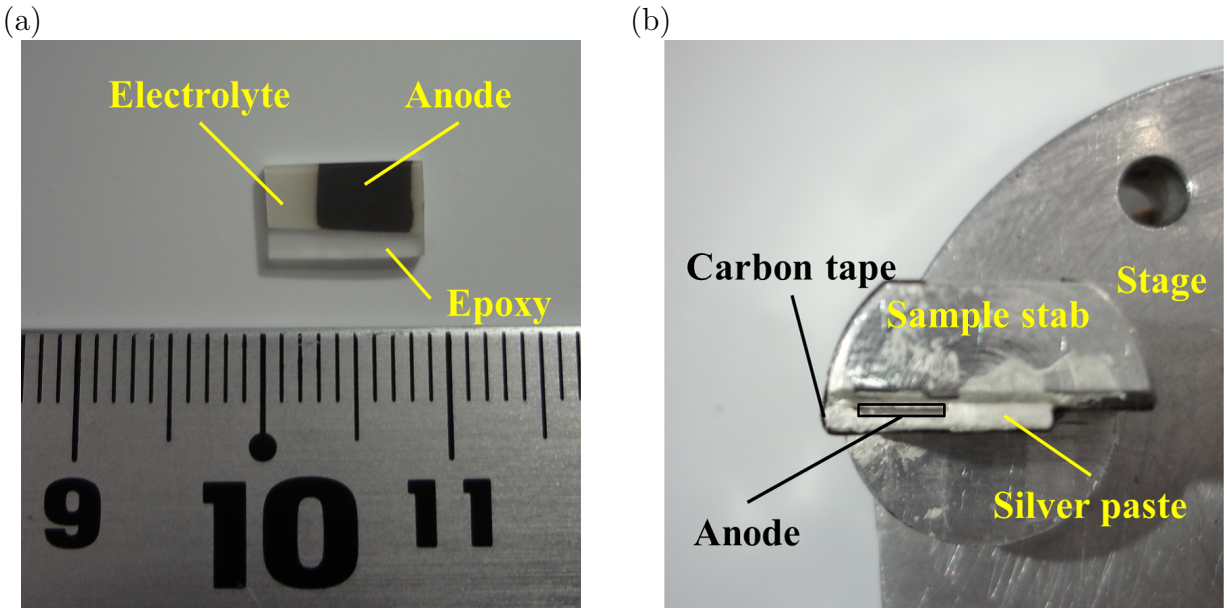

Fig. 2.4. Specimen preparation. (a) Infiltrated and polished anode. (b) setup on the stab.

between the three phases is successfully obtained. In the image, white, gray, and black part corresponds to the Ni, YSZ, and the pore phase, respectively. The charge-up of a sample often becomes an issue because it causes drifting of a target volume in the field of view. Therefore, in addition to the careful sample preparation, carbon is deposited on top of the specimen so that the charge species can be easily removed from the target volume. However, it is still difficult to completely eliminate the drifting; there are always small misalignment between the neighboring images. Therefore, lines are put on the sample surface to use them for an alignment mark in the following image processing.

As the first step in the image processing, misalignments are corrected by minimizing the difference between the neighboring images. Then, regions available for the microstructural analysis is extracted and the segmentation is conducted based on the image brightness. After the alignment and the segmentation, the sequential set of the two-dimensional images is lined up with the actual increment during the FIB-SEM observation and the three-dimensional porous microstructure is reconstructed in a virtual field. A commercial image processing software Avizo (Mercury Computer Systems, Inc.) is used for the image alignment, segmentation, three-dimensional reconstruction, and some of the quantification explained afterward. In this study, orthogonal coordinate axes X and Y are embedded on the two-dimensional SEM image and Z is the proceeding direction of the FIB milling.

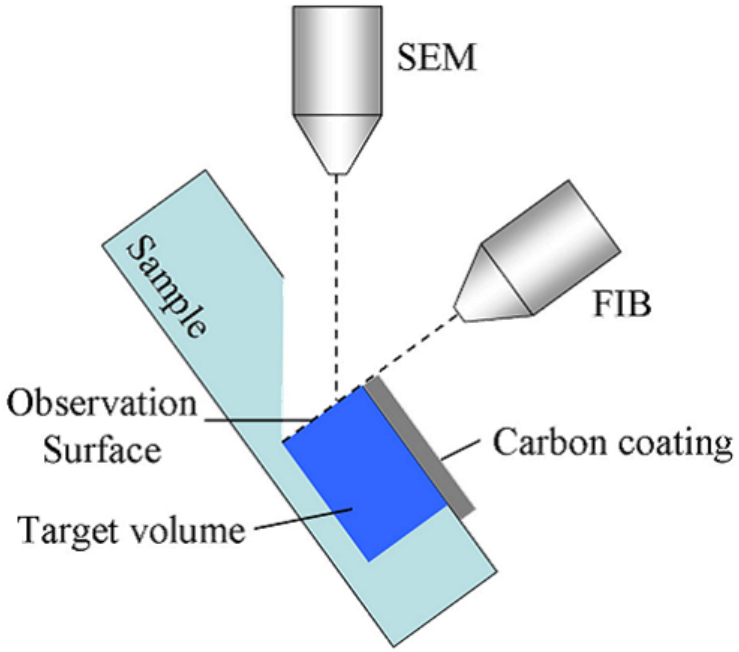

Fig. 2.5. Schematic diagram of the FIB-SEM setting.

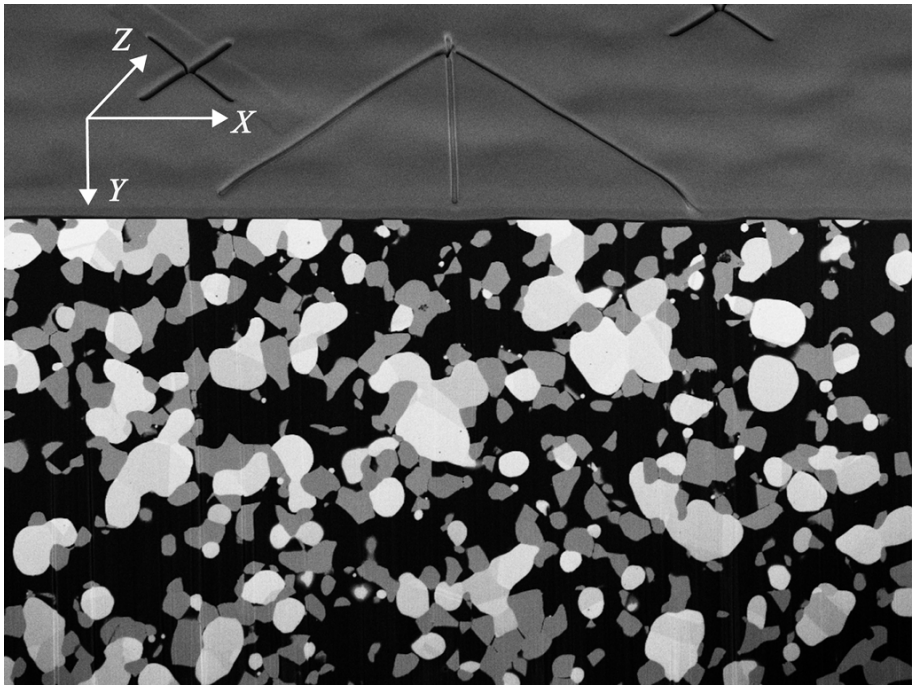

Fig. 2.6. Example of the cross-sectional images obtained with the FIB-SEM. Ni:YSZ = 50:50 (PF) anode. (White: Ni, gray: YSZ, black: pore)

2.3 Quantification of Porous Structure

From the phase-separated images, various microstructural parameters that characterize the porous structure are quantified. They are expected to be the keys to considering the relationships between the electrode microstructure and the electrode performance/durability. For the quantification, in-house code based on the C language is used as well as the commercial software Avizo.

2.3.1 Volume fraction

Volume fraction is the primary information of porous materials and has strong relationships with other microstructural parameters. The number of voxels corresponding to each phase are counted and divided by the total number of volxels in the whole region.

$$V_l = \frac{Vol_l}{Vol_{\mathrm{all}}} \tag{2.1}$$

where V_l is the volume fraction of phase l, and Vol is the volume.

2.3.2 Percolation probability

For the sufficient transport of the chemical species to and from the TPB, contagious pathways of the porous components are required. Therefore, the connectivity of the porous components are significantly important to explain the electrode performance, and hence, should be improved for the microstructural optimization. In this study, the percolation probability of phase l, Q_l, is defined as the volume percentage of the region that penetrates the cuboid sample volume in a specific direction so that the anisotropic aspect of porous structures can be detected.

$$Q_l^{\mathrm{eff}} = \frac{V_l^{\mathrm{eff}}}{V_l} \tag{2.2}$$

where the superscript eff indicates the penetrating region.

2.3.3 Tortuosity factor

In porous materials, the amount of transport though the complex structure are generally reduced compared with that through bulk material. It is primarily caused by the decrease of the conductive volume but that is not the only reason; the structural complexity of the

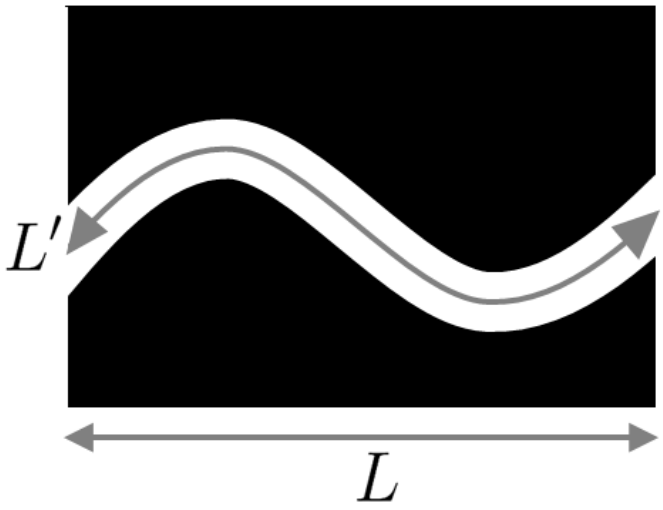

Fig. 2.7. Simple curved channel for the explanation of tortuosity and tortuosity factor.

phase should also be considered. The effective transport coefficients can generally be written as follows:

$$\Gamma_l^{\text{eff}} = \frac{V_l}{\tau_l}\Gamma_l \tag{2.3}$$

where τ_l is the tortuosity factor of phase l, and Γ_l is the bulk transport coefficient.

It should be kept in mind that "tortuosity factor" and "tortuosity" are different concepts. For a simple explanation, a curved channel as depicted in Fig. 2.7 is used here. The "tortuosity" is defined as the ratio of the length of the curved channel, L', to that of the straight channel, L. On the other hand, the "tortuosity factor" in this example is the square of the tortuosity. What can be applied to eq. (2.3) is the tortuosity factor, although it is almost impossible to clearly define the length of the highly branched transport pathways in real porous materials.

The tortuosity factor can be quantitatively evaluated through a random-walk process [18], simplified diffusion simulation. In the first step of the method, a large number of imaginary particles are randomly distributed in the considered phase, i.e., the Ni, YSZ, or pore phase. Each walker randomly chooses one of the neighboring voxels as its possible location in the next time step. If the selected neighboring voxel is the same as the considered phase, the walker migrates to that voxel. If the selected voxel is a different phase, the walker stays at the current voxel and waits for the next time step. In this procedure, neither absorption nor desorption on the phase boundaries is considered. While repeating this process, the mean

square displacement of the random walkers is calculated as follows:

$$\langle r^2(t)\rangle = \frac{1}{N}\sum_{n=1}^{N}\left[\{x_n(t)-x_n(0)\}^2+\{y_n(t)-y_n(0)\}^2+\{z_n(t)-z_n(0)\}^2\right] \tag{2.4}$$

where N is the total number of random walkers, and $x_n(t)$, $y_n(t)$, and $z_n(t)$ are the three-dimensional coordinates of the walker's position at time t for the nth walker. $\langle\ \rangle$ indicates an ensemble average over all the walkers. Since the mean square displacement $\langle r^2\rangle$ is proportional to time, the transport coefficient of the imaginary particles is related to the time derivative of $\langle r^2\rangle$ and the volume fraction of the phase:

$$\Gamma_l = V_l\frac{1}{6}\frac{d\langle r^2(t)\rangle_l}{dt} \tag{2.5}$$

The mean square displacement in porous media is lower than that obtained in a bulk space because the movement of the particles is interrupted at the phase boundaries. The degree of the reduction is measured quantitatively using the tortuosity factor as follows:

$$\tau_l = \frac{\Gamma_{\text{bulk}}}{\Gamma_l^{\text{eff}}/V_l} = \frac{V_l}{V_l^{\text{eff}}}\frac{d\langle r^2(t)\rangle_{\text{bulk}}}{dt}\Big/\frac{d\langle r^2(t)\rangle_l}{dt} \tag{2.6}$$

where Γ_l^{eff} and V_l^{eff} are the effective transport coefficient and the volume fraction of the penetrating region, respectively. It should be noted that the random walkers are distributed only in the penetrating region of the phase because the isolated region cannot contribute to the transport phenomena. Otherwise, random walkers are trapped in the isolated region, resulting in the underestimation of the mean square displacement. In order to capture an anisotropic aspects of the porous structure, the mean square displacement $\langle r^2\rangle$ can be divided into the directional mean square displacements $\langle x^2\rangle$, $\langle y^2\rangle$, and $\langle z^2\rangle$ as follows:

$$\langle x^2(t)\rangle = \frac{1}{N}\sum_{n=1}^{N}\{x_n(t)-x_n(0)\}^2 \tag{2.7}$$

$$\langle y^2(t)\rangle = \frac{1}{N}\sum_{n=1}^{N}\{y_n(t)-y_n(0)\}^2 \tag{2.8}$$

$$\langle z^2(t)\rangle = \frac{1}{N}\sum_{n=1}^{N}\{z_n(t)-z_n(0)\}^2 \tag{2.9}$$

The anisotropic tortuosity factors are calculated with similar relations, eqs. (2.5) and (2.6).

In order to obtain an accurate value of tortuosity factors, a long time step and a large number of walkers are necessary. However, as the time step proceeds, random walkers are

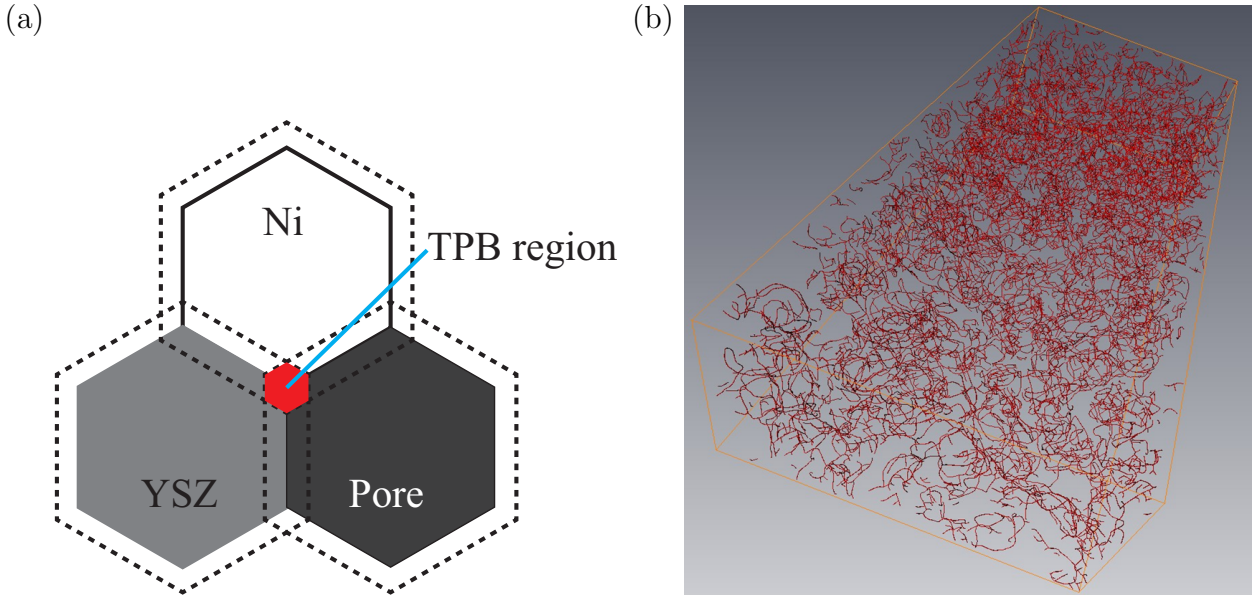

Fig. 2.8. Schematic picture of the volume-expansion method. (a) Extraction of the TPB existing region. (b) Overview of the reconstructed TPB lines.

likely to step out of the image dataset obtained with the FIB-SEM. Therefore, a mirror symmetric boundary condition is applied to solve this problem because it guarantees connectivity of the porous components across the boundaries of the dataset.

For the random numbers, "SIMD-oriented Fast Mersenne Twister (SFMT)" [19] is used as a high performance pseudo-random number generator to meet the requirement for high-dimensional randomness.

2.3.4 Three-phase boundary density

The volume-expansion method is developed and adopted to the evaluation of the TPB using the commercial image processing software Avizo. Schematic picture of the method is depicted in Fig. 2.8(a). First, three phases in the segmented images are slightly expanded outward in the virtual field, and the overlapped regions, which has string-like volumes and contains TPB line inside, are extracted. Then, centerlines of the strings are reconstructed to represent the TPB lines (Fig. 2.8(b)). The total length of the lines are measured and divided by the sample volume to obtain the TPB density. It is worth noting that lines obtained through this method theoretically match the actual TPB lines if the spatial resolution of the images is sufficiently high and the amount of the volume-expansion is infinitely small.

2.3.5 Surface-to-volume ratio

Surface-to-volume ratio $(S/V)_l$ is an important factor particularly in heat transfer and chemical reactions in porous materials. The larger the parameter, the larger surface is included in the porous media, which may result in more heat exchange and surface reaction on the surface. At the same time, a larger surface-to-volume ratio implies complex porous structure, limiting the transport through the phase.

The surface area of the complex porous materials can be obtained with the Avizo, however, it inevitably includes the surface on the boundary of the observed region, which is not an actual surface of the porous material. Therefore, the boundary surface is measured by using an in-house code and subtracted to obtain the surface area that is truly included in the observed region. Then, it is divided by the phase volume to obtain the surface-to-volume ratio.

$$(S/V)_l = \frac{S_l}{Vol_l} \tag{2.10}$$

It should be noted that the surface-to-volume ratio $(S/V)_l$ is different from the "specific surface" S_l^V. In the latter case, the denominator of the ratio is the total volume of the cuboid region instead of that of the considered phase.

$$S_l^V = \frac{S_l}{Vol_{\mathrm{all}}} \tag{2.11}$$

Although both parameters can be used to characterize the porous structure in terms of how large surface area is included in the volume, their meaning are different.

2.3.6 Particle/pore size distribution

Particle/pore size distributions (PSD) are evaluated by the line-intercept method, which was originally developed for quantifying a porous microstructure from a cross-sectional image [1, 2, 20, 21]. In this study, the method is expanded to apply it to three-dimensional structures. Lines are drawn in three directions along the orthogonal coordinate from the focused voxel. The lengths of the lines intercepted by the considered phase are measured and averaged to obtain the local particle/pore diameter (Fig. 2.9).

$$d = \frac{1}{3}\left(r_{x+} + r_{x-} + r_{y+} + r_{y-} + r_{z+} + r_{z-}\right) \tag{2.12}$$

Then the histogram of the local particle/pore size is obtained. Since the total number of voxels contained in a dataset depends on the samples, the histogram is normalized by the total number of voxels to make the comparison between different samples easier.

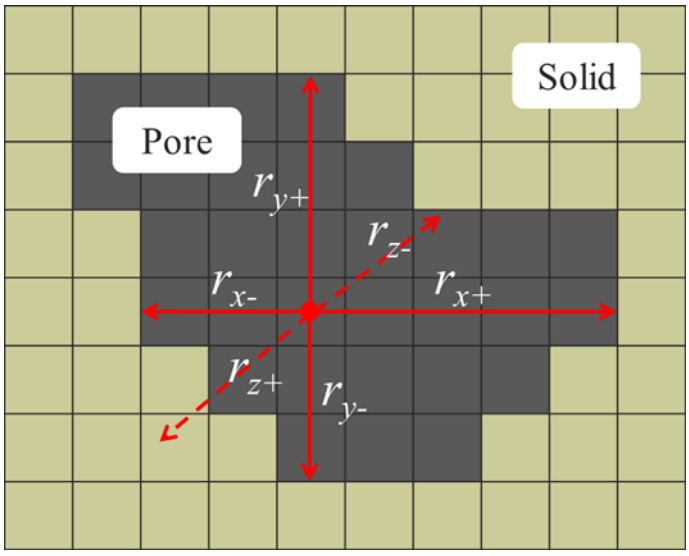

Fig. 2.9. Schematic picture of the line-intercept method.

2.4 Results and Discussion

In this chapter, four different anodes are examined; Ni:YSZ = 70:30, 50:50, and 30:70 without pore former and Ni:YSZ = 50:50 with pore former (PF). Fig. 2.10 shows the example of the segmented images and the three-dimensionally reconstructed structures of the anodes.

2.4.1 Sample sizes and voxel sizes

Table 2.1 shows the sample sizes and voxel sizes of the images extracted from the original SEM images. The sample sizes are around 10 μm in each direction except Z direction in the Ni:YSZ = 50:50 (PF) anode. The elemental voxel size is around 30 nm on the cross-sectional images and 50 nm in the increment direction of the FIB milling.

Table 2.1. Sample sizes and voxel sizes.

	Sample size [μm]			Voxel size [nm]		
Sample	X	Y	Z	X	Y	Z
Ni:YSZ = 70:30	18.0	13.2	10.5	30.0	30.0	52.3
Ni:YSZ = 50:50	18.1	9.72	9.97	34.7	34.7	62.3
Ni:YSZ = 50:50 (PF)	19.2	8.51	6.20	26.6	26.6	62.0
Ni:YSZ = 30:70	18.8	11.6	10.1	36.2	36.2	42.2

2.4.2 Volume fraction

Volume fractions of the porous components in the examined anodes are shown in Table 2.2. The quantified volume ratios of Ni:YSZ show good agreement with the intended values. Slight discrepancies implies that a larger sample volume is preferred for statistically estimated parameters to be representative of the whole anode microstructure.

Table 2.2. Volume fraction.

Sample	Ni	YSZ	Pore	Ni:YSZ
Ni:YSZ = 70:30	42.3	18.9	38.8	69.1:30.9
Ni:YSZ = 50:50	34.2	29.7	36.1	53.5:46.5
Ni:YSZ = 50:50 (PF)	25.3	25.1	49.6	50.2:49.8
Ni:YSZ = 30:70	23.6	50.6	25.8	31.8:68.2

(a) Ni:YSZ = 70:30

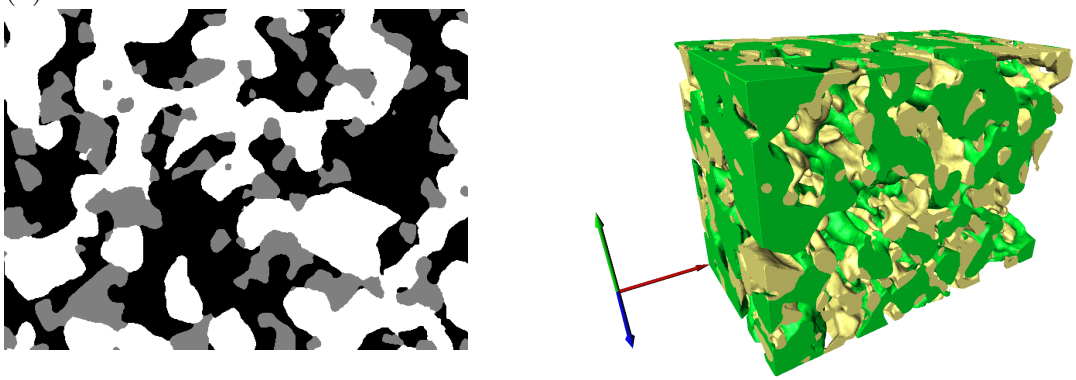

(b) Ni:YSZ = 50:50

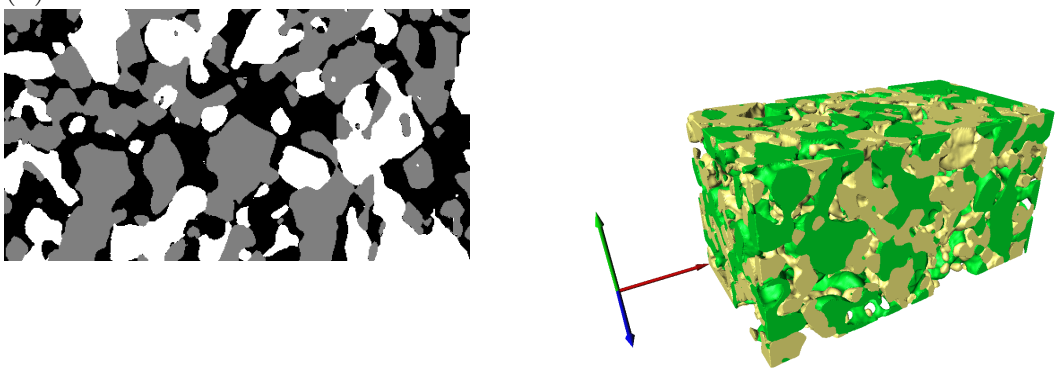

(c) Ni:YSZ = 50:50 (PF)

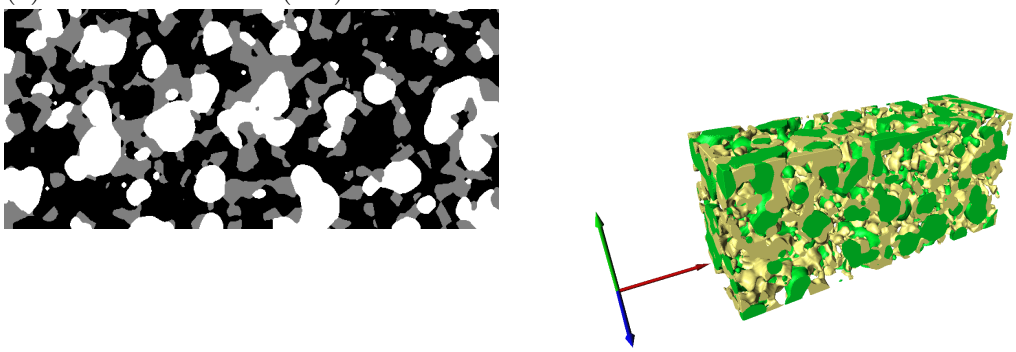

(d) Ni:YSZ = 30:70

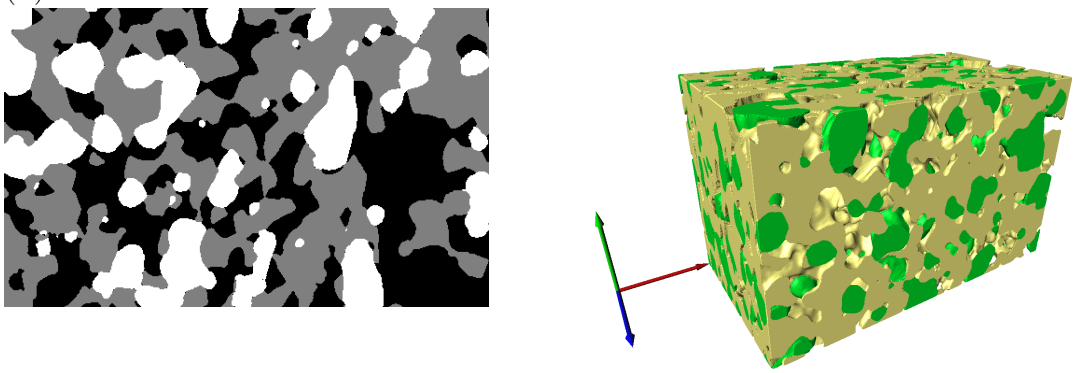

Fig. 2.10. Example of the segmented images and three-dimensionally reconstructed structure. (a) Ni:YSZ = 70:30, (b) Ni:YSZ = 50:50, (c) Ni:YSZ = 50:50 (PF), and (d) Ni:YSZ = 30:70.

2.4.3 Percolation probability

Percolation probabilities are shown in Table 2.3. In the examined anodes, some of the phases show poor connectivity: YSZ phase in the Ni:YSZ = 70:30 anode, Ni phase in the Ni:YSZ = 50:50 (PF) anode, and Ni phase in the Ni:YSZ = 30:70 anode. This is mainly due to their relatively lower volume fractions, 18.9, 25.3, and 23.6%, respectively. However, the YSZ phase in the Ni:YSZ = 50:50 (PF) anode shows good connectivity even though its volume fraction is comparably low (25.1 %). On the basis of the percolation theory [9, 10], a percolation probability steeply declines at a certain value of the volume fraction, which is called the percolation threshold. For binary mixture of uniform-size particles, it is about 30 %; however, it significantly differs if the particle size ratio between the two solid phases are not unity. As shown in Table 2.2, the volume fractions of the Ni and YSZ in the Ni:YSZ = 50:50 (PF) anode take similar values. Nevertheless the percolation probabilities of these two phases are significantly different as shown in Table 2.3: the Ni phase shows a poor connectivity while the YSZ phase is connected well. It implies the difference in the microstructure between the two phases. Details will be discussed later along with other microstructural parameters.

Table 2.3. Percolation probability.

	Ni			YSZ			Pore		
Sample	X	Y	Z	X	Y	Z	X	Y	Z
Ni:YSZ = 70:30	0.988	0.988	0.988	0.000	0.000	0.681	0.997	0.997	0.997
Ni:YSZ = 50:50	0.987	0.987	0.987	0.961	0.961	0.961	0.886	0.996	0.996
Ni:YSZ = 50:50 (PF)	0.477	0.477	0.842	0.943	0.943	0.943	1.000	1.000	1.000
Ni:YSZ = 30:70	0.000	0.155	0.000	1.000	1.000	1.000	1.000	0.986	0.986

2.4.4 Tortuosity factor

The accuracy of the random-walk simulation is examined by applying it to a well-defined structure shown in Fig. 2.11(a); an inclined straight channel is formed in the computational domain. The tortuosity factor in X-direction, τ_X, can be theoretically calculated in this case as $\tau_X = 1 + \tan^2\theta$, where θ is the inclination angle. τ_X is calculated varying the channel width W and the inclination angle θ. The results are compared with the theoretical values in Fig. 2.11(b). The discrepancy from the theoretical values becomes larger with larger inclination angle when W is small. It can be seen that the tortuosity factor is overestimated

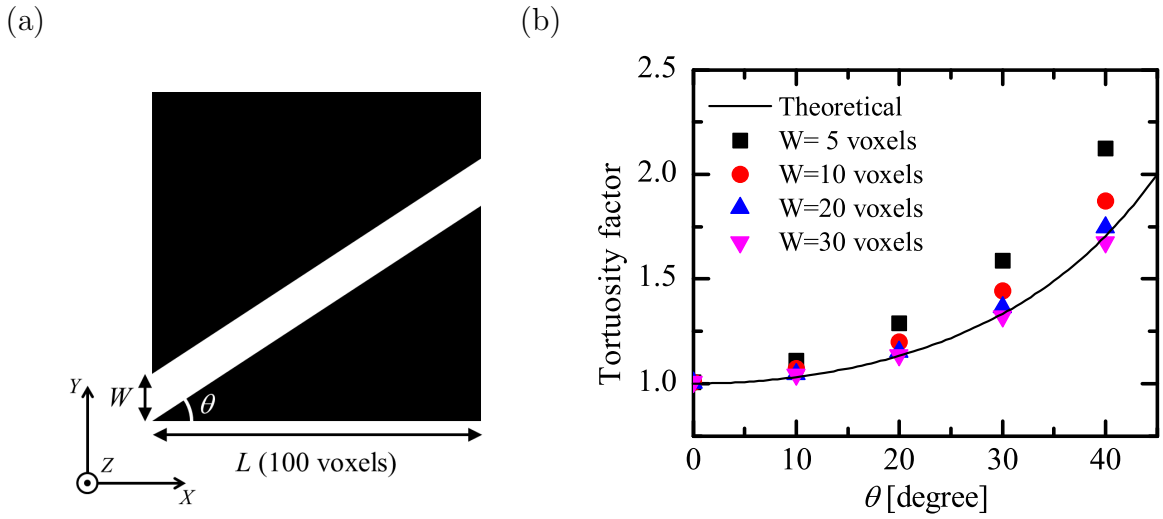

Fig. 2.11. Validation of the random-walk simulation with a well-defined problem: (a) the problem settings for the validation and (b) comparison with the theoretical value under various conditions.

when the spatial resolution is insufficient. It can be concluded from the result that this method provides reasonable values for tortuosity factors when the characteristic structure is resoluted with more than 20 voxels in each direction.

The directional mean square displacements in the Ni phase of the Ni:YSZ = 50:50 (PF) are shown in Fig. 2.12 as a typical result of the random-walk simulation, where the total number of random walkers is 10^5 and the total time step is 10^7. Theoretically, the directional mean square displacements in the free space are $\langle x^2 \rangle = \langle y^2 \rangle = \langle z^2 \rangle = t/3$. However, those in porous media are smaller than those in the free space because the movement of the particles is interrupted by the obstruction effect of the phase boundaries. The anisotropic tortuosity factors of each phase are shown in Table 2.4. In calculating the time derivatives of the mean square displacements, the first half of the total time step is omitted to eliminate the influence of the initial position of the particles. In some of the phases, it is impossible to calculate the anisotropic tortuosity factor because there is no percolating region in a specific direction.

Fig. 2.13 shows the relationships between the tortuosity factor and the phase volume fraction. It can be seen that the tortuosity factors steeply increase as the volume fraction becomes smaller, particularly under the percolation threshold located around the volume fraction of 25 %. It is consistent with the definition of the tortuosity factor shown in eq.(2.6) because it explicitly includes the inverse of the percolation probability.

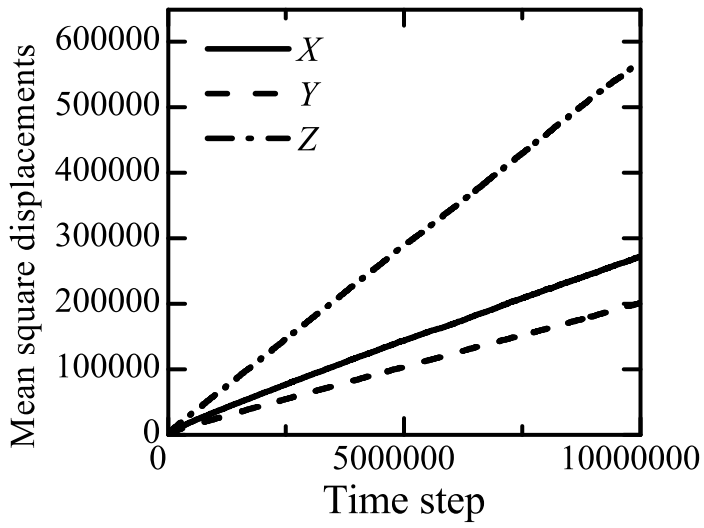

Fig. 2.12. Directional mean square displacements of the random walkers in the Ni phase of the Ni:YSZ = 50:50 (PF) anode.

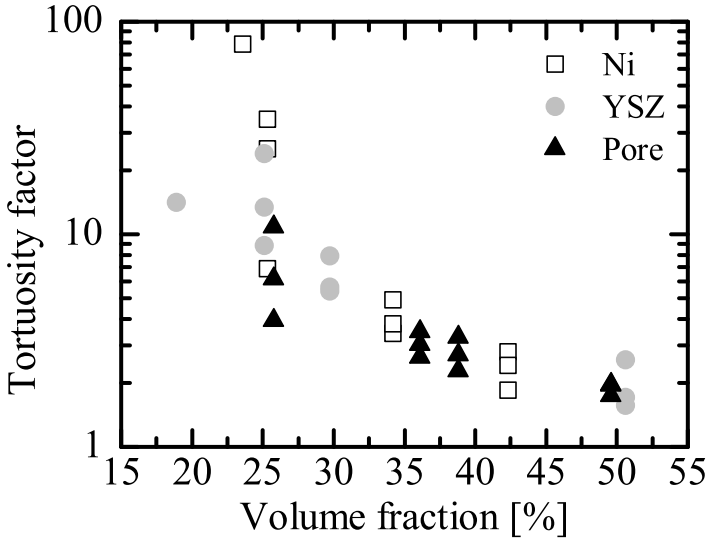

Fig. 2.13. Relationships between the tortuosity factor and the phase volume fraction.

Table 2.4. Anisotropic tortuosity factor.

	Ni			YSZ			Pore		
Sample	X	Y	Z	X	Y	Z	X	Y	Z
Ni:YSZ = 70:30	2.79	2.41	1.85	–	–	14.1	3.26	2.71	2.27
Ni:YSZ = 50:50	4.91	3.43	3.79	7.93	5.63	5.39	3.48	3.04	2.64
Ni:YSZ = 50:50 (PF)	25.2	34.8	6.91	24.0	13.4	8.85	1.95	1.97	1.74
Ni:YSZ = 30:70	–	78.3	–	1.71	1.57	2.57	6.17	3.92	10.8

2.4.5 TPB density

The validity of the volume-expansion method is examined by applying it to a well-defined structure. Fig. 2.14(a) shows the geometry adopted for the test calculation; two spheres, each representing one phase, are partially overlapped with each other and surrounded by the third phase. A circular-shape TPB is formed around the contact area of the two solid particles. The volume-expansion method is applied to this problem varying the spatial resolution of the structure. Fig. 2.14(b) shows the comparison between the obtained values and the theoretical values. It can be concluded from the figure that this method provides reasonable results for structures that have a characteristic length greater than 10 voxels.

The TPB density of each sample is shown in Table 2.5. The TPB density tends to be larger when the volume fractions of the Ni and YSZ phases are equivalent, which is also seen in the random-packing model based on the percolation theory [9, 10]. However, there is also a significant difference between Ni:YSZ = 50:50 and Ni:YSZ = 50:50 (PF) anodes. Even though the particles are more dispersed in the Ni:YSZ = 50:50 (PF) anode because of the higher pore volume fraction, the TPB density is still higher. This implies the particle size of the Ni:YSZ = 50:50 (PF) anode is smaller than that of the Ni:YSZ = 50:50 anode, which will be confirmed later.

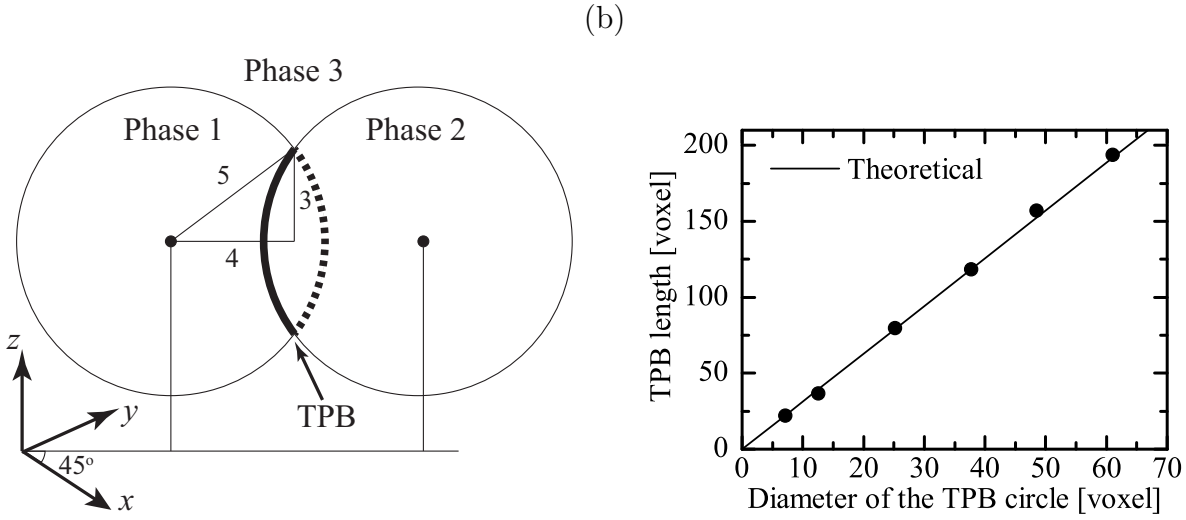

Fig. 2.14. Validation of the volume-expansion method with a well-defined problem: (a) test geometry for the validation and (b) comparison with the theoretical value at various spacial resolutions.

Table 2.5. TPB density. [μm/μm^3]

Sample	
Ni:YSZ = 70:30	1.77
Ni:YSZ = 50:50	2.00
Ni:YSZ = 50:50 (PF)	2.49
Ni:YSZ = 30:70	1.81

2.4.6 Surface-to-volume ratio

Surface-to-volume ratios of each phase are shown in Table 2.6. Also Fig. 2.15 shows the relationships between the surface-to-volume ratio and the phase volume fraction. The values have a slightly negative correlation with the volume fraction. However, the absolute value of the parameter seems to depend on the phase; the value of the YSZ phase is larger than that of the Ni phase when the volume fractions of the two phases are similar.

The microstructural characteristics of the Ni and YSZ phases in the Ni:YSZ = 50:50 (PF) anode is particularly interesting to discuss. Even though they have almost identical volume fraction, the surface-to-volume ratio of the Ni phase is about half of that of the YSZ phase. Moreover, both have larger tortuosity factors compared with the pore phase. The surface-to-volume ratio is useful to explain this issue. If the volume fraction of a phase is relatively small and fixed, a small surface-to-volume ratio indicates a situation where relatively large particles are sparsely distributed in the field, which results in limited connectivity between the particles. This is the case with the Ni phase showing the poor connectivity, and hence the large tortuosity factors. On the other hand, the YSZ phase has a larger surface-to-volume ratio than the Ni phase, but their volume fractions are similar. Considering the good connectivity of the YSZ phase, the YSZ phase is likely to have a smaller structure and is more uniformly distributed in the field. This geometric characteristics of the YSZ phase causes the complexity of the microstructural configuration and limits the transport through the phase, resulting in the large tortuosity factors.

Table 2.6. Surface-to-volume ratio. [μm^2/μm^3]

Sample	Ni	YSZ	Pore
Ni:YSZ = 70:30	2.21	5.34	3.40
Ni:YSZ = 50:50	3.98	5.24	5.17
Ni:YSZ = 50:50 (PF)	3.56	7.51	4.25
Ni:YSZ = 30:70	4.30	3.51	5.43

The above discussion shows that, for a given volume fraction, both very large and very small surface-to-volume ratios may result in large tortuosity factors; there seems to be an appropriate range of surface-to-volume ratio for achieving effective transport in the porous structure. Note that this appropriate range depends on the phase volume fraction.

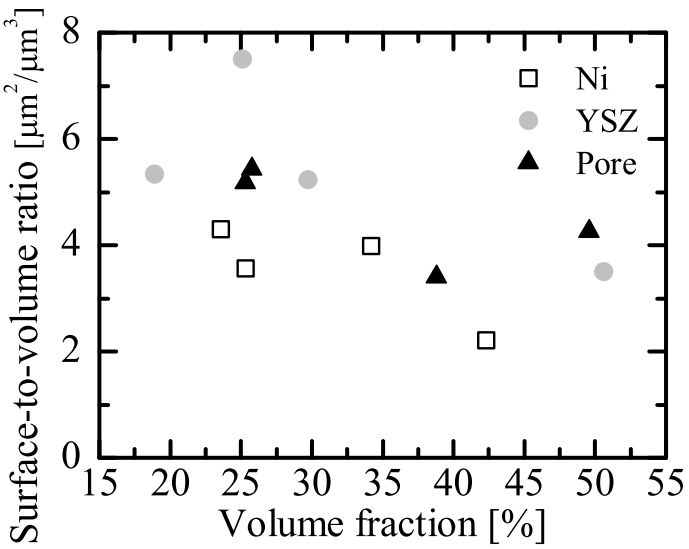

Fig. 2.15. Relationships between the surface-to-volume ratio and the phase volume fraction.

2.4.7 Particle/pore size

Table 2.7 shows the averaged particle/pore sizes of each phase with their standard deviations in parenthesis. Also Fig. 2.16 shows the particle/pore size distributions (PSD) of each phase. The particle/pore sizes are measured at all voxels corresponding to the considered phase and summarized into histograms. Then, the intensity of the histograms is normalized by the total number of voxels corresponding to the phase.

The average particle sizes of the Ni and YSZ phases tend to be larger when the volume fraction of the phase is larger. This is because larger volume fraction indicates more possibility of the sintering between the particles. In such a case, the shape of the PSD gradually becomes lower and wider as the volume fraction becomes higher. The PSD of the pore phase is affected by the Ni volume fraction as well as the addition of the pore former. Higher Ni content causes more volumetric shrinkage in the reduction process, which increases the pore size and widens the PSD of the phase. On the other hand, the pore former creates pores with similar sizes, resulting in relatively narrower PSD.

The effect of the pore former is worth discussing. The average pore size is affected by the addition of the pore former as discussed above. Another important effect of the pore former is that it can inhibit the sintering of the solid particles. The comparison of the PSD of the Ni phase between the Ni:YSZ = 50:50 (PF) and Ni:YSZ = 30:70 anodes clearly demonstrates this effect. Even though they have more than 10 % difference in their volume fraction, their PSD are almost identical. Also, the average particle size of the YSZ phase in the Ni:YSZ = 50:50 (PF) is significantly smaller than those of the other samples, which cannot be explained only by their volume fractions.

Table 2.7. Average particle/pore sizes [μm] and their standard deviations in parenthesis.

Sample	Ni		YSZ		Pore	
Ni:YSZ = 70:30	2.55	(1.05)	1.11	(0.51)	2.19	(1.20)
Ni:YSZ = 50:50	1.60	(0.77)	1.16	(0.56)	1.32	(0.73)
Ni:YSZ = 50:50 (PF)	1.38	(0.54)	0.73	(0.30)	1.74	(0.86)
Ni:YSZ = 30:70	1.34	(0.58)	1.74	(0.73)	1.39	(0.98)

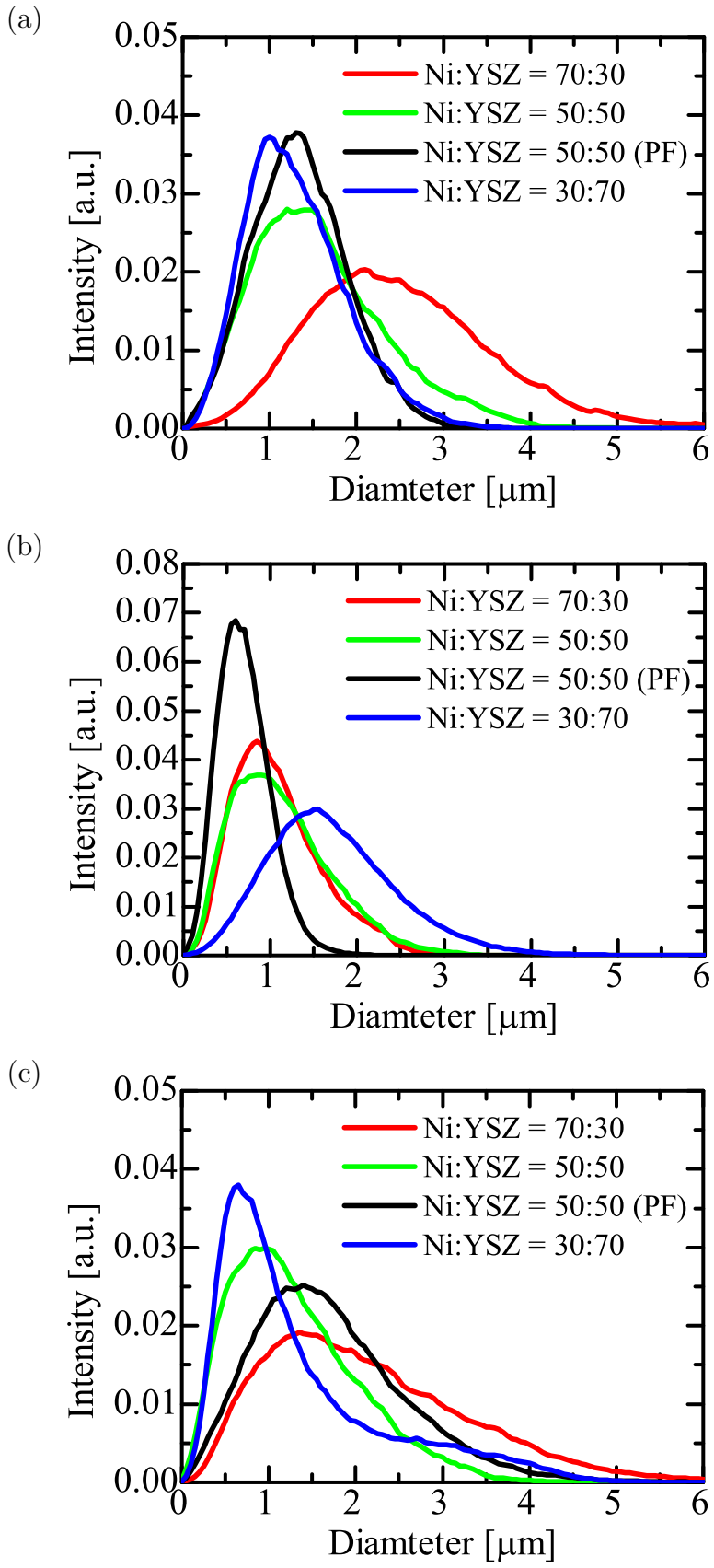

Fig. 2.16. Particle/pore size distributions. (a) Ni, (b) YSZ, and (c) Pore.

2.4.8 Error assessment

Quantification errors in the microstructural parameters are inevitable because of several issues: limited sample size and resolutions in the FIB-SEM observation, uncertainty in the image processing such as the alignment and segmentation, and the accuracy of the quantification methods themselves applied to the image data.

Since the volume fractions of the observed anodes well agree with the intended values (Table 2.2), the structure sizes are judged to be large enough to be representative of the whole anode structure; the influence of the structural inhomogeneity on the quantified parameters is limited. However, Kanno et al. [22] reported that larger volume is required for the accurate quantification of tortuosity factors. Among the tested samples, the Ni:YSZ = 50:50 (PF) anode has smaller structure size in Z direction, which may affect the quantification of the anisotropic tortuosity factors of the anode, although the extent of the effect is not clear so far.

Hayashi [23] reported about the errors associated with the image processing of the FIB-SEM dataset. The edge part of the particles is inevitably blurred in the SEM observation; phase identification of such region causes segmentation error regardless of the method we employ. The influence of the segmentation error on the quantification was found to be at most 2.5% on the volume fraction and 3.6% on the TPB density.

Errors in the quantification methods themselves have been already mentioned previously. For an accurate quantification of the tortuosity factor and the TPB density, the characteristic scale of the porous structure, such as particle/pore size, needs to be resoluted with 20 and 10 voxels, respectively. For the quantification of the TPB density, all samples satisfy the requirement in all directions. On the other hand, for that of the tortuosity factor, the YSZ phase in the Ni:YSZ = 50:50 (PF) anode has a resolution of only 12 pixels in Z direction. The possible error in the anisotropic tortuosity factor in the direction is estimated at most 10 % based on the analysis with the well-defined structure shown in Fig. 2.11(b). The other phases satisfied the requirement.

2.5 Conclusions

In the present chapter, direct observation and following image processing and quantification techniques are developed and employed to the Ni-YSZ anodes of SOFCs. The three-dimensional microstructure of the porous anodes are directly observed with the dual-beam FIB-SEM technique. Then the quantification techniques are developed to characterize the porous microstructure. The anodes with four different compositions are examined and the fundamental understandings of the complex nature of the porous anode are obtained. Main conclusions drawn in the present chapter can be stated as follows:

1. Three-dimensional microstructure of the porous anode can be obtained at nano-scale resolution using the FIB-SEM system. The structure size available for the quantitative analysis is more than 10 μm^3. Use of low acceleration voltage of the electron beam (1–2 kV) and in-lens secondary electron detector provides the clear contrast between the three phases. Infiltration with epoxy resin is effective to eliminate the background effect from the cross-sectional images.

2. Microstructural parameters that have a significant influence on the anode performance can be quantified with the proposed methods. The volume fraction, percolation probability, tortuosity factor, and particle/pore size are obtained with in-house C-language-based program. For the TPB density and surface information, the commercial image processing software Avizo is used. Error analysis is conducted for the quantification of the tortuosity factor and the TPB density and shows the number of voxels required to resolute the characteristic structure of the porous anode: 20 for the tortuosity factor and 10 for the TPB density.

3. Analysis on the anodes with four different compositions provides fundamental insight on the composite anode microstructure. For example, low volume fraction with large particle size of a phase results in sparse distribution of the phase, making the connectivity worse. On the other hand, low volume fraction with small particle size of a phase results in a complex porous configuration even though the phase is spatially well-connected. Tortuosity factor, which is important to consider various transport phenomena in porous materials, is affected by other microstructural parameters such

as percolation probability and surface-to-volume ratio. For the optimization of the microstructure, further investigation of the relationships among the various microstructural parameters is required.

Bibliography

[1] D. Simwonis, F. Tietz, D. Stöver, Nickel Coarsening in Annealed Ni/8YSZ Anode Substrates for Solid Oxide Fuel Cells, *Solid State Ionics* **132** (2000) 241–251.

[2] J.H. Lee, H. Moon, H.W. Lee, J. Kim, J.D. Kim, K.H. Yoon, Quantitative Analysis of Microstructure and its Related Electrical Property of SOFC Anode, Ni-YSZ Cermet, *Solid State Ionics* **148** (2002) 15–26.

[3] D.S. McLachlan, An Equation for the Conductivity of Binary Mixtures with Anisotropic Grain Structures, *Solid State Physics* **20** (1987) 865–877.

[4] J. Gurland, The Measurement of Grain Contiguity in Two-Phase Alloys, *Transactions of the Metallurgical Society of AIME* **212** (1958) 452–455.

[5] Z. Fan, A.P. Miodownik, P. Tsakiropoulos, Microstructural Characterization of Two Phase Materials, *Material Science and Technology* **9** (1993) 1094–1100.

[6] K.R. Lee, S.H. Choi, J. Kim, H.W. Lee, J.H. Lee, Viable Image Analyzing Method to Characterize the Microstructure and the Properties of the Ni/YSZ Cermet Anode of SOFC, *Journal of Power Sources* **140** (2005) 226–234.

[7] S. Sunde, Calculation of Conductivity and Polarization Resistance of Composite SOFC Electrodes from Random Resistor Networks, *Journal of The Electrochemical Society* **142**(4) (1995) L50–L52.

[8] A. Abbaspour, J.L. Luo, K. Nandakumar, Three-Dimensional Random Resistor-Network Model for Solid Oxide Fuel Cell Composite Electrodes, *Electrochimica Acta* **55** (2010) 3944–3950.

[9] P. Costamagna, P. Costa, V. Antonucci, Micro-Modelling of Solid Oxide Fuel Cell Electrodes, *Electrochimica Acta* **43** (1998) 375–394.

[10] J.H. Nam, D.H. Jeon, A Comprehensive Micro-Scale Model for Transport and Reaction in Intermediate Temperature Solid Oxide Fuel Cells, *Electrochimica Acta* **51** (2006) 3446–3460.

[11] A. Abbaspour, K. Nadnakumar, J. Luo, K.T. Chuang, A Novel Approach to Study the Structure Versus Performance Relationship of SOFC Electrodes, *Journal of Power Sources* **161** (2006) 965–970.

[12] Y. Suzue, N. Shikazono, N. Kasagi, Micro Modeling of Solid Oxide Fuel Cell Anode Based on Stochastic Reconstruction, *Journal of Power Sources* **184** (2008) 52–59.

[13] J.R. Wilson, W. Kobsiriphat, R. Mendoza, H.Y. Chen, J.M. Hiller, D.J. Miller, K. Thornton, P.W. Voorhees, S.B. Adler, S.A. Barnett, Three-Dimensional Reconstruction of a Solid-Oxide Fuel-Cell Anode, *Nature Materials* **5** (2006) 541–544.

[14] P.R. Shearing, J. Golbert, R.J. Chater, N.P. Brandon, 3D Reconstruction of SOFC Anodes Using a Focused Ion Beam Lift-Out Technique, *Chemical Engineering Science* **64** (2009) 3928–3933.

[15] H. Iwai, N. Shikazono, T. Matsui, H. Teshima, M. Kishimoto, R. Kishida, D. Hayashi, K Matsuzaki, D. Kanno, M. Saito, H. Muroyama, K. Eguchi, N. Kasagi, H. Yoshida, Quantification of SOFC Anode Microstructure Based on Dual Beam FIB-SEM Technique, *Journal of Power Sources* **195** (2010) 955–961.

[16] D. Gostovic, J.R. Smith, D.P. Kundinger, K.S. Jones, E.D. Wachsman, Three-Dimensional Reconstruction of Porous LSCF Cathodes, *Electrochemical and Solid-State Letters* **10**(12) (2007) B214–B217.

[17] N. Vivet, S. Chupin, E. Estrade, T. Piquero, P.L. Pommier, D. Rochais, E. Bruneton, 3D Microstructural Characterization of a Solid Oxide Fuel Cell Anode Reconstructed by Focused Ion Beam Tomography, *Journal of Power Sources* **196** (2011) 7541–7549.

[18] Y. Nakashima, S. Kamiya, Mathematica Programs for the Analysis of Three-Dimensional Pore Connectivity and Anisotropic Tortuosity of Porous Rocks using X-ray Computed Tomography Image Data, *Journal of Nuclear Science and Technology* **44**(9) (2007) 1233–1247.

[19] *SIMD-oriented Fast Mersenne Twister (SFMT): twice faster than Mersenne Twister*, http://www.math.sci.hiroshima-u.ac.jp/ m-mat/MT/SFMT/index.html

[20] L. Holzer, B. Iwanschitz, Th. Hocker, B. Munch, M. Prestat, D. Wiedenmann, U. Vogt, P. Holtappels, J. Sfeir, A. Mai, Th. Graule, Microstructure Degradation of Cermet Anodes for Solid Oxide Fuel Cells: Quantification of Nickel Grain Growth in Dry and in Humid Atmospheres, *Journal of Power Sources* **196** (2011) 1279–1294.

[21] B. Iwanschitz, L. Holzer, A. Mai, M. Schutze, Nickel Agglomeration in Solid Oxide Fuel Cells: The Influence of Temperature, *Solid State Ionics* **211** (2011) 69–73.

[22] D. Kanno, N. Shikazono, N. Takagi, K. Matsuzaki, N. Kasagi, Evaluation of SOFC Anode Polarization Simulation Using Three-Dimensional Microstructures Reconstructed by FIB Tomography, *Electrochimica Acta* **56** (2011) 4015–4021.

[23] D. Hayashi, Bachelor thesis, Observation of SOFC Anode Microstructure Using a Series of Cross-Sectional SEM Images, *Kyoto University*, Japan 2009.

Chapter 3

One-Dimensional Numerical Simulation of Anode Overpotential Characteristics with Microstructural Parameters of Porous Structure

3.1 Introduction

Numerical simulation is one of the most powerful and effective tools to investigate the relationships between the electrode microstructure and the performance. Detailed information inside the complex porous structure, such as the distribution of the gas concentration and the charge-transfer current can be obtained, some of which are not accessible in experiments. From the parametric study on various operating conditions and microstructural parameters, rate-limiting process in the SOFC electrodes can be identified, which is significantly valuable in optimizing the cell configuration and the electrode microstructure.

Nam et al [1]. conducted a one-dimensional numerical simulation of an intermediate-temperature SOFC cell with the detailed description of the microscale transport and the electrochemical reaction. They found that the effect of the particle size is the most significant on the electrode performance because smaller particle size reduces the activation overpotential by increasing the TPB density in the electrodes. However, small particle size also results in increasing mass transport resistance in the pore phase; optimal size for the solid particles need to be determined considering both the TPB density and the gas diffusivity. Zhu et al [2]. also developed a model that considered parallel transport in porous

electrodes with the electrochemical reaction. Significant improvement in their model was in the electrochemical reaction model that considers heterogeneous chemistry on the solid surface, such as adsorption and desorption. They suggested that the function-layer thickness and particle sizes are among the most effective parameters for optimizing the electrode microstructure. Chen et al [3]. applied similar modeling approach for the optimization of the cathode interlayer. They varied the interlayer thickness as well as various microstructural parameters, and found the optimal thickness of the interlayer.

In spite of the effectiveness of the simulation techniques, they have obvious drawbacks. Since there had been few reliable structure data of the porous electrodes, they were bound to rely on porous models. As a result, the numerical model contains uncertainty both in the applicability of the porous models and the validity of the transport and electrochemical models. This issue makes it difficult to validate the whole numerical model; and hence, poses questions on their findings.

Thus, the recent advances in the three-dimensional observation technique such as the FIB-SEM are highly expected to exclude the uncertainty of the structure model from the whole numerical model. The microstructural parameters quantified from the real porous microstructure can be applied to the numerical model. Although there are some issues unsolved in the quantification of microstructural parameters, such as the limited volume size observable in the tomography and the accuracy of the quantification methods, use of the real microstructure has a significant advantage. Development of reliable simulation techniques using the real electrode microstructure is eagerly desired.

In the present chapter, one-dimensional numerical simulation of the SOFC anode will be conducted considering various transport phenomena in the porous electrode, which are linked by the electrochemical reaction at the TPB. The microstructural parameters of the porous anode will be applied to the model to evaluate the effective transport coefficient and the electrochemical activity of the anode. Numerical results will be compared with the experimental counterparts under various operating conditions to evaluate the validity and applicability of the proposed model. For the fundamental understanding of the effect of the microstructure on the overall anode performance, sensitivity analysis will be conducted varying microstructural parameters, and the rate-limiting process in the anode will be identified.

3.2 Numerical Model

The simulation is based on the finite volume method (FVM) with a uniform grid system, and is conducted in the thickness direction of the anode. The conservation of electron, oxide ion, and gas components are considered, which are linked by the sink and source terms associated with the electrochemical oxidation of hydrogen at the TPB. The microstructural parameters that are necessary to evaluate the effective transport coefficients and electrochemical reaction rate in the anode are evaluated from the Ni:YSZ = 50:50 (PF) anode. Temperature is assumed to be constant and uniform in the anode.

3.2.1 Calculation domain

Schematic picture of the calculation domain is shown in Fig. 3.1. The size of the grid is 0.5 μm and uniform over the entire anode region. Gas transport through the porous structure is assumed to be driven only by diffusion; convection effect is neglected. The microstructural parameters such as the tortuosity factors, pore size, and the TPB density are applied to all grids to evaluate the effective transport coefficients and the electrochemical reaction rate.

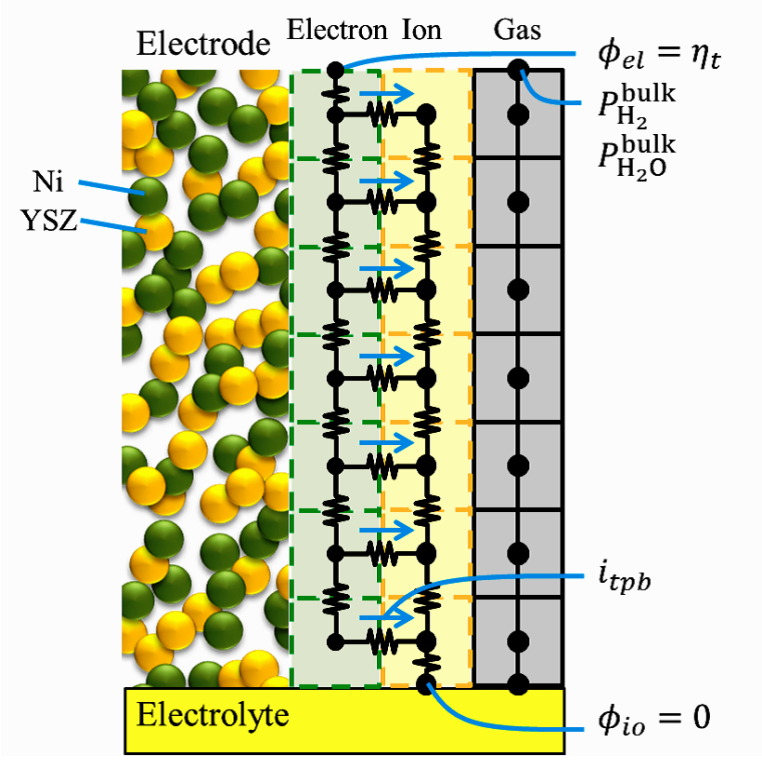

Fig. 3.1. Schematic picture of the calculation domain.

3.2.2 Governing equations

3.2.2.1 Transport of electrons and ions

In the SOFC anodes, electrons and oxide ions are transported through the Ni phase and the YSZ phase, respectively. Considering the conservation of these charge carriers, the following equations are introduced in terms of the electric potential of the phases:

$$\nabla \cdot (\sigma_{el}^{\text{eff}} \nabla \phi_{el}) = -i_{tpb} \tag{3.1}$$

$$\nabla \cdot (\sigma_{io}^{\text{eff}} \nabla \phi_{io}) = i_{tpb} \tag{3.2}$$

where ϕ_{el} and ϕ_{io} are the electric potential in the electron conductive phase (Ni) and the oxide-ion conductive phase (YSZ), respectively, and i_{tpb} is the density of the current exchanged between the two phases (charge-transfer current). σ_{el}^{eff} and σ_{io}^{eff} are the effective electron/ion conductivities, which are defined using the microstructural parameters:

$$\sigma_{el}^{\text{eff}} = \frac{V_{\text{Ni}}}{\tau_{\text{Ni}}} \sigma_{el}, \qquad \sigma_{io}^{\text{eff}} = \frac{V_{\text{YSZ}}}{\tau_{\text{YSZ}}} \sigma_{io} \tag{3.3}$$

where V_l and τ_l are the volume fraction and the tortuosity factor of the phase l. And σ_{el} and σ_{io} are the conductivities of the bulk materials obtained from literatures [4, 5].

$$\sigma_{el} = 3.27 \times 10^4 - 10.653T \tag{3.4}$$

$$\sigma_{io} = 3.40 \times 10^2 \exp\left(-\frac{10350}{T}\right) \tag{3.5}$$

3.2.2.2 Diffusion of gas species

The dusty-gas model (DGM) [6, 7] is used to simulate multi-component gas diffusion in the porous electrodes. This model includes the flow induced by a total pressure gradient and can also be used in the situation where the effect of Knudsen diffusion is not negligible. The DGM is written as an implicit relationship among the molar fraction, molar flux, and total pressure gradient:

$$\nabla \cdot \boldsymbol{N}_l = s_l \tag{3.6}$$

$$\frac{\boldsymbol{N}_l}{D_{l,K}^{\text{eff}}} + \sum_{m=1, m\neq l}^{n} \frac{X_m \boldsymbol{N}_l - X_l \boldsymbol{N}_m}{D_{lm}^{\text{eff}}} = -\frac{P_t}{RT} \nabla X_l - \frac{X_l}{RT} \left(1 + \frac{K P_t}{\mu D_{l,K}^{\text{eff}}}\right) \nabla P_t \tag{3.7}$$

where X_l, P_l and N_l are the molar fraction, partial pressure and molar flux of gas species l. P_t is the total pressure. s_l is the source term associated with the electrochemical reaction at

the TPB described as follows:

$$s_{\mathrm{H_2}} = -\frac{i_{tpb}}{2F}, \quad s_{\mathrm{H_2O}} = \frac{i_{tpb}}{2F} \tag{3.8}$$

μ and K are the mixture viscosity and permeability, and $D^{\mathrm{eff}}_{l,\mathrm{K}}$ and D^{eff}_{lm} are the effective Knudsen diffusion coefficients and the effective binary diffusion coefficients, respectively.

In the binary system ($n = 2$), eq. (3.6) and (3.7) can be divided into two partial differential equations as follows:

$$\nabla \cdot \left(\frac{k_1}{RT} \nabla P_1 \right) + \nabla \cdot \left(\frac{k_2 P_1}{RT} \nabla P_t \right) = \frac{i_{tpb}}{2F} \tag{3.9}$$

$$\nabla \cdot \left(\frac{k_3}{RT} \nabla P_2 \right) + \nabla \cdot \left(\frac{k_4 P_2}{RT} \nabla P_t \right) = -\frac{i_{tpb}}{2F} \tag{3.10}$$

$$k_1 = \frac{D^{\mathrm{eff}}_{12} D^{\mathrm{eff}}_{1,K}}{D^{\mathrm{eff}}_{12} + D^{\mathrm{eff}}_{12,K}}, \quad k_3 = \frac{D^{\mathrm{eff}}_{12} D^{\mathrm{eff}}_{2,K}}{D^{\mathrm{eff}}_{12} + D^{\mathrm{eff}}_{12,K}} \tag{3.11}$$

$$k_2 = k_4 = \frac{K}{\mu} + \frac{D^{\mathrm{eff}}_{1,K} D^{\mathrm{eff}}_{2,K}}{D^{\mathrm{eff}}_{12} + D^{\mathrm{eff}}_{12,K}} \frac{1}{P_t} \tag{3.12}$$

$$D^{\mathrm{eff}}_{12,K} = X_1 D^{\mathrm{eff}}_{2,K} + X_2 D^{\mathrm{eff}}_{1,K} \tag{3.13}$$

where the subscripts 1 and 2 denote the H_2 and H_2O, respectively.

The effective Knudsen diffusion coefficients $D^{\mathrm{eff}}_{l,\mathrm{K}}$ and the effective binary diffusion coefficients D^{eff}_{lm} in the porous anode are estimated by using the volume fraction and the tortuosity factor of the pore phase:

$$D^{\mathrm{eff}}_{l,\mathrm{K}} = \frac{V_{\mathrm{Pore}}}{\tau_{\mathrm{Pore}}} D_{l,\mathrm{K}}, \qquad D^{\mathrm{eff}}_{lm} = \frac{V_{\mathrm{Pore}}}{\tau_{\mathrm{Pore}}} D_{lm} \tag{3.14}$$

The bulk Knudsen diffusion coefficients are estimated as

$$D_{l,\mathrm{K}} = \frac{d_p}{2} \frac{2}{3} \sqrt{\frac{8RT}{\pi M_l}} \tag{3.15}$$

where M_l is the molecular mass, and d_p is the mean pore diameter, which is assumed to be the same as the hydraulic diameter d_h, and is described using the surface-to-volume ratio of the pore phase:

$$d_p \simeq d_h = \frac{4}{(S/V)_{\mathrm{Pore}}} \tag{3.16}$$

For the binary diffusion coefficients, the Fuller-Schettler-Giddings' equation [8] is adopted in this study:

$$D_{lm} = \frac{0.01013 T^{1.75} \left\{ (1/M_l \times 10^3) + (1/M_m \times 10^3) \right\}^{1/2}}{P[(\Sigma v_l \times 10^6)^{1/3} + (\Sigma v_m \times 10^6)^{1/3}]^2} \tag{3.17}$$

where Σv_l represents the diffusion volume of the molecules of species l [9].

Permeability of the porous anode is also necessary to consider the Darcy flow. Among many ways to estimate the parameter [10], the following relationship is adopted to directly use the microstructural parameters evaluated in this study:

$$K = \frac{V_{\mathrm{Pore}}}{6\tau_{\mathrm{Pore}}(S/V)^2_{\mathrm{Pore}}} \tag{3.18}$$

In this formula, the porous network is considered as a group of curved channels, whose diameters are uniform and given by eq. (3.16), and the flow inside is assumed to be a Poiseuille flow. By comparing the Darcy's law with the Poiseuille's law, the above formula is obtained.

3.2.3 Electrochemical reaction model

In SOFC anodes, electrochemical oxidation of hydrogen takes place at the TPB. Currently the evaluation of the charge-transfer rate in SOFC electrodes is still an open issue. As Gorte et al [11]. pointed out, simple Butler-Volmer equation is not always valid in SOFC electrodes because the formula is originally derived to describe reactions that take place at the surface of a metal electrode in electrolytic solution. Therefore, many researches were devoted to investigate the charge-transfer rate in SOFC anodes [13–15]. Kawada et al. [16] experimentally investigated the charge-transfer rate with a Ni-YSZ cermet anode in both anodic and cathodic regimes and developed a modified Butler-Volmer-like equation:

$$i_{tpb} = i_0 \left[\exp\left(\frac{2F}{RT}\eta_{act}\right) - \exp\left(-\frac{F}{RT}\eta_{act}\right) \right] \tag{3.19}$$

where i_0 is the exchange current density, and η_{act} is the activation overpotential. Although the physical meaning of the symmetric factor in eq. (3.19) was not clarified, it is likely to be attributed to the elementary electrochemical reaction around the TPB, such as H_2 adsorption and dissociation on the Ni surface.

In this study, eq. (3.19) for the charge-transfer model is adopted because the model was also used in the three-dimensional numerical analysis by Shikazono et al [17]., in which the same anode structure data obtained with the FIB-SEM was used. Therefore, the comparison between the simulation results becomes possible.

Activation overpotential is derived as follows:

$$\begin{aligned}\eta_{act} &= E - E^{eq} \\ &= \Phi_{el} - \Phi_{io} - E_0^{eq} - \frac{RT}{2F}\ln\left(\frac{P_{\mathrm{H_2O}}^{\mathrm{bulk}}}{P_{\mathrm{H_2}}^{\mathrm{bulk}}}\right) - \frac{RT}{2F}\ln\left(\frac{P_{\mathrm{H_2}}^{\mathrm{bulk}}}{P_{\mathrm{H_2}}}\frac{P_{\mathrm{H_2O}}}{P_{\mathrm{H_2O}}^{\mathrm{bulk}}}\right)\end{aligned} \tag{3.20}$$

where $E = \Phi_{el} - \Phi_{io}$ is the electric potential difference between the electronic and ionic phases in the operating condition. E^{eq} is the electric potential difference between the two phases at the equilibrium, and E_0^{eq} is that in the standard state. $P_{\mathrm{H_2}}^{\mathrm{bulk}}$ and $P_{\mathrm{H_2O}}^{\mathrm{bulk}}$ are the partial pressures of the gas species on the anode surface. In this study, following variables are introduced to rewrite eq. (3.20) [18]:

$$\phi_{el} = \Phi_{el} \tag{3.21}$$

$$\phi_{io} = \Phi_{io} + E_0^{eq} + \frac{RT}{2F}\ln\left(\frac{P_{\mathrm{H_2O}}^{\mathrm{bulk}}}{P_{\mathrm{H_2}}^{\mathrm{bulk}}}\right) \tag{3.22}$$

$$\eta_{act} = \phi_{el} - \phi_{io} - \eta_{con} \tag{3.23}$$

$$\eta_{con} = \frac{RT}{2F}\ln\left(\frac{P_{\mathrm{H_2}}^{\mathrm{bulk}}}{P_{\mathrm{H_2}}}\frac{P_{\mathrm{H_2O}}}{P_{\mathrm{H_2O}}^{\mathrm{bulk}}}\right) \tag{3.24}$$

By using these variables, the electric potential difference between the two solid phases are regarded as the sum of the activation overpotential η_{act} and the concentration overpotential η_{con}.

The exchange current density i_0 in the Buttler-Volmer-like equation (eq. (3.19)) strongly depends on the microstructure of the anode, and is considered to have a linear dependency on the TPB density l_{tpb}:

$$i_0 = i_{0,tpb} l_{tpb} \tag{3.25}$$

where $i_{0,tpb}$ is the exchange current per unit TPB length. In this study, the following empirical relationship is used for the value [13, 19]:

$$i_{0,tpb} = 31.4 P_{\mathrm{H_2}}^{-0.03} P_{\mathrm{H_2O}}^{0.4} \exp\left(-\frac{1.52\times10^5}{RT}\right) \tag{3.26}$$

3.2.4 Boundary conditions

Boundary conditions used in the calculation are summarized in Table 3.1. Gas compositions are constant on the anode surface to represent the supplied fuel composition. In order to determine the anode overpotential, the electric potential in the Ni phase at the

anode surface and that in the YSZ phase at the anode-electrolyte interface are properly set. Also, no flux conditions are set on the anode surface for the ionic potential and on the anode-electrolyte interface for gas components and electric potential.

3.2.5 Calculation conditions

Various microstructural parameters are necessary to determine the effective transport coefficients in (3.1), (3.2), and (3.7) and to determine the electrochemical reaction rate (3.19). In this chapter, the microstructural parameters evaluated from the Ni:YSZ = 50:50 (PF) anode are used. Applied values of the microstructural parameters and other computational conditions are shown in Table 3.2. These values are basically kept constant in the following calculations unless specified.

Table 3.1. Boundary conditions.

Parameter	Surface ($X = 0$)	Interface ($X = L$)
Total pressure	$P_t(0) = P_t^{\mathrm{bulk}}$	$\frac{dP_t}{dx}(L) = 0$
H_2 partial pressure	$P_{\mathrm{H_2}}(0) = P_{\mathrm{H_2}}^{\mathrm{bulk}}$	$\frac{dP_{\mathrm{H_2}}}{dx}(L) = 0$
H_2O partial pressure	$P_{\mathrm{H_2O}}(0) = P_{\mathrm{H_2O}}^{\mathrm{bulk}}$	$\frac{dP_{\mathrm{H_2O}}}{dx}(L) = 0$
Electric potential in Ni	$\phi_{el}(0) = \eta_t$	$\frac{d\phi_{el}}{dx}(L) = 0$
Electric potential in YSZ	$\frac{d\phi_{io}}{dx} = 0$	$\phi_{io}(L) = 0$

Table 3.2. Default calculation conditions.

Parameter	Symbol	Value	Unit
Total Pressure	P_t^{bulk}	1.013×10^5	[Pa]
Temperature	T	1000	[°C]
H_2 partial pressure	$P_{\mathrm{H_2}}^{\mathrm{bulk}}$	$0.97 \times P_t^{\mathrm{bulk}}$	[Pa]
H_2O partial pressure	$P_{\mathrm{H_2O}}^{\mathrm{bulk}}$	$0.03 \times P_t^{\mathrm{bulk}}$	[Pa]
Ni volume fraction	V_{Ni}	0.253	
YSZ volume fraction	V_{YSZ}	0.251	
Pore volume fraction	V_{Pore}	0.496	
Ni tortuosity factor	τ_{Ni}	6.91	
YSZ tortuosity factor	τ_{YSZ}	8.85	
Pore tortuosity factor	τ_{Pore}	1.74	
Pore S-V ratio	$(S/V)_{\mathrm{Pore}}$	4.12×10^6	[m^2/m^3]
TPB density	l_{tpb}	2.49×10^{12}	[m/m^3]
Anode thickness	L	5.0×10^{-5}	[m]

3.3 Results and Discussion

3.3.1 Comparison between numerical results and experiment

In electrochemical cells, three voltage losses play an important role to determine the cell performance, namely, ohmic loss, activation overpotential, and concentration overpotential. Since the electric conductivity of the Ni phase is sufficiently large, the ohmic loss in the anode layer is assumed to be negligible. On this assumption, the anode overpotential measured in the experiment and that set in the numerical simulation as the boundary condition are both interpreted as the sum of the activation overpotential and the concentration overpotential. In this chapter, this overpotential is defined as the "anode overpotential" and used for the comparison between the numerical simulation and the experiment.

Fig. 3.2 shows the typical distributions of the electric potentials and the charge-transfer current density inside the anode in the thickness direction. The left end of the figure corresponds to the anode surface while the right end (50 μm) to the anode-electrolyte interface. The calculation is conducted keeping the total anode overpotential to be 0.05 V, and the average current density is calculated as 411.0 mA/cm^2. The charge-transfer current density i_{tpb} shows the rate of the electrochemical reaction. It can be observed that the value of i_{tpb} is largest at the anode-electrolyte interface and sharply decreases toward the anode surface direction. It shows that most of the electrochemical reaction occurs in the vicinity of the anode-electrolyte interface within about 10 μm. The thickness of the active reaction region in cermet anodes is still an open issue but 10 μm seems to be reasonable for an anode having the microstructure in this study. Brown et al [20]. experimentally analyzed the active reaction thickness in a Ni-YSZ anode with particle diameter 0.5–1 μm, which is similar to that in this study, and reported the active reaction thickness is about 10 μm. Shikazono et al [17]. conducted three-dimensional numerical simulation using the same anode structure as that is used in this study, and reported the similar reaction thickness around 10–15 μm. Since the hydrogen supply is sufficient for the electrochemical reaction in this case, the effect of concentration overpotential is limited. Note that the concentration overpotential is graphically expressed as the gap between the black line and the blue line. The activation overpotential, which is expressed as the gap between the blue and the red lines, becomes large near the anode-electrolyte interface where the electrochemical reaction is prominent.

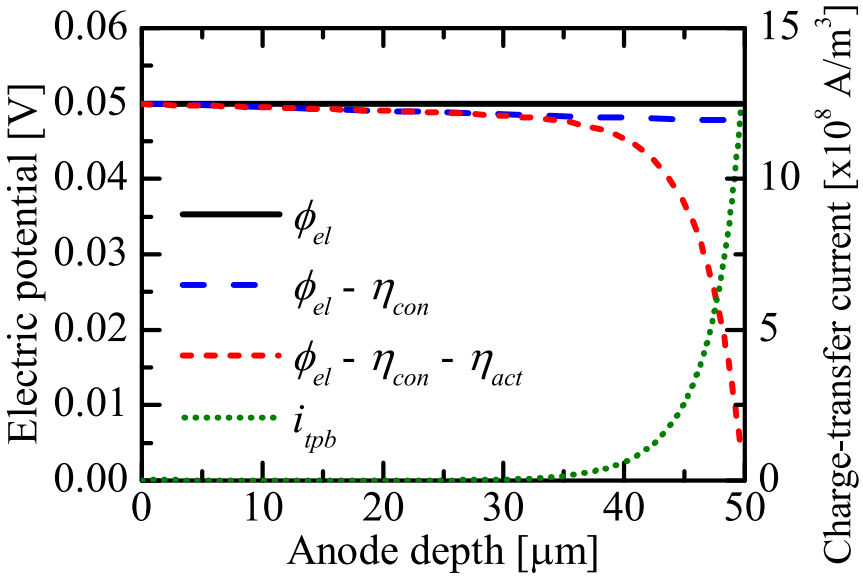

Fig. 3.2. Charge-transfer current density and potential distributions in the default case. Total anode overpotential is set to be 0.05 V. Average current density is 411.0 mA/cm^2.

The figure shows that the activation overpotential is the major cause of the voltage loss and it occurs in the vicinity of the anode-electrolyte interface.

Calculations are conducted under various anode overpotential and fuel gas compositions. Fig. 3.3 compares the anode overpotentials predicted by the simulation with their experimental counterparts at 1000 °C under two different humidified conditions. The predicted overpotentials agree fairly well with the experimental counterparts at 3% humidified condition. When the steam concentration is raised to 20%, the anode overpotential decreases in the experiment and the simulation qualitatively captures this phenomenon. However the anode overpotential is about twice overestimated in the condition. This may be because of the empirical relationship used for the exchange current density per unit TPB length $i_{0,tpb}$ (eq. (3.26)). In the relationship, it is possible that the catalytic activity of steam is underestimated. Another possible reason of the discrepancy is the effect of the local high steam concentration around the TPB. In the polarized condition, electrochemical reaction produces steam, which causes high steam concentration locally around the TPB. Such a local inhomogeneity in the gas compositions can decrease the activation overpotential. A similar discrepancy between the simulation and the experiment under the high steam condition is also reported by Shikazono et al [17]. Further investigation is required to understand the

phenomenon under the high steam concentration.

Figure 3.4 shows the effect of the operating temperature on the anode overpotential. Except for the temperature, calculation parameters shown in Table 3.2 are used. The predicted overpotential agrees fairly well with the experimental counterpart at 1000 °C. The anode overpotential increases as the operating temperature is decreased in the experiment. The one-dimensional simulation can reproduce this tendency but in the low temperature conditions, 900 and 800 °C, it is overestimated particularly in the large current density region. The local high steam concentration mentioned above may also be the reason of the overestimation. Another possible reason is the effect of the activation energy used in the exchange current density model (eq. (3.26)). Bieberle et al [14]. reported smaller activation energy in the H_2 oxidation on the Ni pattern electrode. Use of smaller activation energy may result in reproducing the temperature dependency closer to the experimental results; however, the absolute value of the exchange current density estimated from their experiment is two orders higher than that reported by de Boer [13]. Therefore, it is still difficult to obtain reasonable values of overpotentials in low temperature conditions.

It is wroth stressing that the simulation model proposed in this chapter includes no adjustable parameter to fit the result into the experimental result. Nevertheless the predicted overpotentials are of the same order of magnitude as those from the experiment. Even though further improvement is possible in the model, the outcome of this chapter expresses the possibility of predicting the electrode performance based on the real microstructure of the porous electrodes and finding the relationships between the electrode performance and the microstructure.

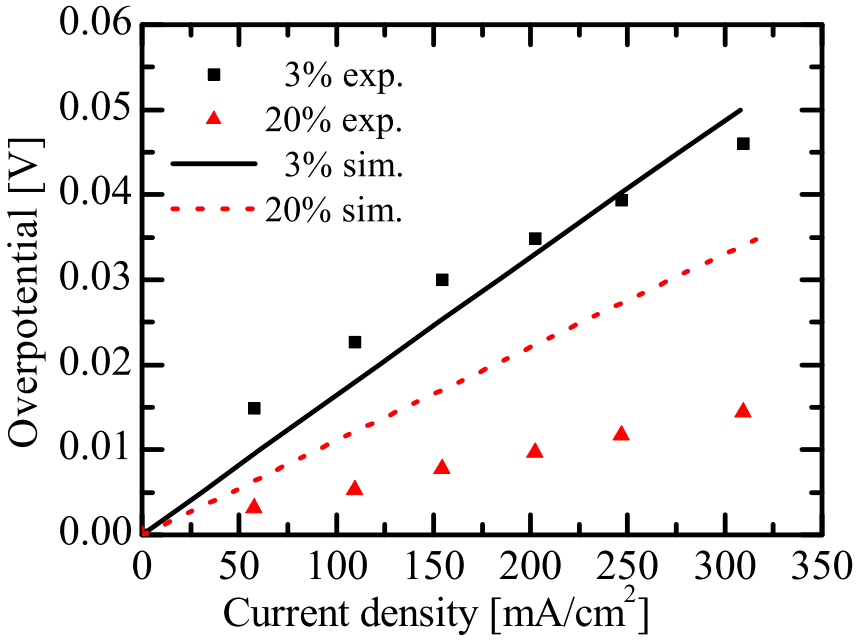

Fig. 3.3. Anode overpotentials in various steam concentration at 1000 °C.

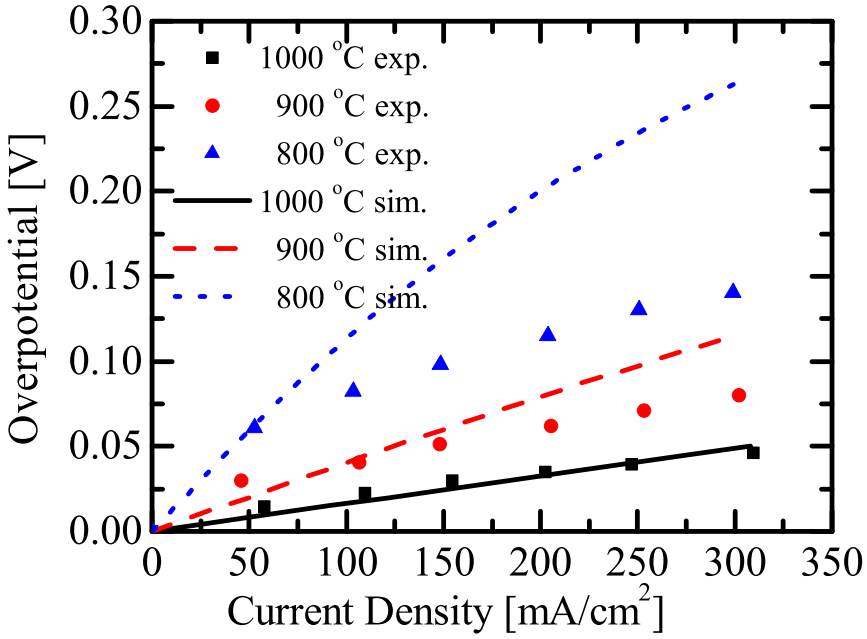

Fig. 3.4. Anode overpotentials in various temperatures at 3% humidified condition.

3.3.2 Effect of the microstructural parameters on the anode overpotential characteristics

According to the microstructural analysis of the Ni:YSZ = 50:50 (PF) anode, the tortuosity factors of the Ni and YSZ phases are quite large, which inhibits the electron and ion transport through these phases. To optimize the microstructure, the anode should be fabricated so that the tortuosity factors are as small as possible. However, the tortuosity factor depends on other microstructural parameters implicitly, hence it is difficult to decrease the tortuosity factor of all phases at the same time. Assuming that there is no drastic change in the microstructure, it is possible to make the Ni tortuosity factor smaller by slightly increasing the volume fraction of the phase. However, this causes a decrease of the YSZ volume faction and increases the YSZ tortuosity factor. Therefore, it is important to investigate the dependency of the power generation performance on the various microstructural parameters and to determine which phase should be prioritized in the optimization approach. In this chapter, the current density is adopted as an indicator of the power generation performance. In this simulation, the anode overpotential is set as a boundary condition; therefore, the larger current density indicates the larger power output of the cell. Here, it is examined how the power generation performance is affected by changing the microstructural parameters such as the tortuosity factor, the surface-to-volume ratio, and the TPB density. Except for the microstructural parameters that were varied for the sensitivity analysis, the calculation is conducted with the parameters listed in Table 3.2. It is assumed that the variation of the considered microstructural parameters have no influence on the other parameters.

3.3.2.1 Effect of the tortuosity factor

Figure 3.5 shows the predicted current density over the tortuosity factor of each phase ranging from 1 to 20. The anode overpotential is set to be 0.1 V. Larger tortuosity factors indicate that the phases have much more complicated microstructure and the effective transport coefficients in the phases are smaller according to eqs. (3.3) and (3.14). Therefore, the current density is expected to decrease as the tortuosity factor becomes larger. Since the electron conductivity of the Ni phase is considerably higher than the oxide ion conductivity in the YSZ phase and the gas diffusivity in the pore phase, the effect of the Ni tortuosity factor on the current density is almost negligible. On the other hand, the current density

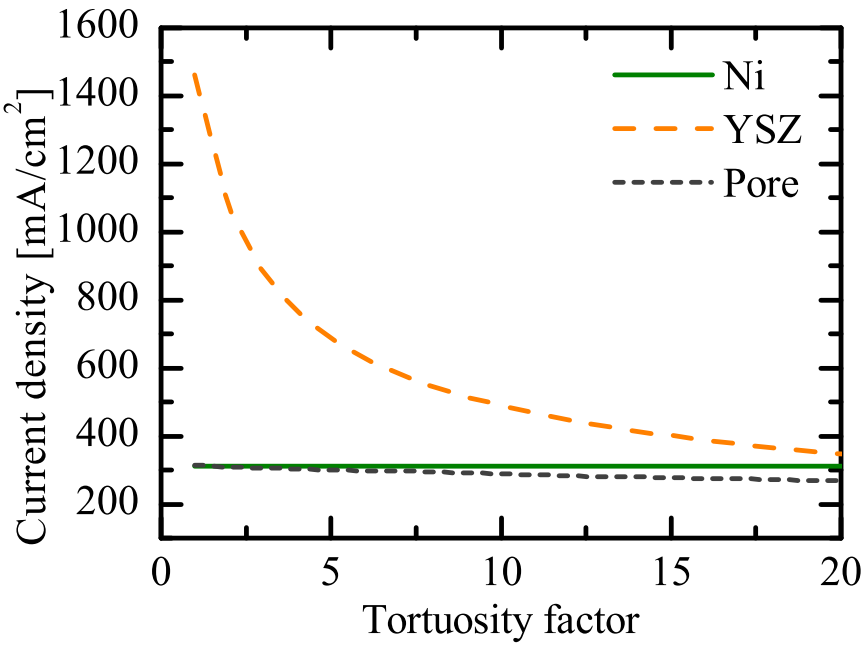

Fig. 3.5. Dependency of the current density on the tortuosity factor ranging from 1 to 20 at the anode overpotential of 0.1 V.

has a very high sensitivity to the YSZ tortuosity factor. This implies that the oxide-ion conduction through the YSZ phase is one of the rate-limiting processes in the SOFC anodes. Therefore, the first priority in optimizing the anode microstructure is to decrease the complexity of the YSZ phase; and hence promote the oxide-ion transport. In addition, the dependency of the anode performance on the YSZ tortuosity factor is non-linear; more performance improvement can be expected when the tortuosity factor is reduced to less than 5. The effect of the pore tortuosity factor is limited compared with that of the YSZ tortuosity factor because the diffusivity in the pore phase is relatively higher.

3.3.2.2 Effect of the surface-to-volume ratio

Next, the surface-to-volume ratio is varied from 10^{-3} to 10^{3} $\mu m^2/\mu m^3$ at the anode overpotential of 0.1 V. In the SOFC anodes, Knudsen diffusion plays an important role in mass transport because the characteristic scale of the pores is comparable to or even smaller than the mean free path of the gas molecules. Therefore, an order analysis about the various diffusion coefficients is conducted to determine which effect is dominant in the mass transport. According to eq. (3.17), the binary diffusion coefficient is constant if the temperature and total pressure are constant. On the other hand, according to eqs. (3.15) and (3.16), the Knudsen diffusion coefficients depend on the surface-to-volume ratio. In the DGM model, since k_1 and k_3 are interpreted as a kind of mixture diffusion coefficients in the fuel gas, the variation of these coefficients are investigated over the wide range of the surface-to-volume ratio. The results are shown in Fig. 3.6(a). The Knudsen diffusion coefficients of H_2 (denoted as subscript 1) and H_2O (denoted as subscript 2), and the binary molar diffusion coefficient are shown. In the region where the surface-to-volume ratio is relatively small, the mixture diffusivity k_1 and k_3 are almost constant and comparable to the binary diffusivity. This is because the molecular diffusion dominates the mass transport. On the other hand, they asymptotically converge to the Knudsen diffusion coefficients as the surface-to-volume ratio becomes larger. Therefore, in the situation where the surface-to-volume ratio is larger and thus, the characteristic scale of the pores is small, the Knudsen diffusion is expected to dominate the mass transfer. It should be noted that the surface-to-volume ratio evaluated from the sample anodes in this study are on the order of 1 $\mu m^2/\mu m^3$, which corresponds to the transient region between the molecular diffusion and the Knudsen diffusion.

The sensitivity of the current density to the surface-to-volume ratio of the pore phase is shown in Fig. 3.6(b). In the molecular-diffusion-dominant region, the current density is almost constant, while in the Knudsen-diffusion-dominant region the value gradually decreases because the Knudsen diffusion coefficient becomes smaller in the small characteristic scale. Generally, smaller particle size of the solid phases results in increasing the TPB density, which is preferable for the electrochemical reaction; however, it also makes the mass transport resistance higher. It is important to consider the balance between the two opposite effects in optimizing the electrode microstructure.

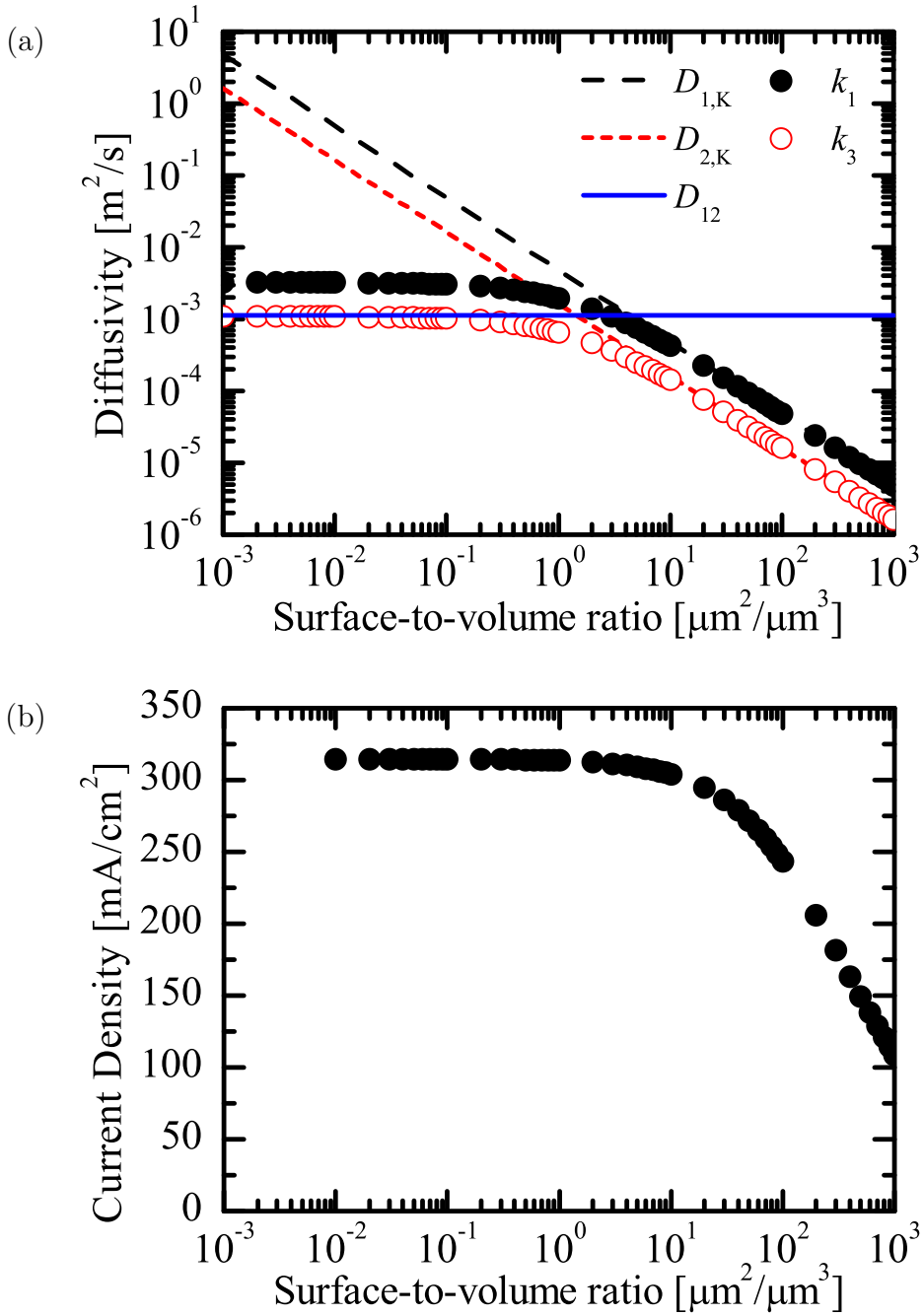

Fig. 3.6. Variation of the diffusion coefficients and the current density when the the surface-to-volume ratio varies from 10^{-3} to 10^{3} μm^2/μm^3 at the anode overpotential of 0.1 V.

3.3.2.3 Effect of the TPB density

Fig. 3.7 shows the predicted current density over the TPB density ranging from 0 to 10 $\mu m/\mu m^3$ at the anode overpotential of 0.1 V. The calculation result is reasonable because larger TPB density provides more reaction sites in the anode layer. The effect of the TPB density on the anode performance is relatively large when the TPB density is smaller than 1 $\mu m/\mu m^3$, after that the dependency is almost linear because the gas diffusivity in the anode is large enough to supply enough hydrogen to the active reaction region that is typically located in the vicinity of the anode-electrolyte interface. Fig. 3.8 shows the distribution of the charge-transfer current density in the thickness direction of the anode. Since the total amount of the current generated in the anode depends on the TPB density, the local charge-transfer current is normalized by the total current. As the TPB density increases, not only the total amount of the current generated in the anode increases, but also there is a slight change in the reaction region. The electrochemical reaction more preferably occurs in the vicinity of the anode-electrolyte interface in larger TPB density, which results in thinner active thickness. More comprehensive investigation of the active thickness will be presented in Chapter 6.

3.3.3 Error assessment

The sensitivity analysis conducted above is also useful for the error assessment; the influence of the microstructural characterization on the simulation accuracy can be quantitatively estimated. As discussed in Chapter 2, the quantified microstructural parameters have some extent of errors: at most 10% in the tortuosity factors, and 3.6% in the TPB density. According to Fig. 3.5, an error of plus or minus 10% around the $\tau_{\mathrm{YSZ}} = 8.85$ results in at most 5% error in the current density. According to Fig. 3.7, the 3.6% error around the $l_{tpb} = 2.49$ results in at most 2% error in the current density. These errors are small enough to validate the discussion in this chapter.

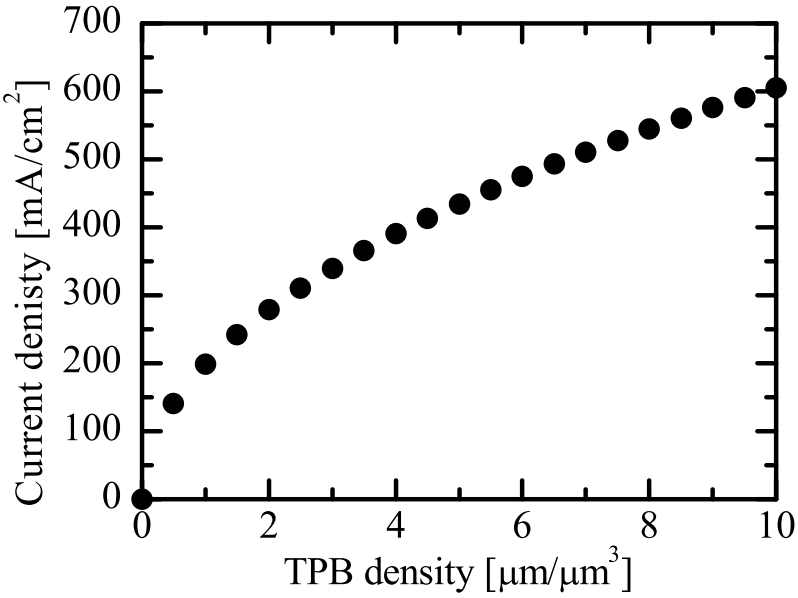

Fig. 3.7. Dependency of the current density on the TPB density ranging from 0 to 10 μm/μm^3 at the anode overpotential of 0.1 V.

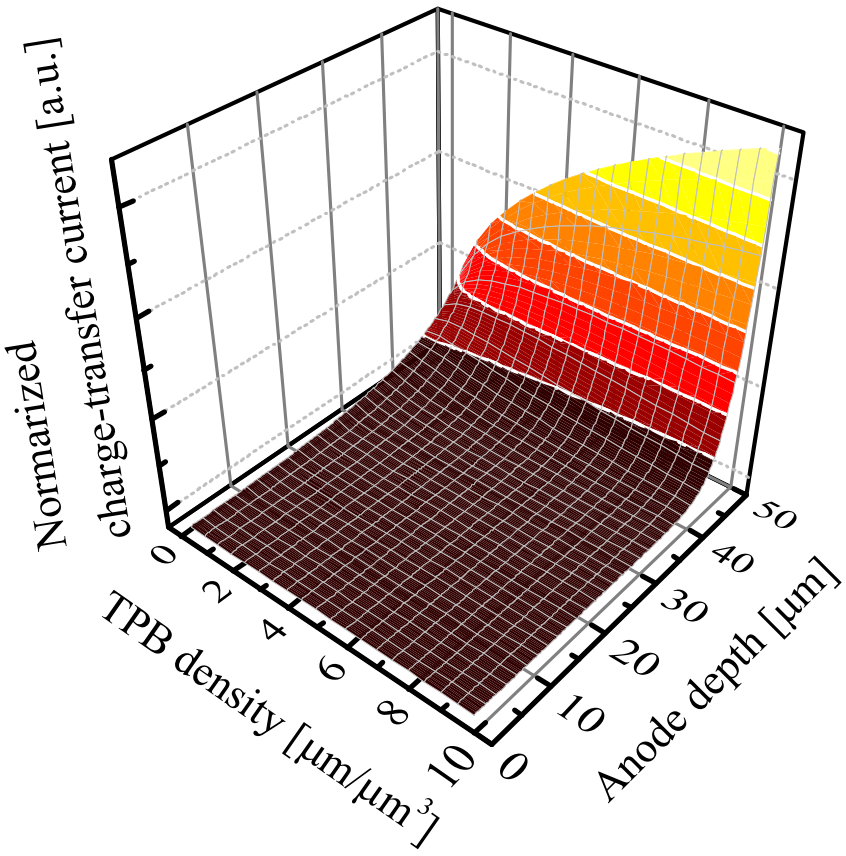

Fig. 3.8. Distribution of the normalized charge-transfer current when the TPB density is varied from 0 to 10 μm/μm^3 at the anode overpotential of 0.1 V.

3.4 Conclusions

In the present chapter, one-dimensional numerical simulation of the SOFC anode is conducted considering the various transport phenomena in the porous electrode, which are linked by the electrochemical reaction at the TPB. The microstructural parameters of the porous anode are applied to the model to evaluate the effective transport coefficients and the electrochemical reaction rate. Numerical results are compared with the experimental counterparts under various operating conditions to validate the proposed model. For the fundamental understanding of the effect of the microstructure on the overall anode performance, sensitivity analysis is conducted varying the microstructural parameters, and the rate-limiting process in the anode is identified. Main conclusions drawn in the present chapter can be stated as follows:

1. A one-dimensional numerical simulation of the anode overpotential is successfully conducted without using any structure model but with the microstructural parameters quantified from the reconstructed three-dimensional structure. The predicted overpotential agrees well with the experimental counterparts in the condition of the low steam concentration (3%) and high temperature (1000 °C). The effects of steam concentration and temperature can be qualitatively reproduced; however, the values are overestimated in high steam concentration (20%) and low temperature (900, 800 °C) conditions. Although further improvement is possible in the model, the outcome of this chapter linking the electrode microstructure and the performance should be stressed.

2. Among the various transport phenomena in the porous anode, the oxide-ion transport through the YSZ phase is one of the rate-limiting processes because the oxide-ion conductivity is several orders lower than the electron conductivity and the gas diffusivity. Therefore, the YSZ tortuosity factor has a significant influence on the anode performance. Improving the transport through the phase is one of the most effective approach to optimize the anode microstructure.

3. In a typical SOFC anode composed of particles with around 1 μm diameter, the state of the mass transport in the pore phase is in the transient region between the molecular diffusion and the Knudsen diffusion. Aiming to improve the electrochemical activity

of the anode, it is often considered effective to decrease the particle sizes for achieving higher TPB density in the anode. However, smaller particle size also results in increasing the effect of the Knudsen diffusion, which causes significant decrease of the effective gas diffusivity. Therefore, the balance between these opposite influences needs to be carefully considered for the optimization of the microstructure.

4. If the gas diffusivity in the anode is secured, the increase in the TPB density has a positive influence on the anode performance. Also, the active reaction region is affected by the TPB density; the more reaction sites are contained in the anode, the thinner the active thickness becomes.

5. According to the error assessment, the errors in the anode overpotential associated with the those in the microstructural characterization are estimated at most 5%, which poses no significant problem on the discussion in this chapter.

Bibliography

[1] J.H. Nam, D.H. Jeon, A Comprehensive Micro-Scale Model for Transport and Reaction in Intermediate Temperature Solid Oxide Fuel Cells, *Electrochimica Acta* **51** (2006) 3446–3460.

[2] H. Zhu, R.J. Kee, Modeling Distributed Charge-Transfer Processes in SOFC Membrane Electrode Assemblies, *Journal of The Electrochemical Society* **155**(7) (2008) B715–B729.

[3] D. Chen, W. Bi, W. Kong, Z. Lin, Combined micro-scale and macro-scale modeling of the composite electrode of a solid oxide fuel cell, *Journal of Power Sources* **195** (2010) 6598–6610.

[4] U. Anselmi-Tamburini, G. Chiodelli, M. Arimondi, F. Maglia, G. Spinolo, Z.A. Munir, Electrical Properties of Ni/YSZ Cermets Obtained Through Combustion Synthesis, *Solid State Ionics* **110** (1998) 35–43.

[5] N.F. Bessette II, W.J. Wepfer, J. Winnick, A Mathematical Model of Solid Oxide Fuel Cell, *Journal of The Electrochemical Society* **142**(11) (1995) 3792–3800.

[6] E.A. Mason, A.P. Malinauskas, R.B. Evans III, Flow and Diffusion of Gases in Porous Media, *The Journal of Chemical Physics* **46**(8) (1967) 3199–3216.

[7] D. Aronšt, P. Schneider, Dynamic Transport of Multicomponent Mixtures of Gases in Porous Solids, *The Chemical Engineering Journal* **57** (1995) 91–99.

[8] E.N. Fuller, P.D. Schettler, J.C. Giddings, A New Method for Prediction of Binary Gas-Phase Diffusion Coefficients, *Industrial Engineering Chemistry Research* **58** (5) (1966) 19–27.

[9] R.H. Perry, Perry's Chemical Engineers' Handbook, 7th ed., McGraw-Hill, New York, 1981.

[10] M. Kaviany, Principles of Heat Transfer in Porous Media, Springer-Verlag, 1991.

[11] R.J. Gorte, J.M. Vohs, Catalysis in Solid Oxide Fuel Cells, *Annual Review of Chemical and Biomolecular Engineering* **2** (2011) 9–30

[12] J. Mizusaki, H. Tagawa, T. Saito, T. Yamamura, K. Kamitani, K. Hirano, S. Ehara, T. Takagi, T. Hikita, M. Ippommatsu, S. Nakagawa, K. Hashimoto, Kinetic Studies of the Reaction at the Nickel Pattern Electrode on YSZ in $H_2 - H_2O$ Atmospheres, *Solid State Ionics* **70/71** (1994) 52–58

[13] B. De Boer, Ph.D. thesis, SOFC Anode - Hydrogen Oxidation at Porous Nickel and Nickel/Yttria-Stabilized Zirconia Cermet Electrodes, *University of Twente*, The Netherland 1998.

[14] A. Bieberle, L.P. Meire, L.J. Gauckler, The Electrochemistry of Ni Pattern Anodes Used as Solid Oxide Fuel Cell Model Electrodes, *Journal of The Electrochemical Society* **148**(6) (2011) A646–A656.

[15] W.G. Bessler, M. Vogler, H. Stomer, D. Gerthsen, A. Utz, A. Weber, E. Ivers-Tiffee, Model Anodes and Anode Models for Understanding the Mechanism of Hydrogen Oxidation in Solid Oxide Fuel Cells, *Physical Chemistry Chemical Physics* **12** (2010) 13888–13903.

[16] T. Kawada, N. Sakai, H. Yokokawa, M. Dokiya, M. Mori, and T. Iwata, Characteristics of Slurry-Coated Nickel Zirconia Cermet Anodes for Solid Oxide Fuel Cells, *Journal of The Electrochemical Society* **137**(10) (1990) 3042–3047.

[17] N. Shikazono, D. Kanno, K. Matsuzaki, H. Teshima, S. Sumino, N. Kasagi, Numerical Assessment of SOFC Anode Polarization Based on Three-Dimensional Model Microstructure Reconstructed from FIB-SEM Images, *Journal of The Electrochemical Society* **157**(5) (2010) A665–A672.

[18] A. Konno, H. Iwai, M. Saito, H. Yoshida, Effect of Characteristic Lengths of Electron, Ion, and Gas Diffusion on Electrode Performance and Electrochemical Reaction Area in a Solid Oxide Fuel Cell, *Heat Transfer Asian Research* **DOI**: 10.1002/htj.20373.

[19] Y. Suzue, N. Shikazono, N. Kasagi, Micro Modeling of Solid Oxide Fuel Cell Anode Based on Stochastic Reconstruction, *Journal of Power Sources* **184** (2008) 52–59.

[20] M. Brown, S. Primdahl, M. Mogensen, Structure/Performance Relations for Ni/Yttria-Stabilized Zirconia Anodes for Solid Oxide Fuel Cells. *Journal of The Electrochemical Society* **147**(2) (2000) 475-485.

Chapter 4

Three-Dimensional Numerical Simulation in Porous Anode Based on Sub-Grid-Scale Modeling of Microstructure

4.1 Introduction

In the previous chapter, one-dimensional numerical simulation is carried out with the microstructural parameters of the porous anode and successfully reproduces the overall electrochemical performance of the anode. The one-dimensional simulation has an advantage in computational cost, and hence, can be applied to parametric studies of the electrodes, such as the sensitivity analysis conducted in the previous chapter. However, development of reliable three-dimensional numerical simulation technique using the real porous microstructure is also required for more detailed understanding of the phenomena occurring in the complex porous structure. For example, as suggested in Chapter 3, the steam partial pressure is possibly higher in the vicinity of the TPB because of the electrochemical oxidation of hydrogen, which affect the kinetics of the electrochemical reaction around the TPB. Such inhomogeneity in the electrodes cannot be represented by the models using homogenized structure. Moreover, morphologic change of the porous microstructure is considered to occur during the long-term operation of SOFCs, which causes degradation in electrode/cell performance. For example, coarsening of metal particles is an inevitable phenomenon in high-temperature operation [1–5], which worsens the connectivity of the metal phase, resulting in making the

TPB inactive. In order to deal with such structure changes, the use of the three-dimensional structure for the computational domain is required.

Development of the three-dimensional simulation techniques with the real electrode microstructure has been intensively carried out since the direct observation with the FIB-SEM became available. The lattice-Boltzmann-method-based simulation is applied to the electrode simulation by the University of Tokyo group [6–8]. The LBM is considered to be suitable for simulating complicated multiphase porous electrodes because the handling of the boundary conditions at the phase boundaries is relatively simpler than other methods. The volume of fluid (VOF) method is employed by Imperial College London group [9, 10] to predict the anode overpotential and they estimate the active reaction thickness in the anode, which is important in optimizing the electrode microstructure. Application of the commercial softwares based on the finite element method (FEM), such as COMSOL [11, 12] and Parcell3D [13] is also found in literatures. However, improvement and validation of the simulation techniques are still required for more reliable prediction of the performance and durability of the porous electrodes.

The accuracy of the three-dimensional numerical simulation in SOFC electrodes basically depends on two aspects: the electrochemical reaction model and the structure model. For the modeling of the electrochemical reaction around the TPB, many experimental approaches have been conducted focusing on the elementary electrochemical reaction on the catalytic surface in the electrodes [14–18]. Some of the findings were summarized into numerical models, which are available for the numerical simulation [19–22]. For the structure model, on the other hand, many porous models have been developed to mimic the complex electrode microstructure [20, 23–25]. For example, the random-spherical packing model [23, 24] assumes that the porous structure is composed of two kinds of spheres, representing electron-conductive particles and ion-conductive particles, which are randomly distributed in the field. From the obtained structure, microstructural parameters such as the phase connectivity and the TPB density can be obtained. However, these structure models require assumptions for the structural configuration, and hence, they cannot always represent the heterogeneous nature of the complex porous structure.

Recent advance in the three-dimensional tomography such as the FIB-SEM has been promoting the development of the simulation techniques based on the real three-dimensional

microstructure. In such analyses, however, the computational load often becomes a critical issue when the obtained voxel-based structure is directly used for the numerical grid system. The elemental image voxel in the FIB-SEM observation is usually several tens of nanometers in size; therefore, the total number of grids tends to reach to the order of a hundred million, which is unrealistic for the grid system considering the reasonable computational resources. Currently, it is a common practice to resample the original voxel-based dataset to reduce the number of calculation grid. The resampling process, however, raises a question as to whether the resampled dataset is still a good representation of the original microstructure because it inevitably results in the loss of the structural information that is smaller than the calculation grid size (sub-grid-scale information).

In this chapter, the use of a sub-grid-scale (SGS) model will be proposed in order to maintain the quality of the original structural information intact in the resampled structure used for the calculation grid system. In the proposed SGS models, the local transport coefficients in the grids will be evaluated with the local information of the porous structure, such as the volume fractions and the structural complexity. The effect of the SGS model on the numerical simulation will be extensively investigated through a diffusion analysis in the porous structure, and their effect and applicability will be evaluated.

4.2 Model Concepts

In this chapter, a numerical simulation with the three-dimensional porous anodes obtained with the FIB-SEM is conducted. In order to evaluate the proposed SGS models in terms of how precisely they can maintain the structural information of the original porous structure, an indicator is required to characterize both the original porous structure and the resampled structure used for the calculation grid system. For this purpose, the tortuosity factor is the most appropriate microstructural parameter because it directly represents the complexity of the porous structure. Two different quantification methods are applied to the original porous structure and the resampled structure as follows.

For the original porous structure, the random-walk-based diffusion simulation (RW) is applied. This method is specialized for evaluating the tortuosity factor from the voxel-based structure data such as that obtained with the FIB-SEM. Since the requirement for the

computational resources is much smaller than that for other approaches, resampling is not necessary. The accuracy of this method has been proved in the previous chapter. Therefore, it can be assumed that the tortuosity factor obtained with the random-walk simulation truly represents the structural complexity of the original porous structure. In the later discussion, the values obtained from this simulation are used as a reference.

For the resampled structure used as the grid system, on the other hand, the diffusion simulation based on the finite volume method (FVM) aided by various SGS models is applied. Although the in-house code used in this study is capable of conducting the overpotential analysis by considering the electrochemical reaction at the TPB, only transport analysis is enough to investigate the effect of the proposed SGS models. Fig. 4.1 shows the schematic diagram of the grid generation for the FVM analysis using the SGS models. As is often adopted in most studies, the original porous structure is resampled to have a lower spatial resolution. The unique strategy used in this study is that the structural information inside the grid is reflected onto the resampled structure in the form of the effective transport coefficients. In the figure, the following length ratio is introduced as a parameter to generally evaluate the grid size:

$$\frac{L_l}{L_{\mathrm{grid}}} \tag{4.1}$$

where L_l is the characteristic scale of the phase l evaluated with the line-intercept method, and L_{grid} is the grid size used in the simulation, which is defined as follows:

$$L_{\mathrm{grid}} = \sqrt[3]{\Delta x \Delta y \Delta z} \tag{4.2}$$

where Δx, Δy, and Δz are the grid sizes in each direction. The value of L_l/L_{grid} is interpreted as the number of grids used to resolve a typical structure of a porous material, in other words, one particle. If the grid size is smaller or L_l/L_{grid} is larger, it can be expected that the grid-scale information (resampled structure without the SGS model) represents the structural complexity. On the other hand, if the grid size is larger or L_l/L_{grid} is smaller, the proposed SGS models need to exert their effects to maintain the sub-grid-scale information in the resampled structure.

If the tortuosity factor obtained with the FVM-based diffusion simulation is the same as that obtained with the random-walk simulation, it can be judged that the resampled structure reasonably maintains the quality of the original structure.

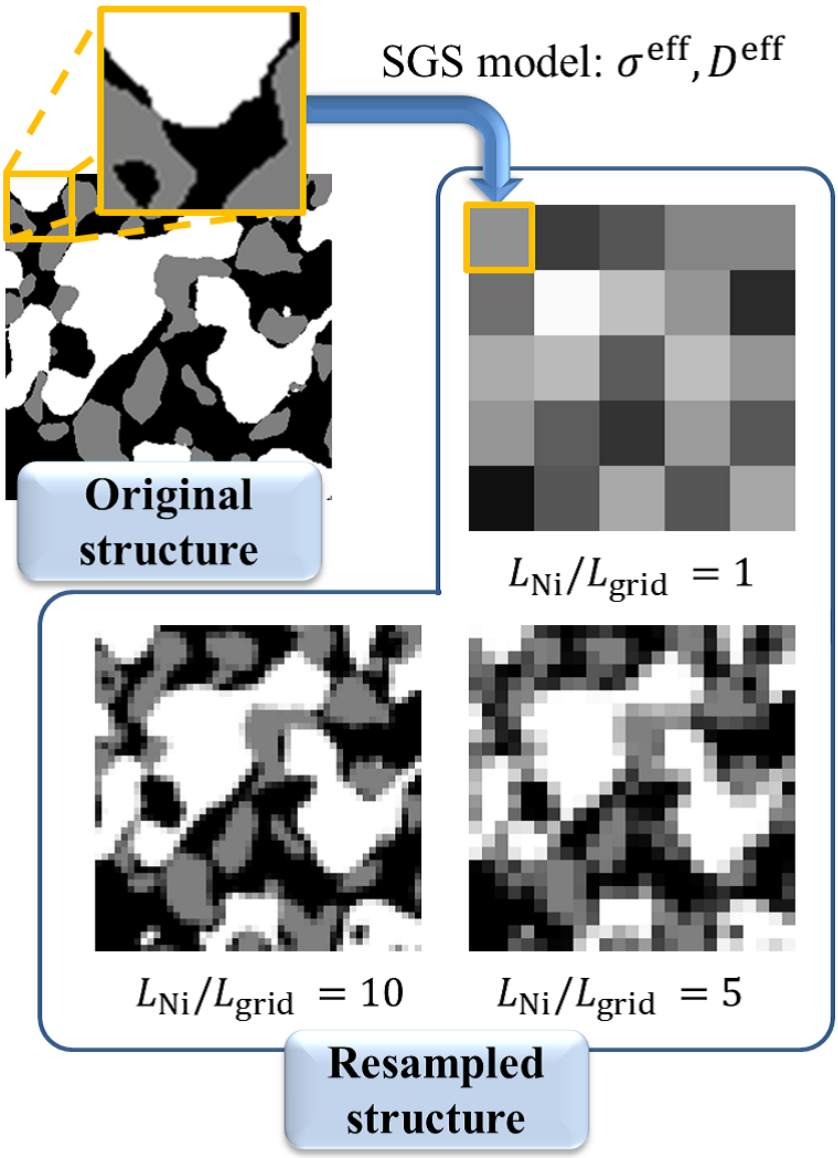

Fig. 4.1. Schematic diagram of the grid generation for the FVM analysis using the SGS models.

4.3 FVM-based Diffusion Simulation

In this chapter, three different anodes, Ni:YSZ = 70:30, 50:50, and 30:70 presented in Chapter 2, are used for the analysis. To evaluate the structural complexity represented by the grid system, a simple diffusion simulation is conducted based on the FVM.

4.3.1 Governing equation

The following generalized diffusion equation is adopted:

$$\nabla \cdot \left(\Gamma_l^{\mathrm{eff,local}} \nabla \varphi_l \right) = 0 \tag{4.3}$$

where φ_l is an arbitrary potential, which corresponds to the electric potential or gas concentration in the actual SOFC electrodes. $\Gamma_l^{\mathrm{eff,local}}$ is the "local" transport coefficient, which is defined at each calculation grid and includes the local structural information evaluated with the SGS models. A detailed description of the SGS models is provided in the next section. The potential difference is set on the two facing edge surfaces of the calculation domain and induce flux through the calculation domain (Fig. 4.2). From the amount of the induced flux, the effective transport coefficient of the phase l, Γ_l^{eff}, in the whole calculation domain is obtained, and the tortuosity factor of the phase is subsequently obtained as follows:

$$\tau_l = V_l \frac{\Gamma_l^{\mathrm{bulk}}}{\Gamma_l^{\mathrm{eff}}} \tag{4.4}$$

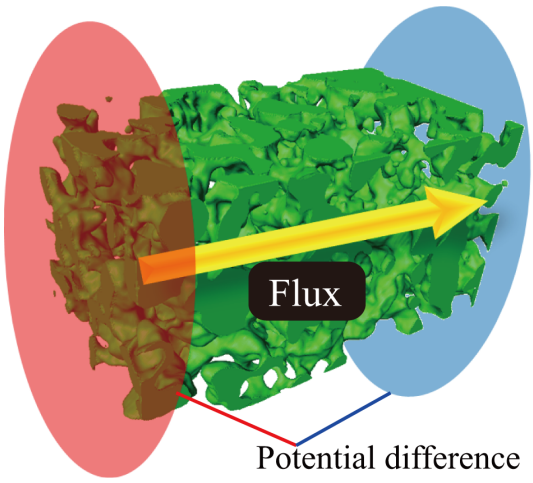

Fig. 4.2. Schematic picture of the FVM-based diffusion simulation.

4.3.2 Sub-grid-scale model

4.3.2.1 SGS1: Volume conservation

As the simplest SGS model, the conservation of the phase volume is considered in each grid (SGS1). Schematic picture of the model concept is shown in Fig. 4.3(a). The numbers of voxels corresponding to the Ni, YSZ, and pore phases are separately counted and the volume fractions are obtained, with which the local transport coefficients $\Gamma_l^{\mathrm{eff,local}}$ are evaluated in each grid as follows:

$$\Gamma_l^{\mathrm{eff,local}} = V_l^{\mathrm{local}} \Gamma_l^{\mathrm{bulk}} \tag{4.5}$$

where Γ_l^{bulk} is the bulk transport coefficient and V_l^{local} is the volume fraction of the phase l in the grid. In this study, Γ_l corresponds to the electron conductivity in the Ni phase (σ_{el}), the oxide-ion conductivity in the YSZ phase (σ_{io}), or the gas diffusivities in the pore phase ($D_{lm}, D_{l,\mathrm{K}}$).

In the FVM, any transport between two neighboring grids occurs through the interface they share. Since the local transport coefficients of the two grids are generally different, an averaged transport coefficient between the two grids needs to be evaluated to calculate the transport flux through the interface. Since an equally spaced grid system is used in this study, it is evaluated as a harmonic average of the effective transport coefficients of the two neighboring grids. The following formula shows the averaged effective transport coefficient between the grid (i, j, k) and grid $(i + 1, j, k)$

$$\Gamma_{l,\left(i+\frac{1}{2},j,k\right)}^{\mathrm{eff,local}} = \left(\frac{1}{\Gamma_{l,(i,j,k)}^{\mathrm{eff,local}}} + \frac{1}{\Gamma_{l,(i+1,j,k)}^{\mathrm{eff,local}}} \right)^{-1} \tag{4.6}$$

Note that the LHS of eq. (4.6) is defined at the location of $i + 1/2$, which corresponds to the interface of the grid (i, j, k) and grid $(i + 1, j, k)$. The transport coefficients at the other interfaces are also defined with a similar formula.

Also, TPB density and pore diameter are locally evaluated in each grid. The TPB is detected as edge lines among the Ni, YSZ, and the pore voxels, and the sum of the length is measured in each grid. This method, however, overestimates the total TPB length because the actual TPB has much smoother shape. Therefore, the scaling correction is applied to match the total TPB length with that obtained from the whole anode region with the volume expansion method. Pore diameter is evaluated with the line intercept method.

4.3.2.2 SGS2: Interfacial connectivity

For the further improvement of the SGS model, it is required to consider the effect of the structural complexity on the transport phenomena, especially when relatively coarse grid system is used. In macro-scale, this effect is generally evaluated by the tortuosity factor; however it is difficult and time-consuming to locally evaluate the tortuosity factor in every grid. For the development of a reliable SGS model, it is important to establish a simple and effective way to locally evaluate the structural complexity.

In the original image voxels, the structural complexity is ascribed to the connectivity of neighboring voxels. If the phases of two neighboring voxels are the same, they are connected and if not, the connectivity is zero. As a result of considering this on/off-type local connectivity for all voxels in the dataset, the macroscopic complexity is expressed. In the SGS2, this expression of the structural complexity is extended to the simulation grid. The difference is that because the simulation grid may contain multiple image voxels, the connectivity of two neighboring grids are evaluated not with the simple on/off-type connectivity but with the surface fraction of the conductive phase on a grid interface. This is considered as an attempt to evaluate the structural complexity with the surface information of the grid. It is worth noting that the complexity expression using the surface information matches to the finite volume method, in which the transport of physical quantities between neighboring two grids is evaluated at the interface; hence, evaluation of the effective transport coefficient on each interface is a key issue. By taking the grid connectivity into account, SGS2 is expected to better describe the effects of structural complexity on the transport phenomena than SGS1. The concept of the model is schematically illustrated in Fig. 4.3(b). First, effective transport coefficients in each grid are evaluated with eq. (4.5), and then the value at the interface is evaluated by using the surface fractions of the conductive volume. Following formula shows the averaged effective transport coefficient at the interface between grid (i, j, k) and grid $(i + 1, j, k)$ as an example.

$$\Gamma^{\mathrm{eff,local}}_{l,\left(i+\frac{1}{2},j,k\right)} = \frac{S_{l,\left(i+\frac{1}{2},j,k\right)}}{S_{\mathrm{all},\left(i+\frac{1}{2},j,k\right)}} \left(\frac{1}{\Gamma^{\mathrm{eff,local}}_{l,(i,j,k)}} + \frac{1}{\Gamma^{\mathrm{eff,local}}_{l,(i+1,j,k)}} \right)^{-1} \tag{4.7}$$

where S_{all} is the total surface area of the grid interface and S_l is the surface area of the phase l on the grid interface. The transport coefficients at the other interfaces are also defined with similar formula.

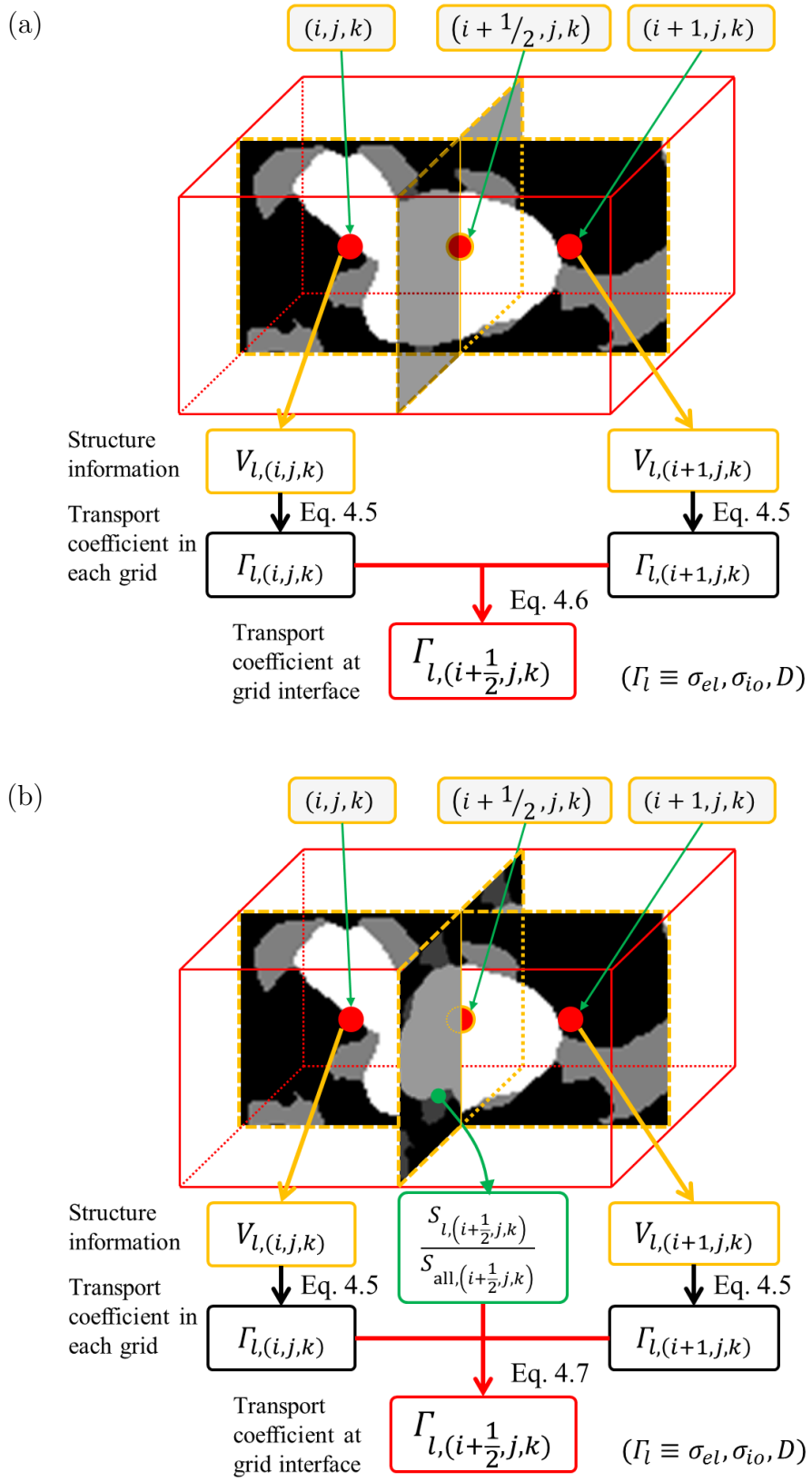

Fig. 4.3. Schematic pictures of the sub-grid scale models. (a) SGS1 (b) SGS2.

4.3.2.3 SGS3: Power low with a constant power index

Before the three-dimensional observation of the porous structure became available with the help of the FIB-SEM and the X-ray CT technologies, porous models had been used to mimic the porous structure. In these models, the macroscopic tortuosity factor is often evaluated with the following empirical formula:

$$\Gamma_l^{\mathrm{eff}} = V_l^{\gamma} \Gamma_l^{\mathrm{bulk}} \tag{4.8}$$

where γ is the Bruggeman factor, which represents the state of the tortuous conduction pathways in the structure. A fully percolated network with a straight conduction pathway is represented as $\gamma = 1$. Since the conduction pathways inside the porous structure are complicated and tortuous, the Bruggeman factor is over unity, and usually assumed to be 1.5–2.0 [24]. In the SGS3, the above macroscopic expression is adopted to evaluate the local tortuosity factor in each calculation grid:

$$\Gamma_l^{\mathrm{eff,local}} = \left(V_l^{\mathrm{local}}\right)^{\gamma} \Gamma_l^{\mathrm{bulk}} \tag{4.9}$$

The volume fraction, V_l^{local} in eq. (4.9) is individually evaluated in each calculation grid, while V_l in eq. (4.8) is evaluated from the whole structure. Eq. (4.9) is equivalent to the following formula, where the local tortuosity factor term is shown explicitly:

$$\Gamma_l^{\mathrm{eff,local}} = \frac{V_l^{\mathrm{local}}}{\tau_l^{\mathrm{local}}} \Gamma_l^{\mathrm{bulk}}, \quad \tau_l^{\mathrm{local}} = \left(V_l^{\mathrm{local}}\right)^{1-\gamma} \tag{4.10}$$

where τ_l^{local} is the local tortuosity factor modeled by the SGS3. The local transport coefficient on a grid interface is evaluated with eq. (4.6). It should be noted that the SGS3 is equivalent to the SGS1 when the Bruggeman factor is unity.

4.3.2.4 SGS4: Power low with an adaptive power index

When the original porous structure is resampled to make a grid system, heterogeneous nature inside the grid significantly depends on the grid size. When the grid size is larger, each grid can contain several solid particles so that relatively complicated transport pathways can be created inside the grid. On the other hand, when the grid size is smaller, each grid can contain only a part of the solid particles; hence the transport pathways inside the grid are less complicated. Therefore, it may be preferable to vary the effect of the SGS models depending

on the grid size used in the simulation. In the SGS4, the relationship between the grid size and the characteristic scale of the porous structure is taken into account. In this sense, it is reasonable to include the length ratio L_l/L_{grid} into the SGS model; the Bruggeman factor in the SGS3 is considered as the adoptive power index that depends on the ratio for further improvement of the SGS model.

The local transport coefficient and the local tortuosity factor are defined as follows:

$$\Gamma_l^{\mathrm{eff,local}} = \frac{V_l^{\mathrm{local}}}{\tau_l^{\mathrm{local}}}\Gamma_l^{\mathrm{bulk}}, \quad \tau_l^{\mathrm{local}} = \left(V_l^{\mathrm{local}}\right)^{1-f\left(\frac{L_l}{L_{\mathrm{grid}}}\right)} \tag{4.11}$$

where f is a function representing the dependency of γ on the length ratio. The derivation of the function is described later.

4.4 Results and Discussion

4.4.1 Microstructural parameters

Microstructural parameters of the anode structures have been already summarized in Chapter 2. Here, some of the parameters related to this analysis are briefly reproduced. Table 4.1 shows the sample sizes and voxel sizes of the anode samples. A region larger than 10 μm^3 is successfully obtained for each anode sample. Table 4.2 shows the volume fraction of the anode samples. The ratios of the Ni and YSZ volume fractions, which are Ni:YSZ = 31.8:68.2, 53.5:46.5, and 69.1:30.9, respectively, are close to the intended values, which indicates the observed region is large enough to be representative of the whole anode structure. Table 4.3 shows the anisotropic tortuosity factors quantified with the random-walk simulation. Since some of the phases have no percolating cluster in a specific direction, tortuosity factors cannot be evaluated. In the following discussion, the tortuosity factors in Z direction are used as the reference values. Table 4.4 shows the average particle/pore sizes measured by the line intercept method. These particle/pore diameters are used as the characteristic scale of the porous component, L_l.

4.4.2 Grid system

Table 4.5 shows the information of the grid systems used in the numerical analysis. The grid size L_{grid} and the length ratio L_l/L_{grid} is also shown. The effect of the grid size can be clearly presented in Fig. 4.4 that shows the distributions of the Ni volume fraction of

Table 4.1. Sample sizes and voxel sizes.

	Sample size [μm]			Voxel size [nm]		
Sample	X	Y	Z	X	Y	Z
Ni:YSZ = 70:30	18.0	13.2	10.5	30.0	30.0	52.3
Ni:YSZ = 50:50	18.1	9.72	9.97	34.7	34.7	62.3
Ni:YSZ = 30:70	18.8	11.6	10.1	36.2	36.2	42.2

Table 4.2. Volume fractions [%].

Sample	Ni	YSZ	Pore	Ni:YSZ
Ni:YSZ = 70:30	42.3	18.9	38.8	69.1:30.9
Ni:YSZ = 50:50	34.2	29.7	36.1	53.5:46.5
Ni:YSZ = 30:70	23.6	50.6	25.8	31.8:68.2

Table 4.3. Anisotropic tortuosity factors.

	Ni			YSZ			Pore		
Sample	X	Y	Z	X	Y	Z	X	Y	Z
Ni:YSZ = 70:30	2.79	2.41	1.85	–	–	14.1	3.26	2.71	2.27
Ni:YSZ = 50:50	4.91	3.43	3.79	7.93	5.63	5.39	3.48	3.04	2.64
Ni:YSZ = 30:70	–	78.3	–	1.71	1.57	2.57	6.17	3.92	10.8

Table 4.4. Average particle/pore sizes [μm].

Sample	Ni	YSZ	Pore
Ni:YSZ = 70:30	2.55	1.11	2.19
Ni:YSZ = 50:50	1.60	1.16	1.32
Ni:YSZ = 30:70	1.34	1.74	1.39

the Ni:YSZ = 50:50 anode in Grid 1 and Grid 5. The grid size of Grid 1 is comparable to the characteristic scale of the original porous structure. As shown in Fig. 4.4(a), Grid 1 no more maintains the details of the original structure. On the other hand, Grid 5 clearly represents the porous network in the original structure (Fig. 4.4(b)). The portion of the grids containing more than two phases is small but they tend to exist at the important locations: the boundaries of different phases. Note that the grid size of Grid 5 is comparable to that used in the three-dimensional simulation by Shikazono et al. [6]

In order to show one aspect of the relationships between the grid and the original microstructure, the volume fractions of the Ni:YSZ = 50:50 anode are shown as histograms in Fig. 4.5. When the volume fraction V_l is unity, the grid is fully occupied by the phase of interest. When the phase of interest is not included in the grid, the volume fraction is zero. In the extreme case where the original image voxel is used as the calculation grid, V_l

is either unity or zero in every grid. As shown in Table 4.5, the grids used in the present calculation are always larger than the original image voxel. As the grid size becomes larger, two or more phases tend to be included in one grid and the portion of $V_l = 0$ or 1 decreases. Moreover, in the case of Grid 1, which is the coarsest grid in this study, the distributions seem to have peaks, and the peak values are close to the values of the global microstructural parameters quantified in Chapter 2. The proposed SGS models are required to exert their effect especially in the coarser grid cases, where one grid includes two or more phases.

Table 4.5. Grid information.
(a) Ni:YSZ = 70:30

	Size [μm]			L_{grid} [μm]	L_l/L_{grid}		
Grid	X	Y	Z		Ni	YSZ	Pore
Grid 1	1.200	1.200	1.045	1.146	2.23	0.97	1.91
Grid 2	0.600	0.600	0.523	0.573	4.45	1.94	3.82
Grid 3	0.300	0.300	0.261	0.287	8.90	3.87	7.64
Grid 4	0.150	0.150	0.105	0.133	19.18	8.35	16.47
Grid 5	0.060	0.060	0.052	0.057	44.50	19.37	38.22

(b) Ni:YSZ = 50:50

	Size [μm]			L_{grid} [μm]	L_l/L_{grid}		
Grid	X	Y	Z		Ni	YSZ	Pore
Grid 1	1.388	1.388	1.246	1.339	1.40	1.01	1.16
Grid 2	0.694	0.694	0.623	0.670	2.79	2.02	2.31
Grid 3	0.347	0.347	0.312	0.335	5.59	4.03	4.63
Grid 4	0.174	0.174	0.125	0.155	12.03	8.69	9.97
Grid 5	0.069	0.069	0.062	0.067	27.93	20.16	23.15

(c) Ni:YSZ = 30:70

	Size [μm]			L_{grid} [μm]	L_l/L_{grid}		
Grid	X	Y	Z		Ni	YSZ	Pore
Grid 1	1.449	1.449	1.689	1.525	0.88	1.14	0.91
Grid 2	0.725	0.725	0.844	0.763	1.76	2.28	1.82
Grid 3	0.362	0.362	0.422	0.381	3.51	4.56	3.65
Grid 4	0.181	0.181	0.211	0.191	7.03	9.13	7.29
Grid 5	0.072	0.072	0.084	0.076	17.57	22.82	18.23

(a)

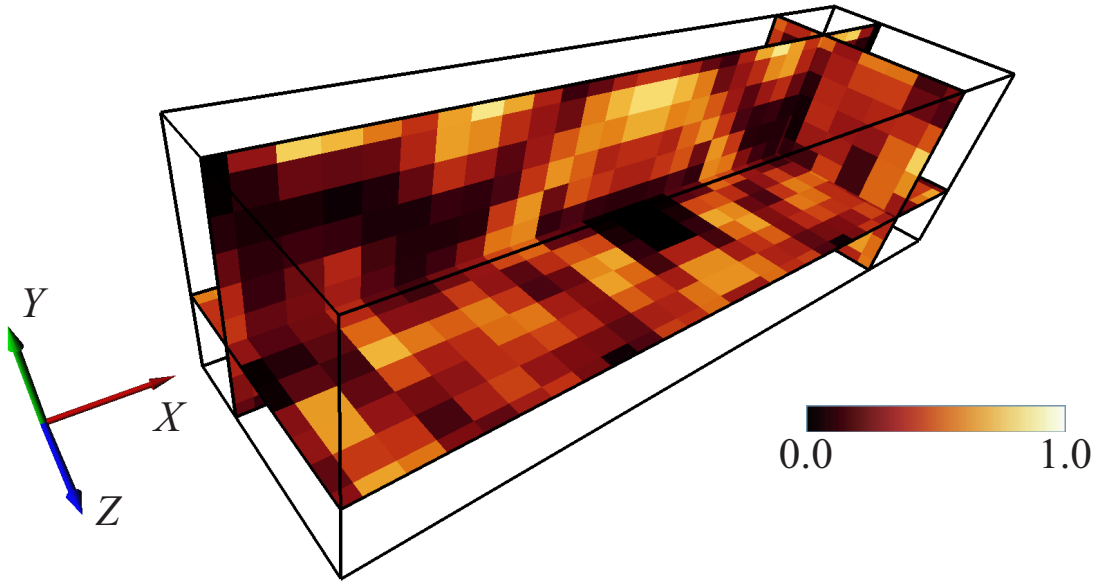

(b)

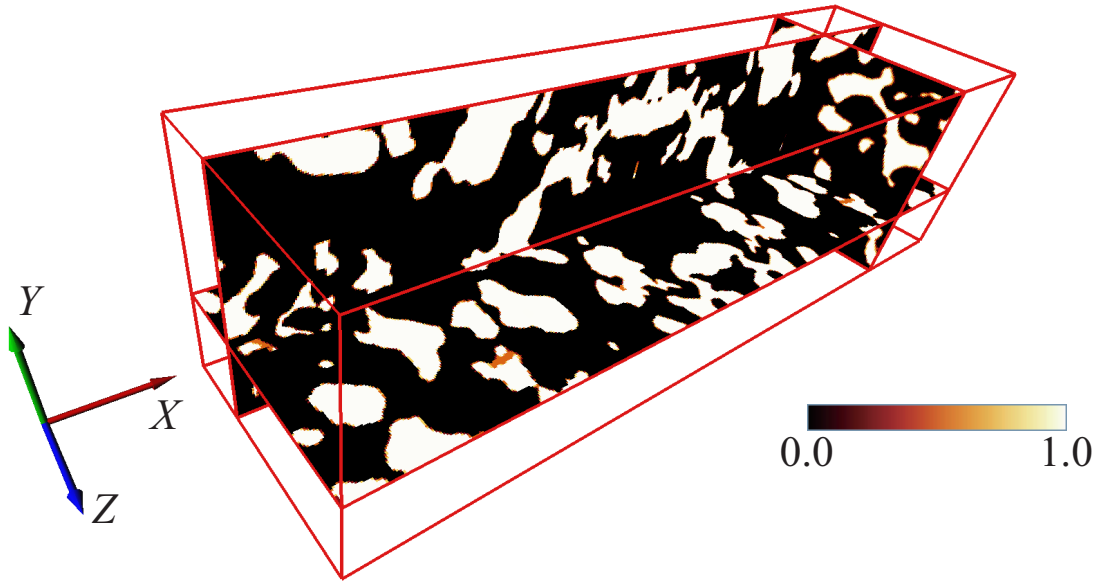

Fig. 4.4. Distribution of the Ni volume fraction in the Ni:YSZ = 50:50 anode. (a) Grid 1 (b) Grid 5.

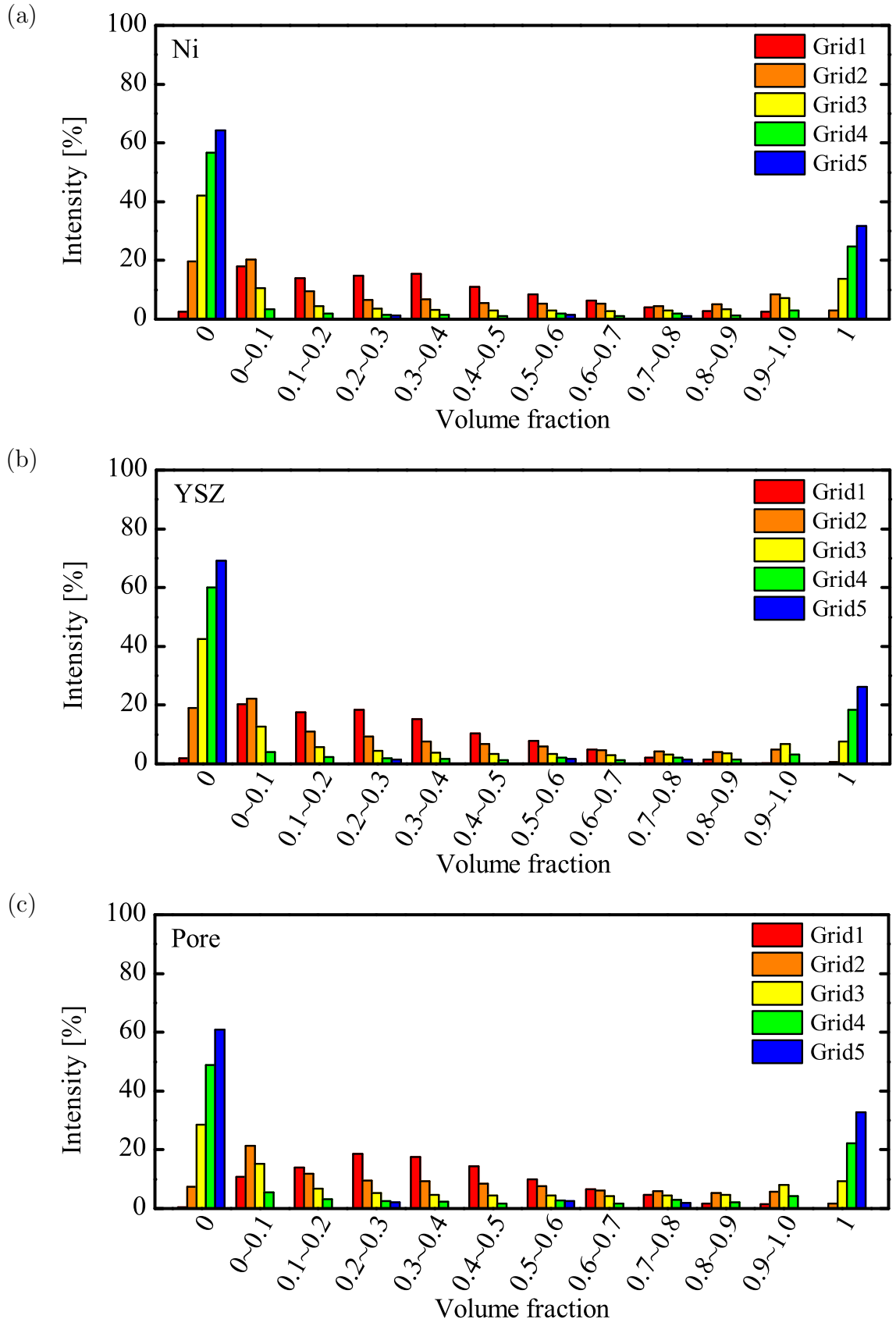

Fig. 4.5. Histograms of the volume fractions in the Ni:YSZ = 50:50 anode. (a) Ni (b) YSZ (c) Pore.

4.4.3 Diffusion simulation

Fig. 4.6 shows the tortuosity factors obtained by the FVM-based diffusion simulation with the SGS1, 2, and 3. The tortuosity factors are normalized with the reference values obtained with the random-walk simulation. The length ratio L_l/L_{grid} is used for the horizontal axis to generally represent the grid size used in the simulation. In every SGS model, the tortuosity factors converge to unity as the grid size becomes smaller. This indicates that the effect of the structural complexity evaluated with the SGS models becomes smaller with finer grids and that the original porous structure can be represented simply by the volume fractions. In the case of coarser grids, on the other hand, only the volume conservation is not enough; hence, the sub-grid-scale information associated with the structural complexity significantly contributes to the representation of the original structure. However, since the method of evaluating the sub-grid-scale information is different among the SGS models, the trends of $\tau_{\mathrm{SGS}}/\tau_{\mathrm{RW}}$ are significantly different.

First, in the SGS1, the values of $\tau_{\mathrm{SGS}}/\tau_{\mathrm{RW}}$ monotonically increase to unity as the grid size becomes smaller. However, the tortuosity factors are significantly underestimated in the case of the coarser grids, indicating that only volume conservation is not enough to represent the original porous structure inside the grid. It is required to evaluate higher-order quantities associated with the heterogeneous nature of the porous structure for more sophisticated SGS model.

Second, in the SGS2, the local structural complexity is evaluated with the surface information of the grids. This approach results in drastic changes in the trends of $\tau_{\mathrm{SGS}}/\tau_{\mathrm{RW}}$. The values of $\tau_{\mathrm{SGS}}/\tau_{\mathrm{RW}}$ approach unity even in the case of the coarser grids. However, the extent of the effect is different from phase to phase. For example, in the case of the YSZ phase of the Ni:YSZ = 30:70 anode, the tortuosity factors are reasonably evaluated over a wide range of grid sizes. On the other hand, in the case of the YSZ phase of the Ni:YSZ = 70:30 anode, the value is significantly overestimated in the intermediate grid size region ($L_l/L_{\mathrm{grid}} \simeq 5$). These unsystematic behaviors of the SGS2 implies that the relationships between the surface information and the inner information are not straightforward; therefore, the SGS2 may not always be valid in a wide variety of porous structures.

Third, in the SGS3, the structural complexity inside a grid is evaluated by the volume

fraction and the Bruggeman factor γ, whose value is set 1.2, 1.5, or 1.8 in this study. This approach is to employ the macroscopic expression used in the conventional porous models (eq. (4.8)) on the evaluation of the local tortuosity factor (eq. (4.9)). When the value of γ is small, the structural complexity is still underestimated in the case of coarser grids; the trends observed in the graph are similar to those in the SGS1. However, simply increasing the value of γ is not an effective solution; the structural complexity tends to be overestimated in the case of the intermediate grids if a larger γ is applied. It is found to be difficult to properly represent the structural complexity over a wide range of grid sizes with a constant value of γ.

The SGS1, 2, and 3 discussed above show positive contributions to maintain the structural information in the resampled structure used as the calculation grid system. However, they are not always valid in a wide range of grid sizes; underestimation or overestimation is often observed. This is because the same formula is applied to all grid sizes. The heterogeneous nature inside the grids significantly varies with the grid sizes so that a tuning parameter is required to vary the effect of the SGS model depending on the grid size. This is the motivation to consider the Bruggeman factor γ as an adaptive power index in the SGS4.

In the SGS4, the local tortuosity factors are estimated with an adaptive power index γ that depends on the ratio between the characteristic length L_l and the grid size L_{grid}. In order to determine the dependency of γ on the length ratio L_l/L_{grid}, the Bruggeman factor γ is considered as a fitting parameter; an appropriate value of γ is determined with which the macroscopic structural complexity is properly evaluated, in other words, the value of $\tau_{\mathrm{SGS}}/\tau_{\mathrm{RW}}$ becomes unity. Fig. 4.7 shows the appropriate value of γ for each phase versus the length ratio L_l/L_{grid}. The calculation is conducted in all the phases in all the samples except the Ni phase of the Ni:YSZ = 30:70 anode. Although there is some extent of deviation, the graph reveals an apparent trend. When the value of L_l/L_{grid} is large enough or the grid size is small enough, γ converges to unity. This indicates that the structural information of the porous anode is represented simply by considering the volume conservation and that it is not necessary to rely on the sub-grid-scale information associated with the structural complexity when conducting the transport analysis. On the other hand, when the value of L_l/L_{grid} becomes smaller or the grid size becomes larger, γ tends to steeply increase up to around 2.5.

These results gives us an important criterion in making a calculation grid system for the simulation in porous electrodes. If the characteristic length of the porous structure (e.g. particle/pore diameter) is resoluted with more than 15 grids, the structural information of the porous electrodes can be represented by the grid-scale information. Otherwise, the SGS model needs to be applied to the resampled structure to maintain the quality of the structural information. In the anode overpotential analysis, where it is necessary to consider the transport in the three phases at the same time, the allowable maximum grid size without the SGS model is determined by the structure that has the smallest characteristic scale. For the Ni:YSZ = 70:30, 50:50, and 30:70 anodes used in this study, the grid size needs to be smaller than 74, 77, and 89 nm, respectively. However, it is not always possible to use such small grid sizes considering reasonable computational resources so that the aid of the SGS model is significantly important.

Considering the value of the Bruggeman factor must be larger than unity, the obtained values of γ is fitted on the following exponential decay function.

$$\gamma = A \exp\left(-\lambda \frac{L_l}{L_{\mathrm{grid}}}\right) + 1 \tag{4.12}$$

where A is a pre-exponential factor and λ is a decay constant. The solid line in Fig. 4.7 is the fitting curve, where $A = 1.44$ and $\lambda = 0.246$. The mean square deviation is 0.832. It is worth noting the structure data used in the fitting: the volume fraction of the phase is from 18.9 to 50.6%, which covers structures both over and below the percolation threshold of ordinary porous materials. The particle/pore size is from 1.11 to 2.55 μm, which is typical for SOFC electrode materials.

Fig. 4.8 shows the comparison of the effects among the various SGS models. All values of $\tau_{\mathrm{SGS}}/\tau_{\mathrm{RW}}$ obtained in all the phases of all the samples are shown in the graph. The SGS4 successfully makes the $\tau_{\mathrm{SGS}}/\tau_{\mathrm{RW}}$ much closer to unity than the other models. Structural complexity in the case of coarser grids is more accurately represented than the SGS1, and the overshoot observed in the SGS2 is moderated. Although the SGS4 does not give perfect values for $\tau_{\mathrm{SGS}}/\tau_{\mathrm{RW}}$ in all the cases, significant improvement is achieved. The attempt to include the length ratio L_l/L_{grid} in the SGS model has a positive contribution to developing a more sophisticated SGS model.

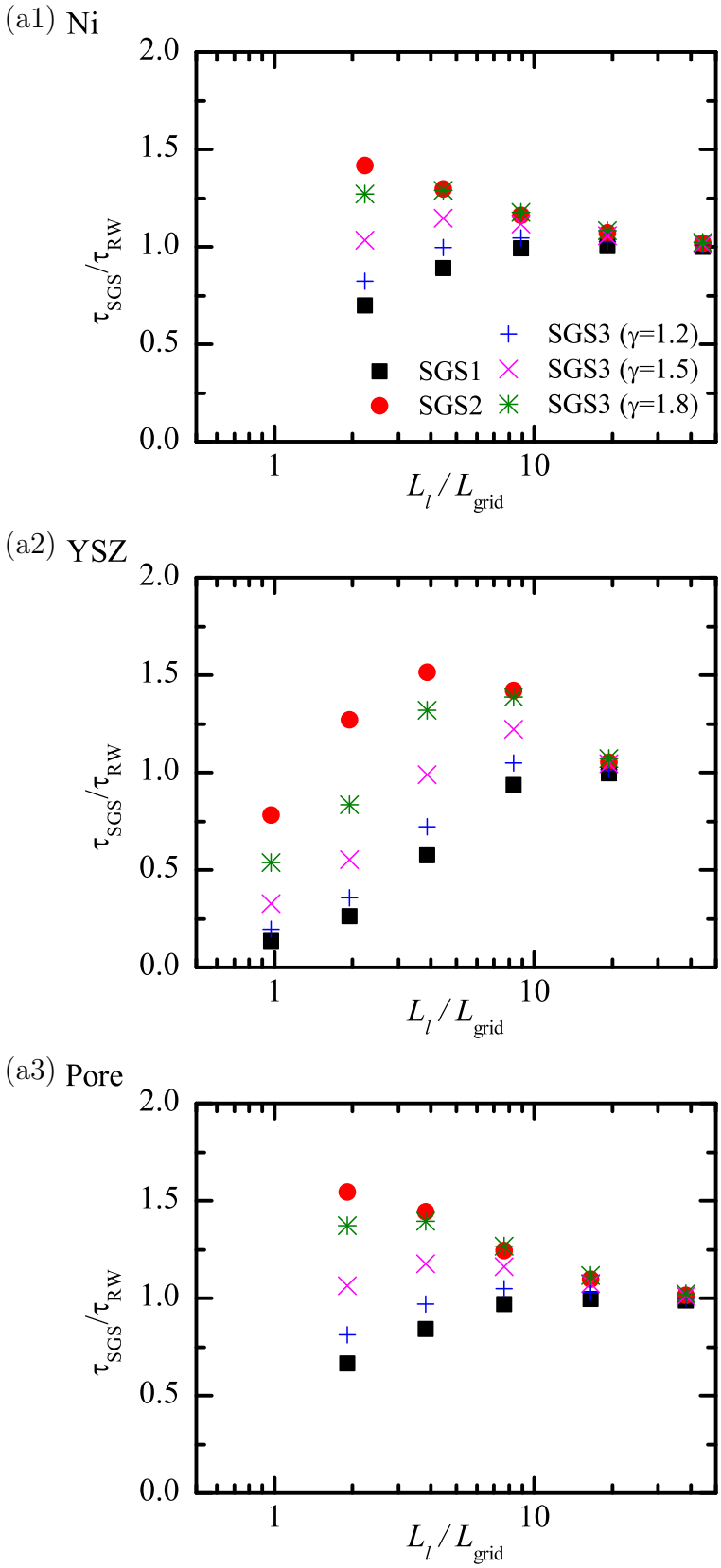

Fig. 4.6. (a) Tortuosity factors obtained by the FVM-based diffusion simulation normalized by the reference tortuosity factors obtained by the random-walk simulation. Ni:YSZ = 70:30 anode.

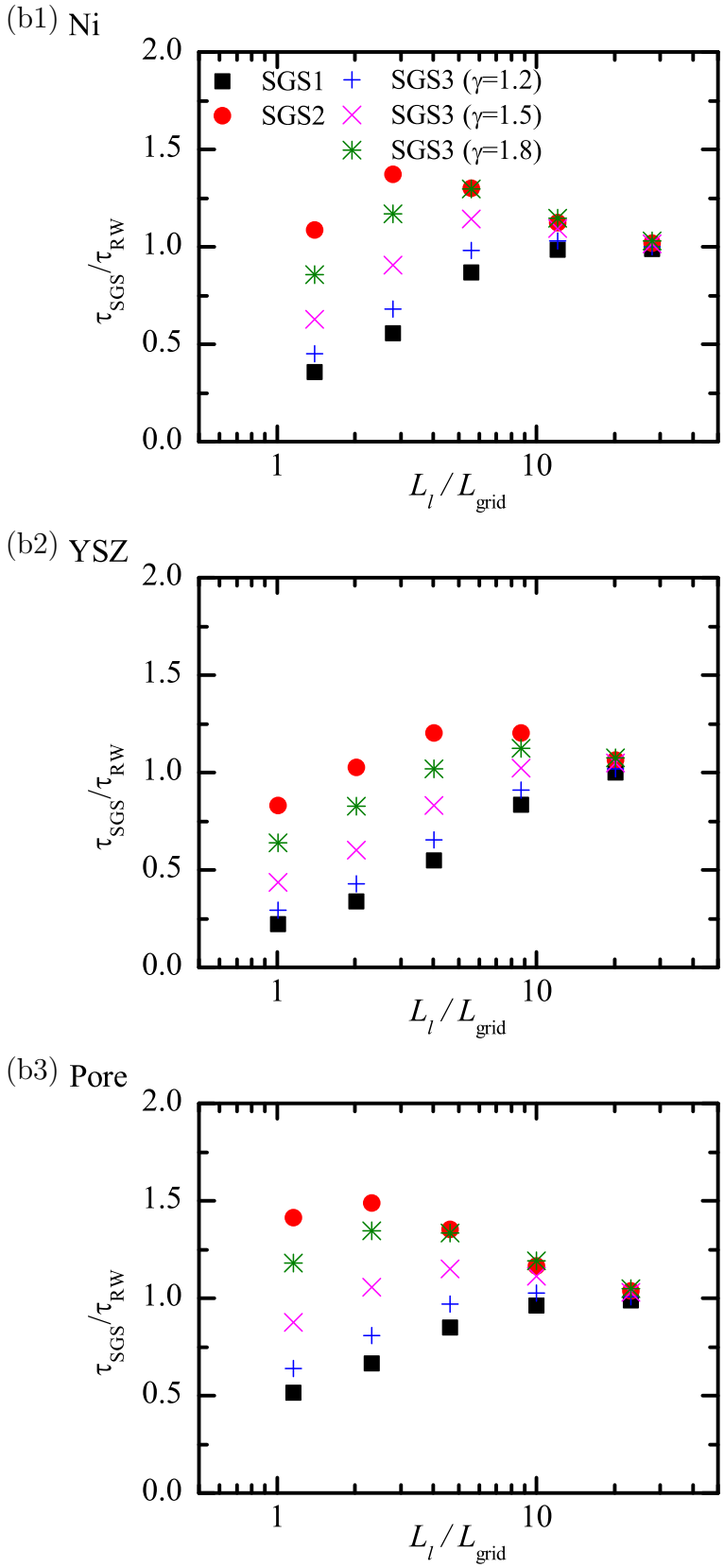

Fig. 4.6. (b) Tortuosity factors obtained by the FVM-based diffusion simulation normalized by the reference tortuosity factors obtained by the random-walk simulation. Ni:YSZ = 50:50 anode.

(c1) N/A

(c2) YSZ

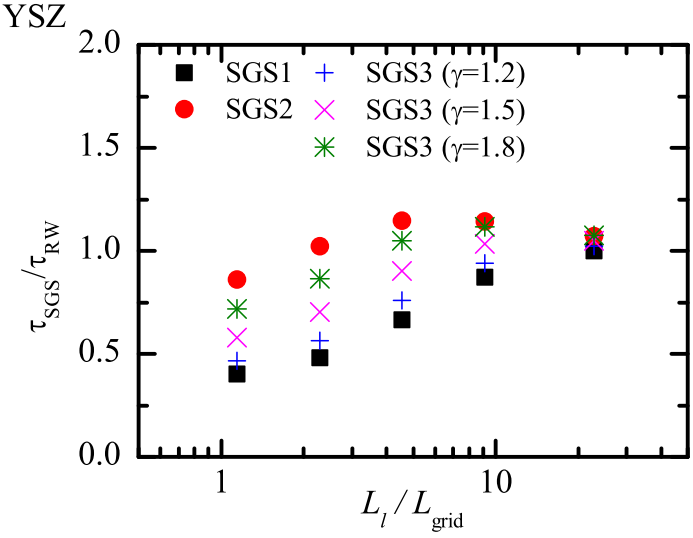

(c3) Pore

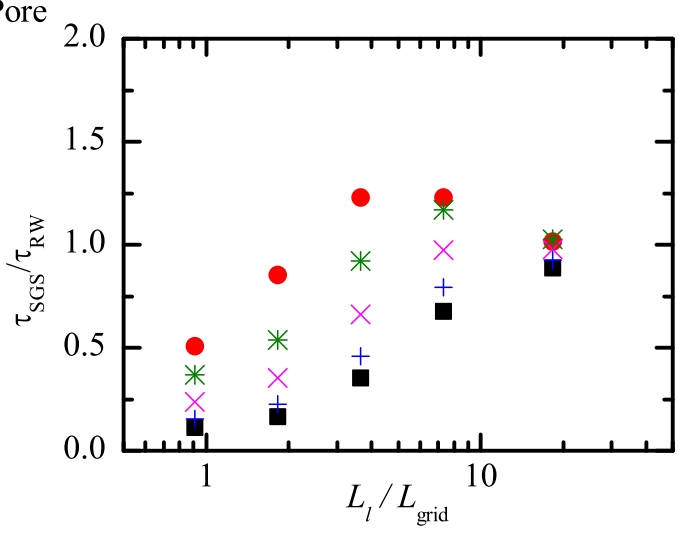

Fig. 4.6. (c) Tortuosity factors obtained by the FVM-based diffusion simulation normalized by the reference tortuosity factors obtained by the random-walk simulation. Ni:YSZ = 30:70 anode.

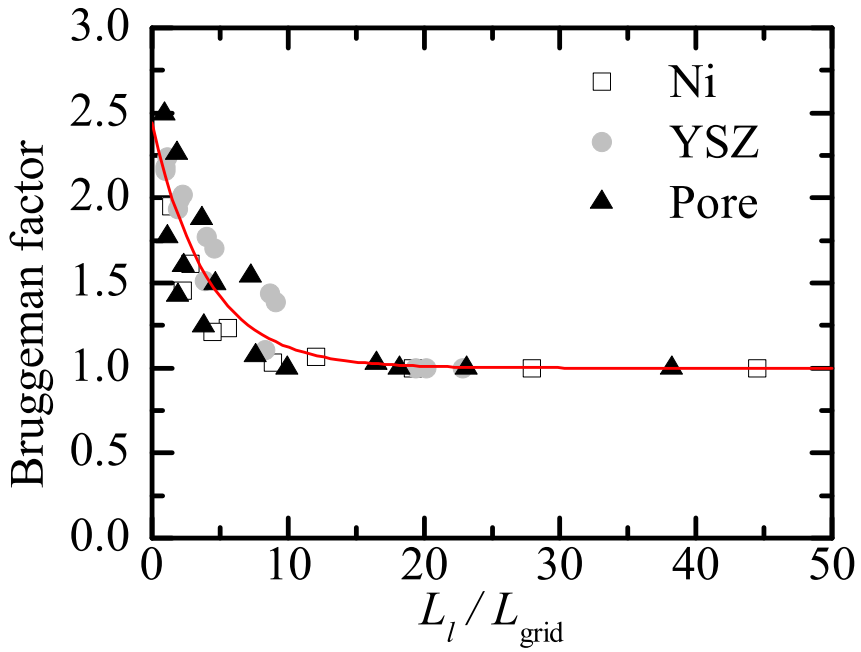

Fig. 4.7. Appropriate values for Bruggeman factor against the length ratio L_l/L_{grid} and its fitted curve.

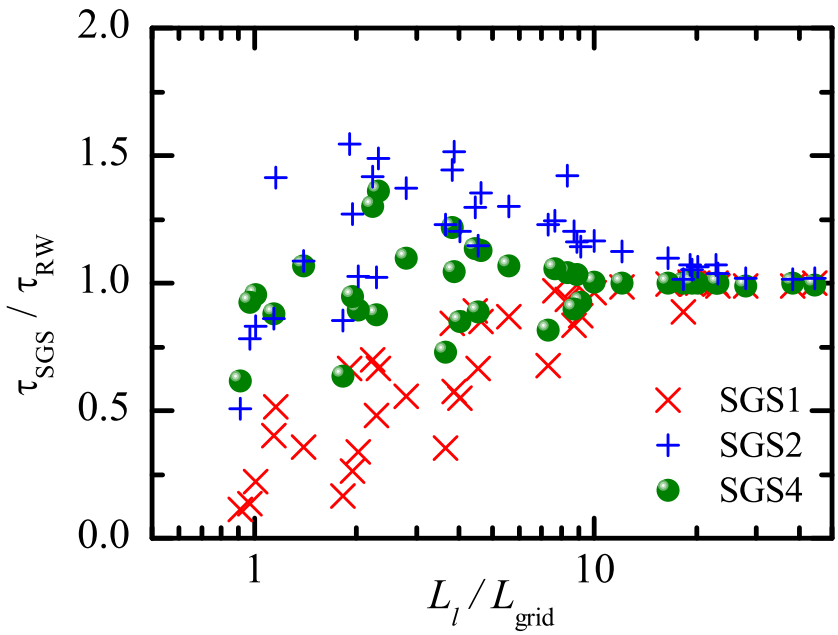

Fig. 4.8. Comparison of the three types of SGS models.

4.4.4 Computation time

The computation time required to obtain the convergent solutions with the SGS4 is shown in Fig. 4.9. All computation times are measured when using a single core of Xeon W3690 processor. It clearly shows the effectiveness of the SGS model. As discussed in Fig. 4.7, the typical structure of porous materials needs to be resoluted with more than 15 grids when SGS models are not applied. On the other hand, the required number of grids can be reduced to about 10 if the SGS4 is applied as shown in Fig. 4.8. This makes it possible to reduce the computation time by almost one-tenth. If a coarser grid can be used in the electrode simulation without losing accuracy, the electrode simulation can be combined with a larger-scale analysis, or more accuracy can be expected in the simulation with limited computational resources.

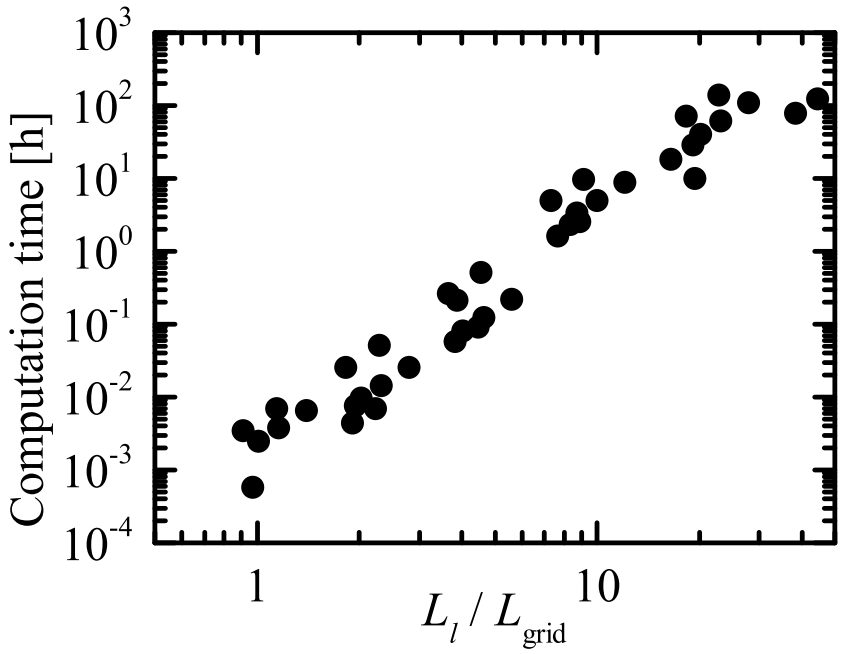

Fig. 4.9. Computation time required to obtain a convergent solution when the SGS4 is applied.

4.5 Conclusions

Sub-grid-scale model used for the three-dimensional numerical analysis in the SOFC electrodes is developed. The main function of the SGS model is to maintain the quality of the voxel-based structural information in a resampled structure used as the calculation grid system by considering a structure with a characteristic scale that is smaller than the grid size. Improvement of the simulation accuracy and reduction of the computation load can be expected with the SGS models. In the present chapter, four types of SGS models are investigated to clarify their effect and applicability. They are featured by (1) volume conservation, (2) interfacial connectivity, (3) power law with a constant power index, and (4) power law with an adaptive power index, respectively. The validity of the proposed SGS models are investigated through the diffusion simulation. Main conclusions drawn in the present chapter can be stated as follows:

1. The volume conservation (SGS1) is not enough to represent the structural information in the grids. In order to maintain the accuracy of the numerical simulation, characteristic scale of porous materials needs to be resoluted with more than 15 grids. However, it may result in increasing computation load.

2. Use of the surface information on the grid interface (SGS2) or the constant power low (SGS3) has a positive contribution to maintain the structural information in the grids by evaluating the local tortuosity factor. However, their availabilities are not assured in wide range of grid sizes, resulting in underestimation or overestimation of the structural complexity.

3. By using the ratio between the grid size and the characteristic scale of the porous structure for an adoptive power index (SGS4), the structural complexity in the grids is successfully evaluated in wide range of grid sizes. The SGS4 exerts its effect preferably in accordance with the grid size.

4. The computation time is significantly reduced by applying the SGS4 with keeping the simulation accuracy. An accurate and effective SGS model can promote a flexible application of the numerical technique to the analysis in porous materials.

Bibliography

[1] D. Simwonis, F. Tietz, D. Stöver, Nickel Coarsening in Annealed Ni/8YSZ Anode Substrates for Solid Oxide Fuel Cells, *Solid State Ionics* **132** (2000) 241–251.

[2] S.P. Jiang, Sintering Behavior of $Ni/Y_2O_3 - ZrO_2$ Cermet Electrodes of Solid Oxide Fuel Cells, *Journal of Materials Science* **38** (2003) 3775–3782.

[3] A. Hagen, R. Barfod, P.V. Hendriksen, Y.L. Liu, S. Ramousse, Degradation of Anode Supported SOFCs as a Function of Temperature and Current Load, *Journal of The Electrochemical Society* **153**(3) (2006) A1165–A1171.

[4] A. Faes, A. Hessler-Wyser, D. Presvytes, C.G. Vayenas, J. Van herle, Nickel-Zirconia Anode Degradation and Triple Phase Boundary Quantification from Microstructural Analysis, *Fuel Cells* **6** (2009) 841–851.

[5] L. Holzer, B. Iwanschitz, Th. Hocker, B. Münch, M. Prestat, D. Wiedenmann, U. Vogt, P. Holtappels, J. Sfeir, A. Mai, Th. Graule, Microstructure Degradation of Cermet Anodes for Solid Oxide Fuel Cells: Quantification of Nickel Grain Growth in Dry and in Humid Atmospheres, *Journal of Power Sources* **196** (2011) 1279–1294.

[6] N. Shikazono, D. Kanno, K. Matsuzaki, H. Teshima, S. Sumino, N. Kasagi, Numerical Assessment of SOFC Anode Polarization Based on Three-Dimensional Model Microstructure Reconstructed from FIB-SEM Images, *Journal of The Electrochemical Society* **157**(5) (2010) A665-672.

[7] K. Matsuzaki, N. Shikazono, N. Kasagi, Three-Dimensional Numerical Analysis of Mixed Ionic and Electronic Conducting Cathode Reconstructed by Focused Ion Beam Scanning Electron Microscope, *Journal of Power Sources* **196** (2011) 3073–3082.

[8] D. Kanno, N. Shikazono, N. Takagi, K. Matsuzaki, N. Kasagi, Evaluation of SOFC Anode Polarization Simulation Using Three-Dimensional Microstructures Reconstructed by FIB Tomography, *Electrochimica Acta* **56** (2011) 4015–4021.

[9] P.R. Shearing, Q. Cai, J.I. Golbert, V. Yufit, C.S. Adjiman, N.P. Brandon, Microstructural Analysis of a Solid Oxide Fuel Cell Anode Using Focused Ion Beam Techniques

Coupled with Electrochemical Simulation, *Journal of Power Sources* **195** (2010) 4804–4810.

[10] Q. Cai, C.S. Adjiman, N.P. Brandon, Investigation of the Active Thickness of Solid Oxide Fuel Cell Electrodes Using a 3D Microstructure Model, *Electrochimica Acta* **56** (2011) 10809–10819.

[11] B. Ruger, J. Joosa, A. Weber, T. Carraro, E. Ivers-Tiffée, 3D Electrode Microstructure Reconstruction and Modelling, *ECS Transactions* **25**(2) (2009) 1211–1220.

[12] U. Doraswami, P. Shearing, N. Droushiotis, K. Li, N.P. Brandon, G.H. Kelsall, Modelling the Effects of Measured Anode Triple-Phase Boundary Densities on the Performance of Micro-Tubular Hollow Fiber SOFCs, *Solid State Ionics* **192** (2011) 494–500.

[13] J. Joos, T. Carraro, A. Weber, E. Ivers-Tiffée, Reconstruction of Porous Electrodes by FIB/SEM for Detailed Microstructure Modeling, *Journal of Power Sources* **196** (2011) 7302–7307.

[14] J. Mizusaki, H. Tagawa, T. Saito, T. Yamamura, K. Kamitani, K. Hirano, S. Ehara, T. Takagi, T. Hikita, M. Ippommatsu, S. Nakagawa, K. Hashimoto, Kinetic Studies of the Reaction at the Nickel Pattern Electrode on YSZ in $H_2 - H_2O$ Atmospheres, *Solid State Ionics* **70/71** (1994) 52-58.

[15] B. de Boer, Ph.D. Thesis, SOFC Anode - Hydrogen Oxidation at Porous Nickel and Nickel/Yttria-Stabilized Zirconia Cermet Electrodes, *University of Twente*, Netherlands 1998.

[16] A. Bieberle, L.P. Meier, L.J. Gauckler, The Electrochemistry of Ni Pattern Anodes Used as Solid Oxide Fuel Cell Model Electrodes, *Journal of The Electrochemical Society* **148**(6) (2001) A646-A656.

[17] A. Utz, H. Stormer, A. Leonide, A. Weber, E.Ivers-Tiffee, Degradation and Relaxation Effects of Ni Patterned Anodes in H_2-H_2O Atmosphere, *Journal of The Electrochemical Society* **157**(6) (2010) B920-B930.

[18] R. Radhakrishnan, A.V. Virkar, S.C. Singhal, Estimation of Charge-Transfer Resistivity of $La_{0.8}Sr_{0.2}MnO_3$ Cathode on $Y_{0.16}Zr_{0.84}O_2$ Electrode Using Patterned Electrodes, *Journal of The Electrochemical Society* **152**(1) (2005) A210-A218.

[19] T. Kawada, N. Sakai, H. Yokokawa, M. Dokiya, Characteristics of Slurry-Coated Nickel Zirconia Cermet Anodes for Solid Oxide Fuel Cells, *Journal of The Electrochemical Society* **137**(10) (1990) 3042-3047.

[20] Y. Suzue, N. Shikazono, N. Kasagi, Micro Modeling of Solid Oxide Fuel Cell Anode Based on Stochastic Reconstruction, *Journal of Power Sources* **184** (2008) 52-59.

[21] H. Zhu, R.J. Kee, V.M. Janardhanan, O. Deutschmann, D.G. Goodwin, Modeling Elementary Heterogeneous Chemistry and Electrochemistry in Solid-Oxide Fuel Cells, *Journal of The Electrochemical Society* **152**(12) (2005) A2427-A2440.

[22] W.G. Bessler, M. Volger, H. Stormer, D. Gerthsen, A. Utz, A. Weber, E. Ivers-Tiffee, Model Anodes and Anode Models for Understanding the Mechanism of Hydrogen Oxidation in Solid Oxide Fuel Cells, *Physical Chemistry Chemical Physics* **12** (2010) 13888-13903.

[23] P. Costamagna, P. Costa, V. Antonucci, Micro-Modeling of Solid Oxide Fuel Cell Electrodes, *Electrochimica Acta* **43** (1998) 375-394.

[24] J.H. Nam, D.H. Jeon, A Comprehensive Micro-Scale Model for Transport And Reaction in Intermediate Temperature Solid Oxide Fuel Cells, *Electrochimica Acta* **51** (2006) 3446-3360.

[25] A, Abbaspour, J.L. Luo, N. Nandakumar, Three-Dimensional Random Resistor-Network Model for Solid Oxide Fuel Cell Composite Electrodes, *Electrochimica Acta* **55** (2010) 3944-3950.

Chapter 5

Effect of Composition of Ni-YSZ Anode on Distribution of Three-Phase Boundary and Power Generation Performance

5.1 Introduction

For the conventional Ni-YSZ cermet anode, composition ratio between the Ni and YSZ phases is the primary control parameter that determines the fundamental microstructural characteristics of the anodes [1–3]. Therefore, it is essentially important to clarify the effect of the ratio on other microstructural parameters and on the overall anode performance. The anode performance mainly depends on the two aspects of the porous structure: the TPB density and the phase connectivity. The electrochemical reaction inside the Ni-YSZ anode is considered to occur around the TPB; therefore, the anodes are expected to contain as much TPB as possible to provide abundant reaction site. At the same time, for the sufficient transport of chemical species to and from the TPB, contiguous pathways of the Ni, YSZ, and pore phases must be secured; the lack of any one of these pathways results in making the TPB inactive.

Reaction region is also a major subject of interest in optimizing the electrode microstructure [4–6]. In the case of anode supported SOFC cells, the anodes often consist of two layers with different microstructure: the function layer and the support layer. The function layer is fabricated just on the electrolyte and made with relatively small particles to have larger

TPB density. On the other hand, the support layer has larger porosity for sufficient gas diffusion through the layer. Generally, the support layer occupies most part of the anode and the thickness of the function layer is at most several tens of microns. This is because the reaction in the anode is considered to occur in the vicinity of the anode-electrolyte interface, which is sometimes called active reaction region or active thickness. However, the active thickness significantly changes depending on the anode microstructure as well as operating conditions.

In the present chapter, the electrochemical characteristics of the Ni-YSZ cermet anodes with three different compositions, Ni:YSZ = 70:30, 50:50, and 30:70 vol.%, will be experimentally evaluated. Next, the three-dimensional microstructure of the porous anodes will be observed with the FIB-SEM and quantitatively analyzed. The phase connectivity of the porous components and the distribution of the effective TPB will be investigated as essential parameters to explain the relationships between the anode microstructure and the electrochemical performance. Finally, a numerical simulation of the anode overpotential using the obtained three-dimensional microstructure will be conducted and the internal states of the anodes will be investigated, such as the distribution of the charge-transfer current.

5.2 Experiment

The electrochemical characteristics of the Ni-YSZ anodes are experimentally evaluated. The Ni:YSZ = 70:30, 50:50, and 30:70 presented in Chapter 2 are used. The three-dimensional microstructure of the examined anodes are obtained with the FIB-SEM and various microstructural parameters are quantified. Details of the electrochemical characterization and the three-dimensional observation are also presented in Chapter 2.

5.3 Numerical Model

Numerical simulation of the anode polarization characteristics are carried out with the three-dimensional porous structure obtained with the FIB-SEM. The simulation is based on the finite volume method (FVM) with a structured hexahedral grid system.

5.3.1 Calculation domain

Schematic picture of the calculation domain is shown in Fig. 5.1. The whole anode structure obtained with the FIB-SEM is mirror-symmetrically extended twice in the X direction to equivalently attain the real anode thickness. The conservation of electrons in the Ni phase, oxide ions in the YSZ phase, and gas species in the pore phase are considered and linked by the electrochemical oxidation of hydrogen at the TPB. Temperature and total gas pressure are assumed to be constant and uniform over the whole anode region.

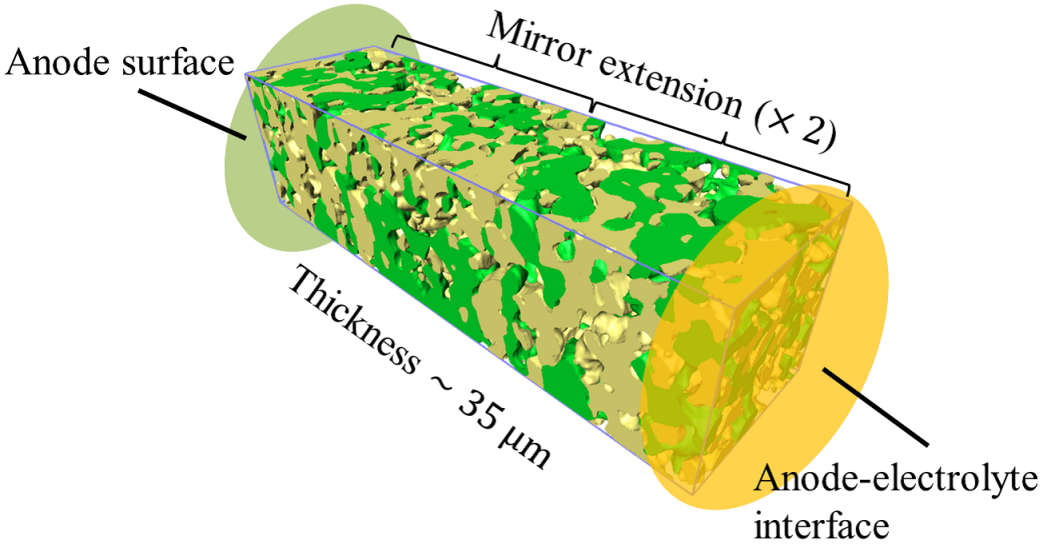

Fig. 5.1. Schematic picture of the calculation domain.

5.3.2 Governing equations

Governing equations presented in Chapter 2 are used in this chapter. For the evaluation of the effective transport coefficient in each calculation grid, the SGS model proposed in Chapter 4 is used. The grid size used in this study is around 150 $\sim$ 200 nm, which indicates the characteristic scale of the porous anodes is resoluted with more than 7 grids.

5.3.3 Boundary conditions

Boundary conditions set on the anode surface and the anode-electrolyte interface are shown in Table 5.1. Gas compositions are constant on the anode surface to represent the supplied fuel composition. In order to determine the anode overpotential, the electric potential in the Ni phase at the anode surface and that in the YSZ phase at the anode-electrolyte interface are properly set. Boundary conditions on the other surfaces (X-Y and X-Z surfaces) are the no-flux condition for all variables.

Table 5.1. Boundary conditions.

Variables	Surface ($X = 0$)	Interface ($X = L$)
H_2 partial pressure	$P_{H_2}(0) = P_{H_2}^{bulk}$	$\frac{dP_{H_2}}{dx}(L) = 0$
H_2O partial pressure	$P_{H_2O}(0) = P_{H_2O}^{bulk}$	$\frac{dP_{H_2O}}{dx}(L) = 0$
Electric potential in Ni	$\phi_{el}(0) = \eta_t$	$\frac{d\phi_{el}}{dx}(L) = 0$
Electric potential in YSZ	$\frac{d\phi_{io}}{dx}(0) = 0$	$\phi_{io}(L) = 0$

5.3.4 Calculation conditions

Calculation conditions are shown in Table 5.2. Unlike the case of the one-dimensional simulation with the microstructural parameters, the structural information is represented by the grid system itself with the aid of the SGS models; therefore, there is no need to apply the quantified microstructural parameters to the grids.

Table 5.2. Default calculation conditions.

Parameter	Symbol	Value	Unit
Total Pressure	P_t^{bulk}	1.013×10^5	[Pa]
Temperature	T	1000	[°C]
H_2 partial pressure	$P_{H_2}^{bulk}$	$0.97 \times P_t^{bulk}$	[Pa]
H_2O partial pressure	$P_{H_2O}^{bulk}$	$0.03 \times P_t^{bulk}$	[Pa]

5.4 Results and Discussion

5.4.1 Anode performance

Figure 5.2 shows the electrochemical characteristics of the anodes examined in this study. Fig. 5.2(c) shows the overpotential characteristics that are obtained by substituting the ohmic loss from the total anode overpotential measured as the voltage drop from the open-circuit voltage in Fig. 5.2(a). The ohmic resistances are obtained from the high-frequency intercept of the impedance characteristics in Fig. 5.2(b). This substituting process is aiming to eliminate the voltage loss attributed to the ionic conduction through the YSZ electrolyte. However, as will be discussed later, the overpotential of the Ni:YSZ = 30:70 anode includes non-negligible ohmic resistance inside the anode. Therefore, the ohmic resistance of the Ni:YSZ = 50:50 anode is used instead.

Fig. 5.2 clearly shows lower performance of the Ni:YSZ = 30:70 anode compared with the others. This is mainly attributed to the high ohmic resistance of the anode. On the other hand, there is only a small difference between the characteristics of the Ni:YSZ = 50:50 anode and that of the Ni:YSZ = 70:30 anode even though they are expected to have different porous microstructure. The slight difference can be attributed to the difference of the polarization resistance, which is estimated from the size of the impedance arc.

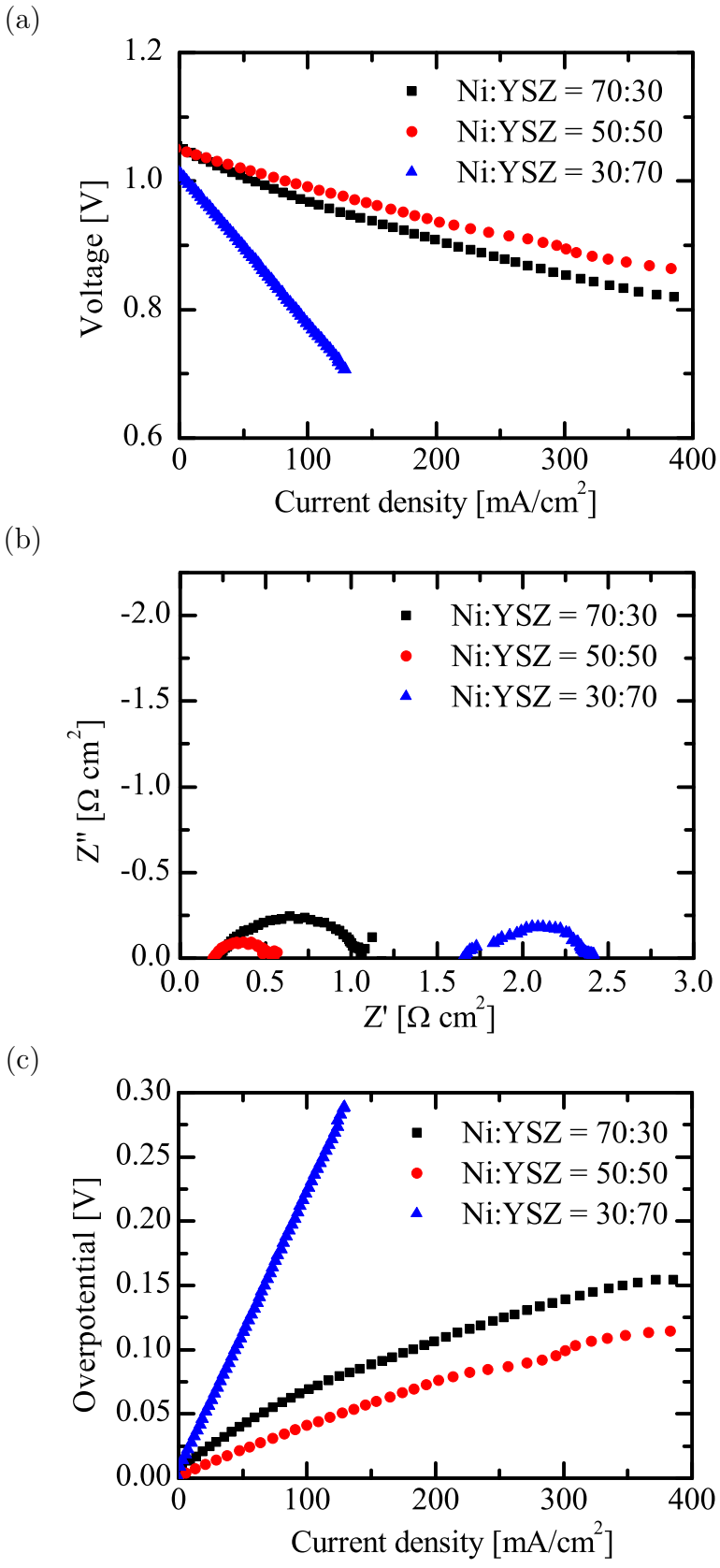

Fig. 5.2. Anode electrochemical performance (Anode-Reference). (a) I-V characteristics. (b) Impedance characteristics. (c) Overpotential characteristics. (1000 °C, $H_2 : H_2O = 97:3$)

5.4.2 Microstructural parameters

Microstructural parameters of the anode structures have been already shown in Chapter 2. Here, some of the parameters related to the discussion in this chapter are briefly reproduced.

Table 5.3 shows the sample sizes and voxel sizes of the anode samples. The region larger than 10 μm^3 is successfully obtained for each anode sample. Table 5.4 shows the volume fraction of the anode samples. The ratios of the Ni and YSZ volume fractions, which are Ni:YSZ = 31.8:68.2, 53.5:46.5, and 69.1:30.9, respectively, are close to the intended values, which indicates the observed region is large enough to be representative of the whole anode structure. Table 5.5 shows the percolation probabilities of the anodes. The Ni:YSZ = 30:70 and 70:30 anodes lack in the percolation of the Ni and YSZ phase, respectively, which is because of the low volume fraction of the phases.

Table 5.3. Sample sizes and voxel sizes.

	Sample size [μm]			Voxel size [nm]		
Sample	X	Y	Z	X	Y	Z
Ni:YSZ = 70:30	18.0	13.2	10.5	30.0	30.0	52.3
Ni:YSZ = 50:50	18.1	9.72	9.97	34.7	34.7	62.3
Ni:YSZ = 30:70	18.8	11.6	10.1	36.2	36.2	42.2

Table 5.4. Volume fractions [%].

Sample	Ni	YSZ	Pore	Ni:YSZ
Ni:YSZ = 70:30	42.3	18.9	38.8	69.1:30.9
Ni:YSZ = 50:50	34.2	29.7	36.1	53.5:46.5
Ni:YSZ = 30:70	23.6	50.6	25.8	31.8:68.2

Table 5.5. Percolation probability.

	Ni			YSZ			Pore		
Sample	X	Y	Z	X	Y	Z	X	Y	Z
Ni:YSZ = 70:30	0.988	0.988	0.988	0.000	0.681	0.681	0.997	0.997	0.997
Ni:YSZ = 50:50	0.987	0.987	0.987	0.961	0.961	0.961	0.886	0.996	0.996
Ni:YSZ = 30:70	0.000	0.155	0.000	1.000	1.000	1.000	1.000	0.986	0.986

TPB density of the anodes are shown in the center column of Table 5.6. Although slight difference is observed, it can not explain the significant difference in the anode performance. The TPB density in the Ni:YSZ = 30:70 anode is slightly lower than that of the Ni:YSZ =

Table 5.6. TPB density. [μm/μm^3]

Sample	Total	Effective
Ni:YSZ = 70:30	1.77	0.700
Ni:YSZ = 50:50	2.00	1.53
Ni:YSZ = 30:70	1.81	0.610

50:50 anode; however, the difference is too small to make the overpotential more than double. Moreover, it is even larger than that of the Ni:YSZ = 70:30 anode, which is inconsistent with the order of the overpotentials. Therefore, in order to carry on the discussion, the "effective" TPB is extracted from the total TPB. It is assumed that there is a current collector on the $X = 0$ plane and an anode-electrolyte interface on the opposite side, and the TPB that is connected to the current collector with the Ni phase and also to the interface with the YSZ phase is extracted. The Ni or YSZ phases connected with only sidewalls (X-Y and X-Z planes) are regarded as unconnected in this study. Results are shown in the right column of Table 5.6. In the Ni:YSZ = 70:30 and Ni:YSZ = 30:70 anodes, considerable part of the TPB are judged as inactive since the connectivity of the Ni or YSZ phase is limited. However, it still can not explain why the anode performance of only the Ni:YSZ = 30:70 anode is worse than the other samples.

For the further investigation, the distribution of the effective TPB is investigated in the observed region, which is shown in Fig. 5.3. Also for the quantitative analysis, Fig. 5.4 shows the distribution of the volume fractions and the effective TPB density in the thickness direction of the anode. The electrochemical reaction in the Ni-YSZ anode is reported to be active in the vicinity of the anode-electrolyte interface because the YSZ phase has higher transport resistance for oxide ion transport compared with the other resistances associated with the electron and gaseous transport. However, this is only valid when the transport pathways of each phase to and from the TPB is secured. In the case of the Ni:YSZ = 30:70 anode, the Ni phase lacks the connectivity because of its low volume fraction. Therefore, the transport pathways of the Ni phase from the current collector to the vicinity of the anode-electrolyte interface is hardly created, which shifts the effective TPB far from the interface. In such a case, the ionic transport pathways through the YSZ phase needs to become longer, which causes high ohmic loss. This is the reason why the overpotential of the Ni:YSZ = 30:70 anode is remarkably higher than the others. On the other hand, the Ni:YSZ = 70:30

anode has sufficient effective TPB near the interface with the amount that is comparable to that of the Ni:YSZ = 50:50 anode. This is the reason why the performance of the Ni:YSZ = 70:30 anode is similar to that of the Ni:YSZ = 50:50 anode.

From the above discussion, it is concluded that the amount of the total TPB is inappropriate for the correlative analysis between the electrode performance and the microstructure; instead, the amount and distribution of the effective TPB is significantly important to explain the anode performance; sufficient amount of the effective TPB should be distributed near the anode-electrolyte interface to provide reaction sites for the electrochemical reaction.

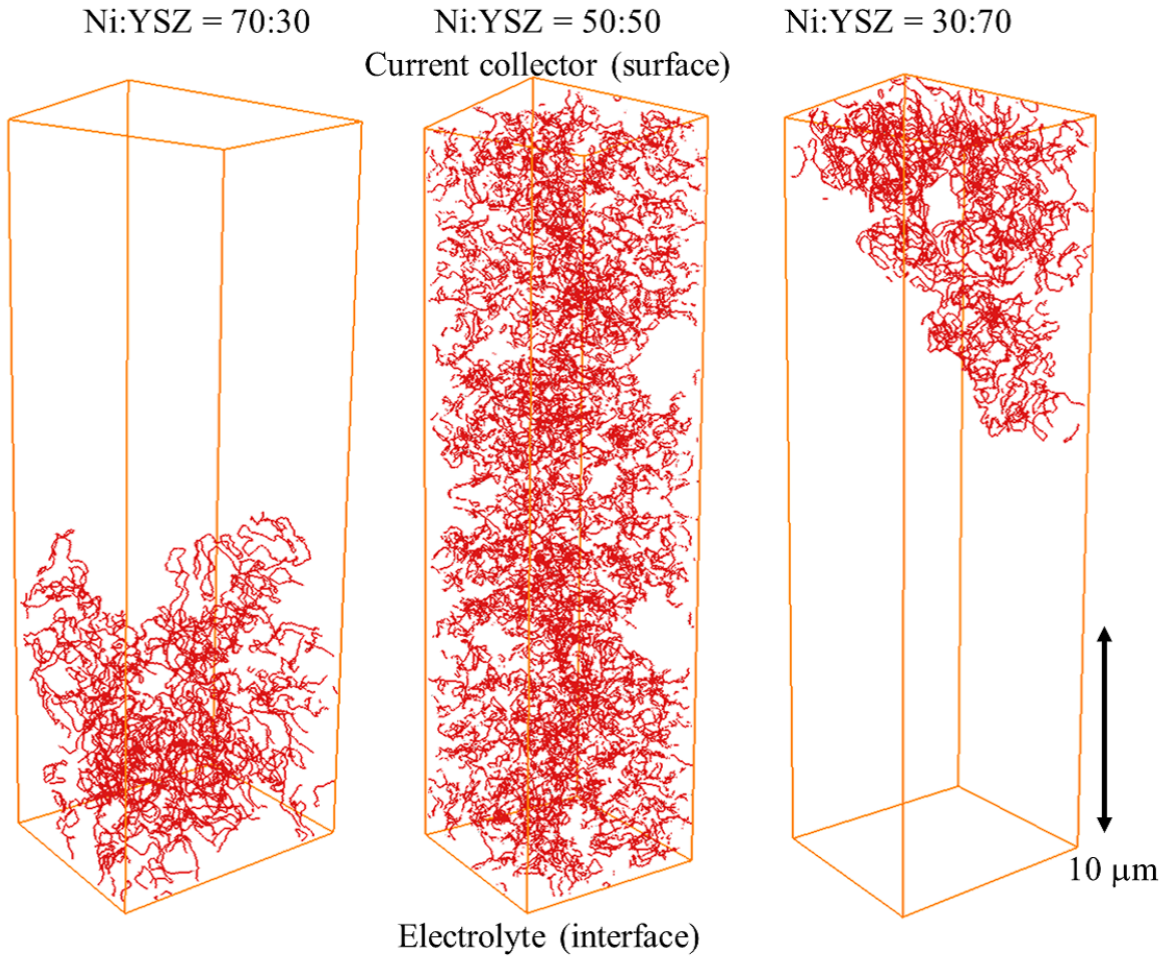

Fig. 5.3. Distribution of the effective three-phase boundary.

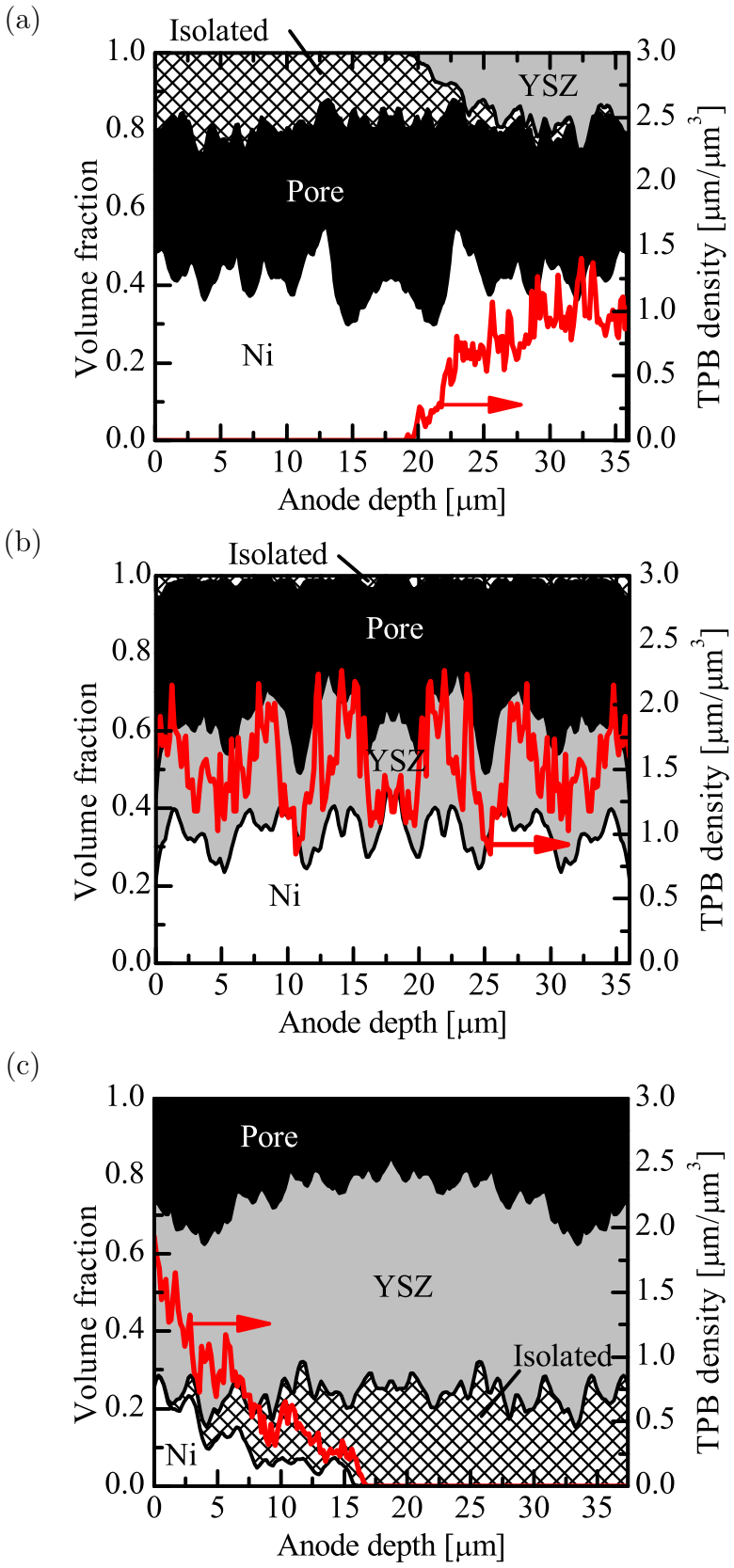

Fig. 5.4. Distribution of the volume fractions and the effective TPB density in the thickness direction of the anode. Ni:YSZ = (a) 70:30, (b) 50:50, and (c) 30:70.

5.4.3 Numerical simulation

Figure 5.5 shows the comparison of the anode overpotential between the numerical simulation and the experiment. The trend of the overpotential obtained in the experiment is qualitatively reproduced by the simulation; the overpotential of the Ni:YSZ = 30:70 anode is about twice as large as that of the Ni:YSZ = 50:50 anode, and the Ni:YSZ = 70:30 anode shows similar but slightly higher overpotential than that of the Ni:YSZ = 50:50 anode. It can be concluded that the numerical model used in this study has enough sensitivity to the structural difference of the porous structure. The discrepancy between the numerical simulation and the experiment can be attributed to the electrochemical reaction kinetics model described by eqs. (3.19)–(3.26) shown in Chapter 3. More sophisticated electrochemical model such as those considering elementary chemical reactions around the TPB is required to improve the simulation model.

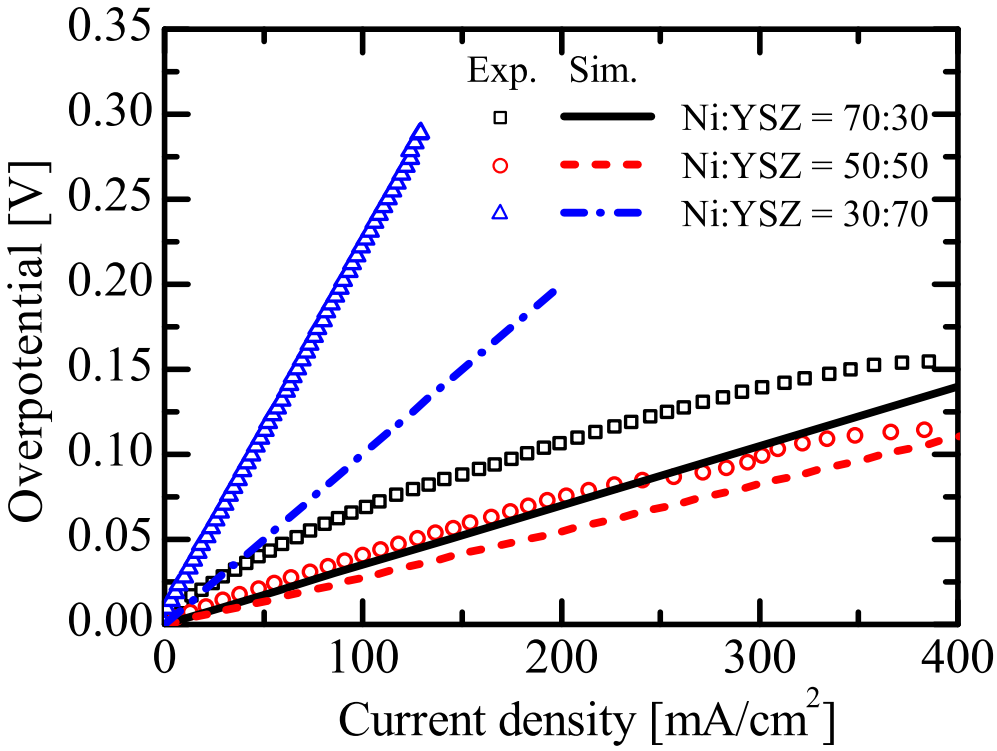

Fig. 5.5. Comparison of the anode overpotential. T = 1000 °C, $H_2 : H_2O$ = 97:3.

To analyze the active reaction region in the Ni-YSZ anodes, the distribution of the effective TPB and the charge-transfer current density are investigated in the thickness direction of the anode (Fig. 5.6). In the case of the Ni:YSZ = 30:70 anode, the reaction region locates more than 20 μm away from the anode-electrolyte interface because of the lack of the effective TPB in the region. On the other hand, in the case of the Ni:YSZ = 50:50 and 70:30 anodes, there is sufficient amount of the effective TPB around the interface so that the peak charge-transfer current is located just on the interface. If the thickness of the active reaction region is defined as the region from the anode-electrolyte interface where 90% of the total electrochemical reaction takes place, the thicknesses are 14.2, 15.6, and 33.8 μm for Ni:YSZ = 70:30, 50:50, and 30:70 anodes, respectively.

Generally, larger volume fraction in a porous structure is preferable for sufficient transport through the phase. However, it is of course impossible to achieve high volume fraction in all phases of porous components. If the volume fraction of the Ni phase is larger, the YSZ phase becomes more complex and is likely to have larger isolated part. On the other hand, if the volume fraction of the YSZ is larger, connectivity of the Ni phase becomes poorer and the effective TPB cannot exist in the vicinity of the anode-electrolyte interface as discussed above. Considering that the oxide-ion conductivity of the YSZ phase is much lower than the electron conductivity of the Ni phase, the YSZ volume fraction should be larger to reduce the ohmic resistance in the phase. At the same time, the transport pathways of the electrons should be secured from the current collector to the vicinity of the anode-electrolyte interface. This should be the primary concern for optimizing the anode microstructure. As the next step, in order to maximize the amount of the effective TPB density, the volume fractions and particle sizes of the two phases should be modified particularly in the function layer in anode supported cells. The appropriate thickness of the function layer is found to be about 15 μm in the condition of $H_2 : H_2O = 97:3$ at 1000 °C. However, since the porous structure is reported to change over long-time operation, the microstructure should be fabricated so that it can minimize the structure change along the time. Further optimizing policy for achieving the anode with higher performance and longer durability should be discussed along with the detailed understanding of the degradation mechanism.

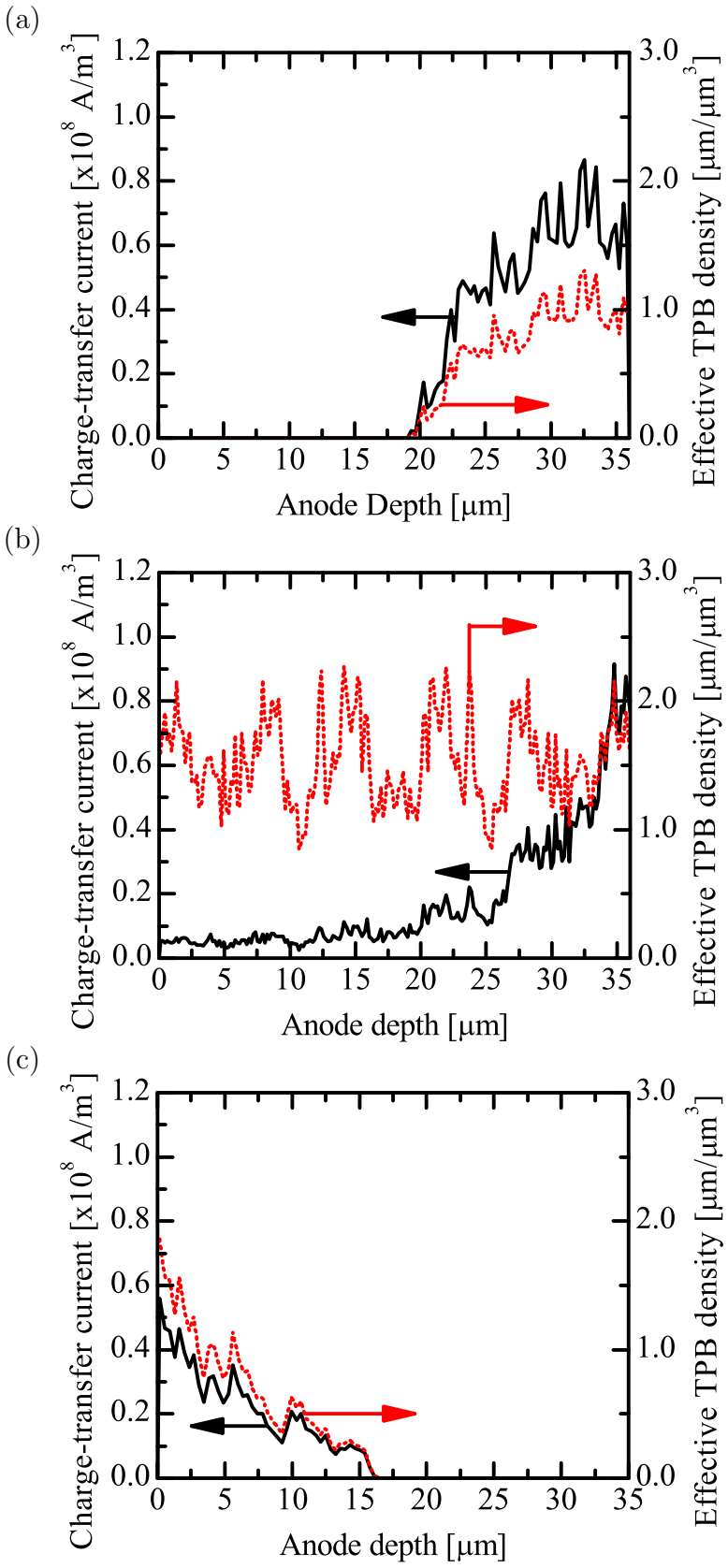

Fig. 5.6. One-dimensional distribution of the charge-transfer current and the effective TPB density. Ni:YSZ = (a) 70:30, (b) 50:50, and (c) 30:70.

5.5 Conclusions

Ni-YSZ composite anodes of SOFCs with three different compositions are examined and compared through the electrochemical measurement, microstructural analysis, and numerical simulation. Porous microstructure of the examined anodes is directly observed with the FIB-SEM and used for the three-dimensional simulation with the aid of the SGS models proposed in Chapter 4. Main conclusions drawn in the present chapter can be stated as follows:

1. The Ni:YSZ = 30:70 anode shows significantly lower performance than the other anodes because of the higher ohmic resistance. This is attributed to the longer conduction pathways of the oxide ions through the anode. The low Ni volume contents inhibits the effective pathways for the electrons from the anode surface (current collector) to the vicinity of the anode-electrolyte interface, as a result, the oxide ions are required to be transported far away from the interface for the electrochemical reaction.

2. The Ni:YSZ = 70:30 anode shows similar performance to that of the Ni:YSZ = 50:50 anode even though they are expected to have different porous structure. This is because the sufficient amount of the effective TPB is distributed around the anode-electrolyte interface in both anodes. Although the connectivity of the YSZ phase in the Ni:YSZ = 70:30 anode is poor, it is enough to secure the oxide-ion transport from the electrolyte to the TPB located close to the anode-electrolyte interface.

3. The amount and distribution of the effective TPB is essentially important to explain the anode performance, instead of the commonly-used total TPB density. This addresses the importance of obtaining the three-dimensional structure in analyzing the relationships between the electrode microstructure and the performance because the connectivity of the porous components, which are necessary for extracting the effective TPB, are only available through the three-dimensional analysis.

4. The three-dimensional numerical simulation of the anode overpotential using the obtained porous structure qualitatively reproduces the experimental results. Since the precision of the transport analysis in the porous structure is fairly assured by using the SGS model, the discrepancy between the numerical prediction and the experimental

results can be attributed to the electrochemical reaction model adopted in this study. Further improvement is required to achieve more reliable simulation model.

5. Combined with the distribution of the charge-transfer current density and the effective TPB, the simple optimizing policy for the Ni-YSZ anode is proposed.

Bibliography

[1] J.H. Lee, H. Moon, H.W. Lee, J. Kim, J.D. Kim, K.H. Yoon, Quantitative Analysis of Microstructure and its Related Electrical Property of SOFC Anode, Ni-YSZ Cermet, *Solid State Ionics* **148** (2002) 15–26.

[2] J.R. Wilson, J.S. Cronin, S.A. Barnett, Linking the Microstructure, Performance and Durability of Ni-Yttria-Stabilized Zirconia Solid Oxide Fuel Cell Anodes Using Three-Dimensional Focused Ion Beam-Scanning Electron Microscopy Imaging, *Scripta Materialia* **65** (2011) 67–72.

[3] N. Vivet, S. Chupin, E. Estrade, A. Richard, S. Bonnamy, D. Rochais, E. Bruneton, Effect of Ni Content in SOFC Ni-YSZ Cermets: A Three-Dimensional Study by FIB-SEM Tomography, *Journal of Power Sources* **196** (2011) 9989–9997.

[4] M. Brown, S. Primdahl, M. Mogensen, Structure/Performance Relations for Ni/Yttria-Stabilized Zirconia Anodes for Solid Oxide Fuel Cells, *Journal of The Electrochemical Society* **147**(2) (2000) 475–485.

[5] N. Shikazono, D. Kanno, K. Matsuzaki, H. Teshima, S. Sumino, N. Kasagi, Numerical Assessment of SOFC Anode Polarization Based on Three-Dimensional Model Microstructure Reconstructed from FIB-SEM Images, *Journal of The Electrochemical Society* **157**(5) (2010) B665–B672.

[6] Q. Cai, C.S. Adjiman, N.P. Brandon, Investigation of the Active Thickness of Solid Oxide Fuel Cell Electrodes Using a 3D Microstructure Model, *Electrochimica Acta* **56** (2011) 10809–10819.

Chapter 6

Prediction of Active Thickness in SOFC Anode with Characteristic Length of Oxide-Ion Conduction

6.1 Introduction

Among the various microstructural parameters, the TPB density is one of the most important parameters that directly affects the electrode performance. The more TPB is distributed in the electrodes, the better performance can be expected. However, it has been widely accepted that the distribution of the electrochemical reaction in porous electrodes is non-uniform and it mainly occurs in the vicinity of the electrode-electrolyte interface. In other words, only limited segment of the TPB is active for the electrochemical reaction. This is because the oxide-ion conductivity in the electrode is usually several orders smaller than the electron conductivity and gas diffusivity. The electrochemically active region in the electrodes is often called active reaction region or active thickness.

When the electrode thickness is thinner than the active thickness, the electrode performance can be improved by increasing the electrode thickness. On the other hand, if the electrode thickness is much thicker than the active thickness, the electrode performance may decrease because of the increase of the mass transport resistance in the pore phase. Therefore, the precise information about the active thickness is necessary in designing electrodes with optimum thickness. Although many researches have been devoted to investigate the active thickness in SOFC electrodes. the values reported in the literatures have significant variation. Table 6.1 summarizes the reported values.

In experimental approaches, many electrodes with different thicknesses were fabricated and their electrochemical performance was characterized by the current-voltage measurement and the electrochemical impedance spectroscopy (EIS). As increasing the electrode thickness, electrode performance generally improves when the electrode is relatively thin, then it reaches constant. The thickness at which the performance reaches the plateau is considered as the active thickness. Juhl et al. [1] examined LSM/YSZ cathode fabricated from powders with around 1 μm in size. The active thickness was evaluated from the area specific resistance of the cathode and was determined around 4–10 μm. It became significantly thinner as the temperature was increased. Primdahl et al. [2] examined a Ni-YSZ anode fabricated from powders with around 0.4 μm size. The active thickness was evaluated from the area specific resistance and was no more than 20 μm at 1000 °C. However, measurement in thinner electrode (less than 10 μm) could not be conducted because of the difficulty in the current collection. Successive investigation was conducted by Brown et al. [3] with the same experimental configuration, and the active thickness was determined as about 10 μm at 1000 °C. They mentioned the thickness was related to the conductivity of the YSZ network. Kong et al. [4] examined with a multilayer Ni-YSZ anode in which the particle sizes were 0.53 and 1.42 μm for NiO and YSZ, respectively. The active thickness obtained from the current-voltage characteristics was about 40–50 μm. Moon et al. [5] fabricated a Ni-YSZ anode with a function layer of various thicknesses and found the optimal thickness of the layer to be 20 μm at 600–700 °C. The optimal thickness for the function layer can be directly linked with the active thickness. Chen et al. [6] also attempted to optimize the thickness of the function layer of a Ni-YSZ anode and found that the anode with a function layer with 5 μm thickness exhibited the highest performance at 800 °C. The active thickness obtained through the experimental approaches widely varies from 5 to 50 μm, which may be attributed to the difference in the microstructure of the examined electrodes and in the operating conditions such as temperature.

There are also many numerical approaches to investigate the active thickness. Sunde et al. [7] applied random-resistor network model to represent the complex conduction pathways in the porous electrode, and investigated the active thickness. Varying the electrode thickness from 1 to 100 μm, the inverse of the area-specific polarization resistance was obtained, from which the active thickness was determined as 30–40 μm. Chan et al. [8] conducted one-

dimensional numerical simulation for the Ni-YSZ anode with the microstructure that was considered homogeneous and represented by effective parameters such as volume fractions and tortuosity factors. These values were based on the random-spherical packing model. The active thickness in their study was 50, 100, and 160 μm for particle size of 0.2, 0.4, and 0.5 μm, respectively, at 1000 °C. They suggested that the thicker anode was required for the anode with coarser structure to provide sufficient reaction site. Yuan et al. [9] examined the LSCF/SDC cathode in anode-supported cell. The electrode structure was homogenized and represented by the effective conductivity and diffusivity, which were evaluated also with the random-spherical packing model. The active thickness was about 20 μm according to the distribution of the charge-transfer current. The cell temperature was 500 °C, which was relatively lower than those in other researches. Cai et al. [10] applied the volume of fluid (VOF) method to the Ni-YSZ anode with the structure that was made with three-dimensional Monte Carlo packing of spherical particles. The active thickness was about 5–15 μm. They also found that the active thickness was a function of the overpotential and the particle size. These numerical approaches mentioned above more or less depends on the structure models; therefore, the transport properties and electrochemical reaction rate may be different from those of real electrodes. This can be the reason why many different values of the active thickness were reported.

Recently the FIB-SEM technique is used to directly observe the three-dimensional microstructure of the porous electrode, which provides us the detailed information of the complex porous configurations. The numerical techniques using the real three-dimensional structure have been also developed so that the simulation without porous model is realized. Shikazono et al. [11] applied the Lattice Boltzmann method (LBM) for a Ni-YSZ anode and analyzed the distribution of the charge-transfer current. They found that the active thickness was around 10–15 μm at 1000 °C. Matsuzaki et al. [12] also employed the same approach for the LSCF cathode and found the active thickness was around 10–20 μm at 700–800 °C. The active thickness became thicker if the cell temperature was higher and the oxygen concentration in gas phase was lower.

The approaches based on the three-dimensional structure obtained with the FIB-SEM observation give us more reliable values for the active thickness. However, it is time-consuming and requires high computation load to obtain a convergent solution for the simulation. Al-

though many researches suggest that the active thickness is a function of various operating conditions and the microstructure of the electrodes, it is difficult to conduct a systematic investigation to analyze the effect of various factors on the active thickness.

In Chapter 3, the one-dimensional numerical simulation with the homogenized porous structure of the Ni-YSZ anode is conducted. The anode structure was represented by microstructural parameters that were quantified from the FIB-SEM reconstructed structure. The obtained active thickness was about 10–15 μm, which was close to that obtained from the three-dimensional analysis. Therefore, it can be fairly concluded that the one-dimensional numerical analysis based on the homogenized structure is enough to investigate the active thickness if appropriate microstructural parameters are applied.

In the present chapter, a one-dimensional numerical simulation is conducted to evaluate the active thickness in the Ni-YSZ anode. Effect of the microstructural parameters and the operating conditions is systematically investigated. For the prediction of the active thickness, a parameter is newly introduced by taking the ratio between the effective oxide-ion conductivity and the electrochemical reaction rate.

Table 6.1. Active thickness in the literatures.

		Thickness	Material	Comment	Ref.
Exp.	Juhl et al.	10 μm	LSM/YSZ	700–1000 °C	[1]
	Primdahl et al.	∼20 μm	Ni-YSZ	1000 °C	[2]
	Brown et al.	10 μm	Ni-YSZ	1000 °C	[3]
	Kong et al.	40–50 μm	Ni-YSZ		[4]
	Moon et al.	20 μm	Ni-YSZ	600–700 °C	[5]
	Chen et al.	5 μm	Ni-YSZ	800 °C	[6]
Sim.	Sunde et al.	30–40 μm	Ni-YSZ	Random register	[7]
	Chan et al.	50, 100, 160 μm	Ni-YSZ	1D, Homogenious	[8]
	Yuan et al.	20 μm	LSCF/SDC	2D, Homogenious	[9]
	Cai et al.	5–15 μm	Ni-YSZ	3D, Monte Carlo	[10]
	Shikazono et al.	10–15 μm	Ni-YSZ	3D, FIB-SEM	[11]
	Matsuzaki et al.	10–20 μm	LSCF	3D, FIB-SEM	[12]

6.2 Numerical Model

The one-dimensional numerical model proposed in Chapter 3 is employed in this chapter. Conservations of electrons, oxide ions, and gas species are considered and linked by the electrochemical reaction at the TPB. The microstructural parameters are applied to the calculation grids to evaluate the effective transport coefficients and the electrochemical reaction rate.

6.2.1 Calculation conditions

The calculation conditions used in this chapter are summarized in Table 6.2. These parameters are used as constants unless specified.

Table 6.2. Default calculation conditions.

Parameter	Symbol	Value	Unit
Total pressure	P_t^{bulk}	1.013×10^5	[Pa]
Temperature	T	800, 1000	[°C]
H_2 partial pressure	$P_{\text{H}_2}^{\text{bulk}}$	$P_t^{\text{bulk}} \times 0.97$	[Pa]
H_2O partial pressure	$P_{\text{H}_2\text{O}}^{\text{bulk}}$	$P_t^{\text{bulk}} \times 0.03$	[Pa]
Ni volume fraction	V_{Ni}	0.30	
YSZ volume fraction	V_{YSZ}	0.30	
Pore volume fraction	V_{Pore}	0.40	
Ni tortuosity factor	τ_{Ni}	4.0	
YSZ tortuosity factor	τ_{YSZ}	4.0	
Pore tortuosity factor	τ_{Pore}	2.0	
Pore S-V ratio	$(S/V)_{\text{Pore}}$	4.0×10^6	[m^2/m^3]
TPB density	l_{tpb}	2.0×10^{12}	[m/m^3]
Area-specific current density	i	50, 500	[mA/cm^2]
Anode thickness	L	50	[μm]

6.2.2 Factors influencing on the active thickness

In this chapter, a sensitivity analysis is conducted to investigate the effect of various operating conditions and microstructural parameters of the Ni-YSZ anode on the active thickness. For the efficient analysis, the independent factors that have an influence on the active thickness need to be determined. Since the performance of the electrodes depends on various factors such as overpotential, temperature, microstructure, and gas compositions, the area-specific current density i is generally represented as follows:

$$i = f\left(\eta_t, T, l_{tpb}, \frac{V_{\text{Ni}}}{\tau_{\text{Ni}}}, \frac{V_{\text{YSZ}}}{\tau_{\text{YSZ}}}, \frac{V_{\text{Pore}}}{\tau_{\text{Pore}}}, P_{\text{H}_2}, P_{\text{H}_2\text{O}}\right) \tag{6.1}$$

Since the transport of electrons and gaseous species is much faster than that of oxide ions, the effect of the microstructural parameters $V_{\mathrm{Ni}}/\tau_{\mathrm{Ni}}$ and $V_{\mathrm{Pore}}/\tau_{\mathrm{Pore}}$ can be assumed negligible. Moreover, since the effects of the TPB density and the gas partial pressures are only on the exchange current density (eqs. (3.25) and (3.26)), the effect of the partial pressures is omitted in this study.

$$i = f\left(\eta_t, T, l_{tpb}, \frac{V_{\mathrm{YSZ}}}{\tau_{\mathrm{YSZ}}}\right) \tag{6.2}$$

6.2.3 Voltage losses

For the detailed understandings of the several voltage losses in the anodes, the following averaged values are introduced in this chapter [14]. Local overpotentials are averaged with the weight of the local charge-transfer current i_{tpb}.

$$\overline{\eta}_{act} = \frac{\int_0^L \eta_{act}(x) i_{tpb}(x) dx}{\int_0^L i_{tpb}(x) dx} \tag{6.3}$$

$$\overline{\eta}_{con} = \frac{\int_0^L \eta_{con}(x) i_{tpb}(x) dx}{\int_0^L i_{tpb}(x) dx} \tag{6.4}$$

$$V_{ohm,el} = \frac{\int_0^L \{\phi_{el}(0) - \phi_{el}(x)\} i_{tpb}(x) dx}{\int_0^L i_{tpb}(x) dx} \tag{6.5}$$

$$V_{ohm,io} = \frac{\int_0^L \{\phi_{io}(x) - \phi_{io}(L)\} i_{tpb}(x) dx}{\int_0^L i_{tpb}(x) dx} \tag{6.6}$$

6.3 Active Thickness and Characteristic Length

6.3.1 Active thickness

In this chapter, the active thickness l_{reac} is defined as the thickness of the region from the anode-electrolyte interface where 90% of the total electrochemical reaction takes place (Fig. 6.1).

$$\int_{L-l_{reac}}^{L} i_{tpb} dx = 0.90 \int_0^L i_{tpb} dx \tag{6.7}$$

6.3.2 Characteristic length of the oxide-ion conduction

In this study, the active thickness in the anodes is assumed to be mainly determined by the two factors: oxide-ion conductivity and the electrochemical reaction rate. When the

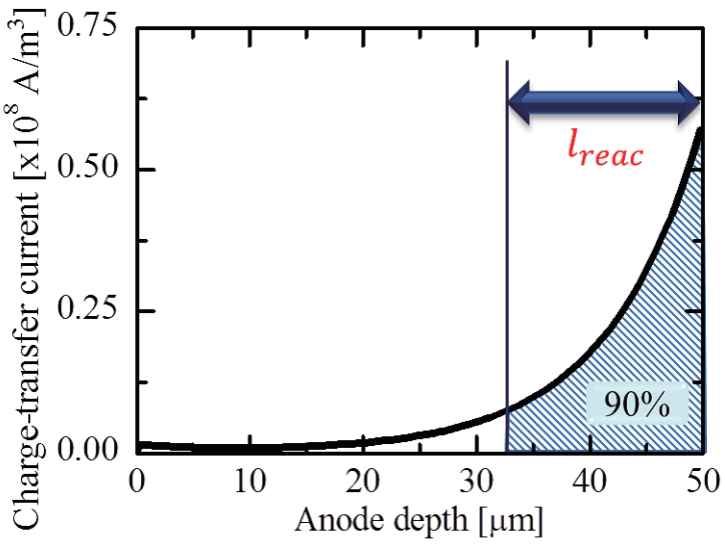

Fig. 6.1. Definition of the active thickness in the SOFC anode.

oxide-ion conductivity is larger, the oxide ion can be transported further from the anode-electrolyte interface, resulting in thicker active thickness. On the other hand, when the electrochemical reaction rate is larger, the supplied oxide ions from the YSZ electrolyte is immediately consumed around the anode-electrolyte interface, resulting in thinner active thickness. The balance between the two factors is essentially important to estimate the active thickness in the anodes. Therefore, by taking the ratio between the two factors, the following parameter is newly introduced:

$$l_{io} = \frac{\sigma_{io}^{\mathrm{eff}}}{i/\eta_t} = \frac{\sigma_{io}^{\mathrm{eff}}\eta_t}{i} \tag{6.8}$$

where i is the area-specific current density and η_t is the anode overpotential. In this study, the l_{io} is named as the characteristic length of the oxide-ion conduction, and the relationships between the active thickness and the characteristic length is investigated through the numerical simulation.

6.4 Results and Discussion

6.4.1 Effect of the current density

For the fundamental understanding of the active thickness, the effect of the area-specific current density on the active thickness is investigated. Fig. 6.2 shows the (a) anode overpotential, (b) active thickness and characteristic length, (c) voltage losses at 800 °C, and (d) voltage losses at 1000 °C. The voltage losses are expressed in percentage to make the comparison easier among different temperature conditions.

The anode overpotential linearly depends on the current density at 1000 °C, while it is non-linear at 800 °C. This tendency was also found in Chapter 3. The trends of the active thickness and the characteristic length also depend on the temperature; they significantly decrease at 800 °C as the current density increases, while they are almost constant at 1000 °C.

The ratio of the voltage losses in Fig. 6.2 (c) and (d) also shows interesting trends. At 1000 °C, the anode overpotential is divided almost equally between the activation loss and the ohmic loss associated with the oxide-ion conduction. On the other hand, at 800 °C, the activation loss becomes prominent in high current density region. This indicates the balance between the charge-transfer resistance and the ohmic resistance is not constant but depends on the current density or overpotential. The reason of this phenomena will be discussed later. The contribution of the ohmic loss associated with the electron conduction is assumed to be negligible in this analysis, therefore, the word of "ohmic loss" is used hereinafter for that associated with the oxide-ion conduction. The contribution of the concentration loss is negligible at 800 °C but increases up to 8% at 1000 °C. This is because the activation and ohmic losses become smaller at higher temperature, while the concentration loss becomes larger according to its definition (eq.(3.24)). Note that there is no significant difference in the distribution of the gas composition in the anode between 800 °C and 1000 °C conditions.

As indicated in the Fig 6.2 (d), when the current density increases in higher temperature, the amount of both the oxide-ion transport through the YSZ phase and the electrochemical reaction per unit TPB increase, keeping the ratio of the voltage losses unchanged. However, the balance between the two factors is lost when the anode overpotential becomes larger than approximately 0.1 V. This is because the charge-transfer resistance associated with the

Butler-Volmer equation is not constant but depends on the anode overpotential in higher overpotential region. At 1000 °C, the local activation overpotential in the vicinity of the anode-electrolyte interface is at most 0.05 V, which indicates the exponent in the Butler-Volmer equation, $F\eta/RT$, is on the order of 0.1. In this situation, the Butler-Volmer equation can be approximated by the following linear formula through the series expansion of the exponential terms:

$$\begin{aligned} i &= i_0 \left\{ \exp\left(\frac{2F}{RT}\eta\right) - \exp\left(-\frac{F}{RT}\eta\right) \right\} \\ &\simeq i_0 \left\{ 1 + \frac{2F}{RT}\eta - \left(1 - \frac{F}{RT}\eta\right) \right\} \\ &= 3i_0 \frac{F}{RT}\eta \end{aligned} \tag{6.9}$$

Therefore the charge-transfer resistance η/i is constant. On the other hand, at 800 °C, the local activation overpotential in the vicinity of the anode-electrolyte interface can reach to 0.20 V, hence, the exponent $F\eta/RT$ becomes on the order of 1. In this situation, the higher order terms in the series expansion of the Butler-Volmer equation cannot be neglected, subsequently, the charge-transfer resistance depends on the activation overpotential. The charge-transfer resistance becomes smaller in higher overpotential region, while the transport resistance of the oxide ions is always independent of the overpotential. The discrepancy in the change rate of the two resistances breaks the balance between the activation loss and the ohmic loss. Due to the smaller charge-transfer resistance in the high overpotential region, the electrochemical reaction preferably occurs rather than the oxide-ion conduction, making the active thickness thinner. This is the reason why the active thickness becomes thinner when the anode overpotential is large.

Similar discussion can be done for the characteristic length. As shown in the Fig. 6.2 (a), the anode overpotential characteristics is non-linear at 800 °C, therefore, the value of i/η_t becomes larger as the current density increases. This results in shortening the characteristic length. On the other hand, since the overpotential characteristics is almost linear at 1000 °C, the value of i/η_t is constant, hence, the characteristic length is also constant.

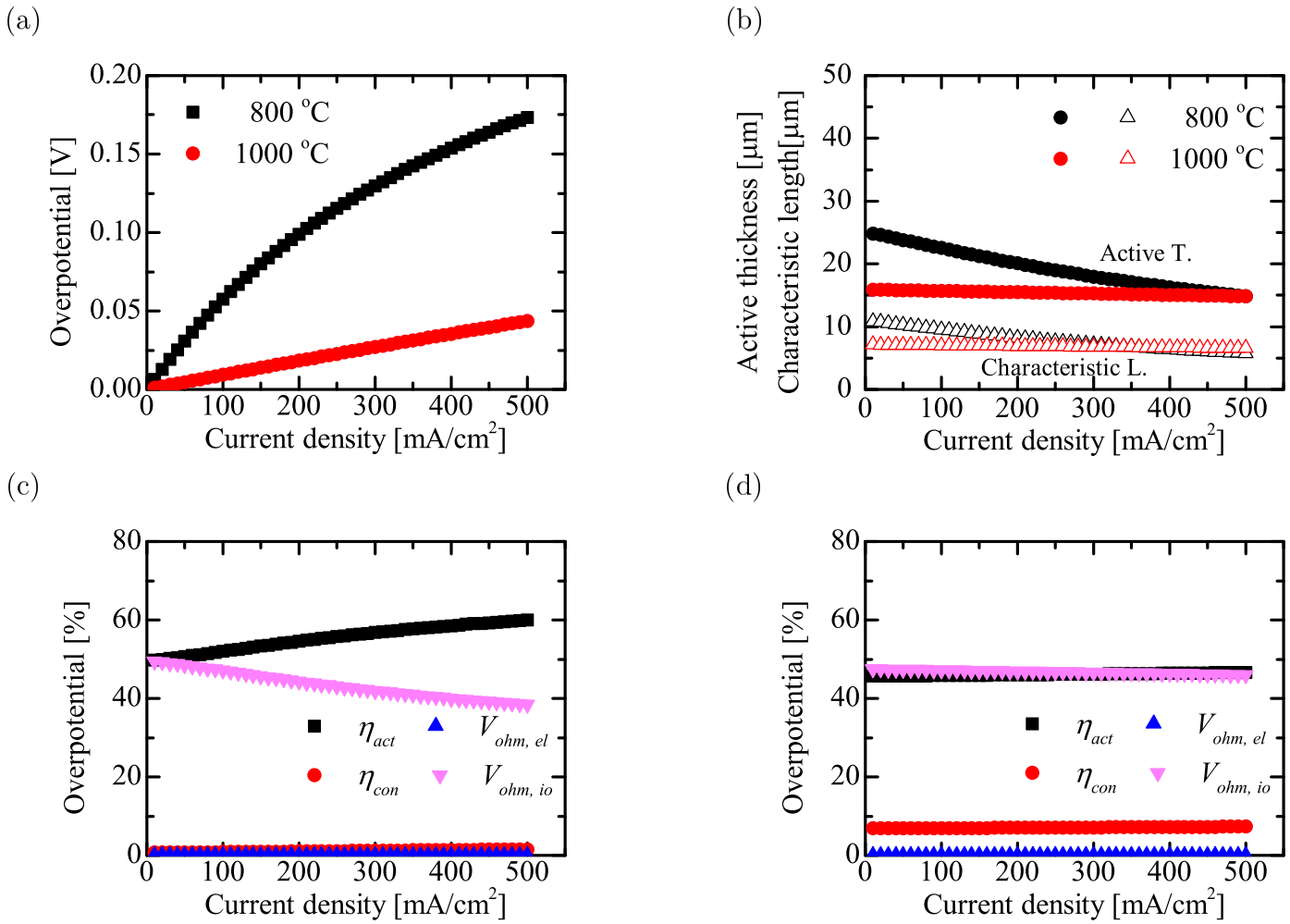

Fig. 6.2. Effect of current density on (a) anode overpotential, (b) active thickness and characteristic length, (b) voltage losses at 800 °C, and (d) voltage losses at 1000 °C.

6.4.2 Effect of the tortuosity factor of the YSZ phase

In order to investigate the effect of the oxide-ion conductivity on the active thickness, the tortuosity factor of the YSZ phase is varied from 1 to 20. In actual electrodes, it is almost impossible to change only the tortuosity factor of the YSZ phase with keeping other microstructural parameters unchanged, such as volume fractions and particle diameters. However, the objective of this analysis is to investigate the effect of the oxide-ion conductivity through the anode structure; varying the value of the tortuosity factor is just one of the possible numerical procedures. The change of the conductivity can be also associated with using other electrode materials such as gadolinia-doped ceria (GDC) instead of YSZ. Moreover, the structural change in the YSZ phase caused by long-term operation of SOFCs, such as sintering and cracking, can be represented by the change of the tortuosity factor.

Fig. 6.3 shows the effect of the YSZ tortuosity factor on the (a) anode overpotential, (b) characteristic length and active thickness, (c) voltage losses at 50 mA/cm^2, and (d) voltage losses at 500 mA/cm^2 at 800 °C. Fig. 6.4 shows those at 1000 °C.

As the tortuosity factor becomes larger, the effective oxide-ion conductivity decreases, which results in larger anode overpotential. At the same time, the active thickness becomes thinner. The characteristic length also becomes shorter, which indicates the amount of decrease in the effective ion conductivity is larger than the increase in the overpotential. The effect of the tortuosity factor is larger when the value is smaller than about 5; similar behavior was observed in the sensitivity analysis conducted in Chapter 3 (Fig. 3.5).

At 1000 °C, the anode overpotential is almost equally divided between the activation loss and the ohmic loss regardless of the current density. On the other hand, at 800 °C, the activation loss becomes prominent especially at higher current density. This phenomena can also be explained by the non-linearity of the Butler-Volmer equation as discussed in the previous section. The anode overpotential at 800 °C with 500 mA/cm^2 load is more than 0.1 V, where the charge-transfer resistance strongly depends on the overpotential. In this situation, the electrochemical reaction preferably occurs rather rather than the oxide-ion conduction, resulting in thinner active thickness. In the other cases, the overpotential is at most 0.05 V so that the balance between the reaction and the conduction is kept unchanged.

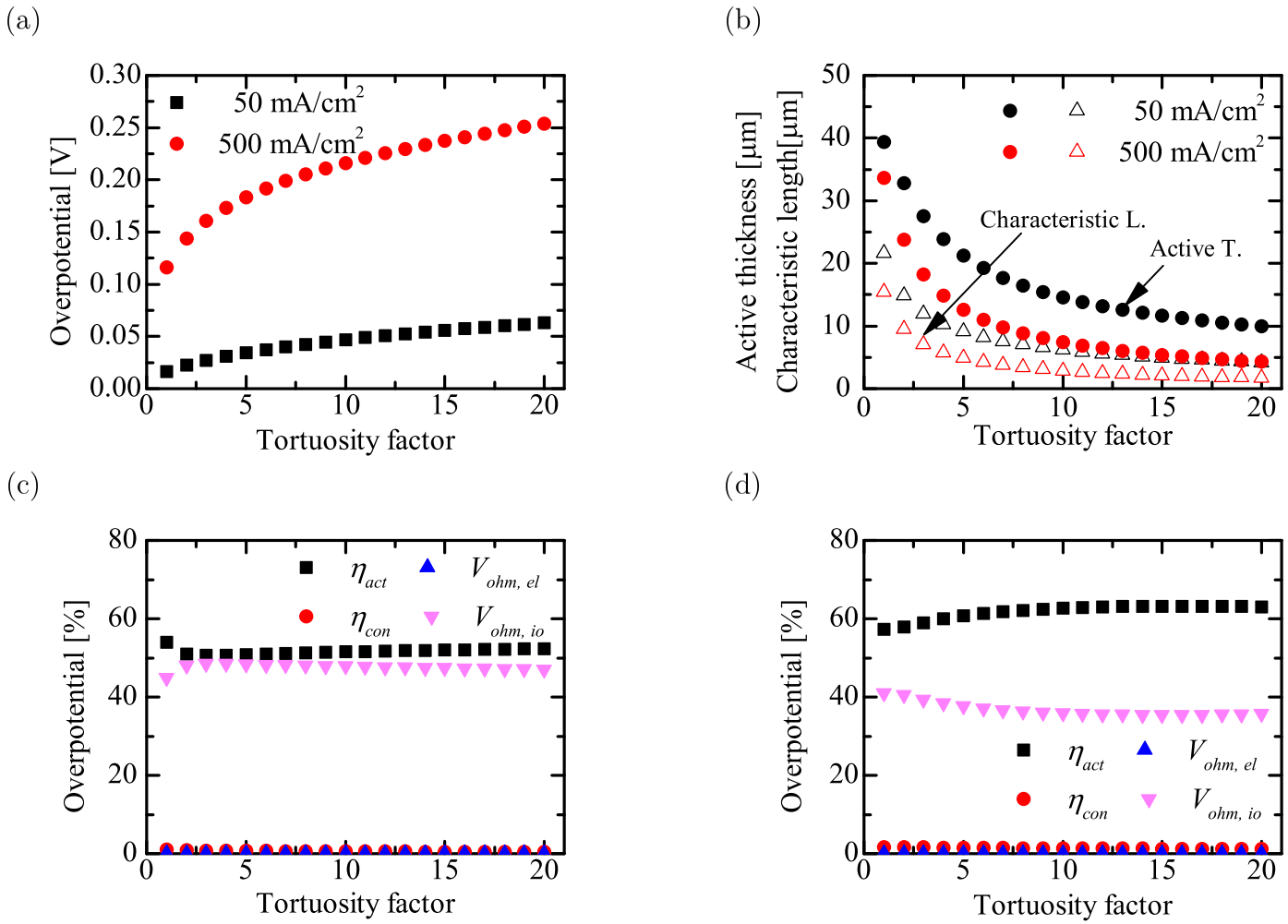

Fig. 6.3. Effect of the tortuosity factor of the YSZ phase on (a) anode overpotential, (b) active thickness and characteristic length, (b) voltage losses at 50 mA/cm^2, and (d) voltage losses at 500 mA/cm^2. $T = 800$ °C.

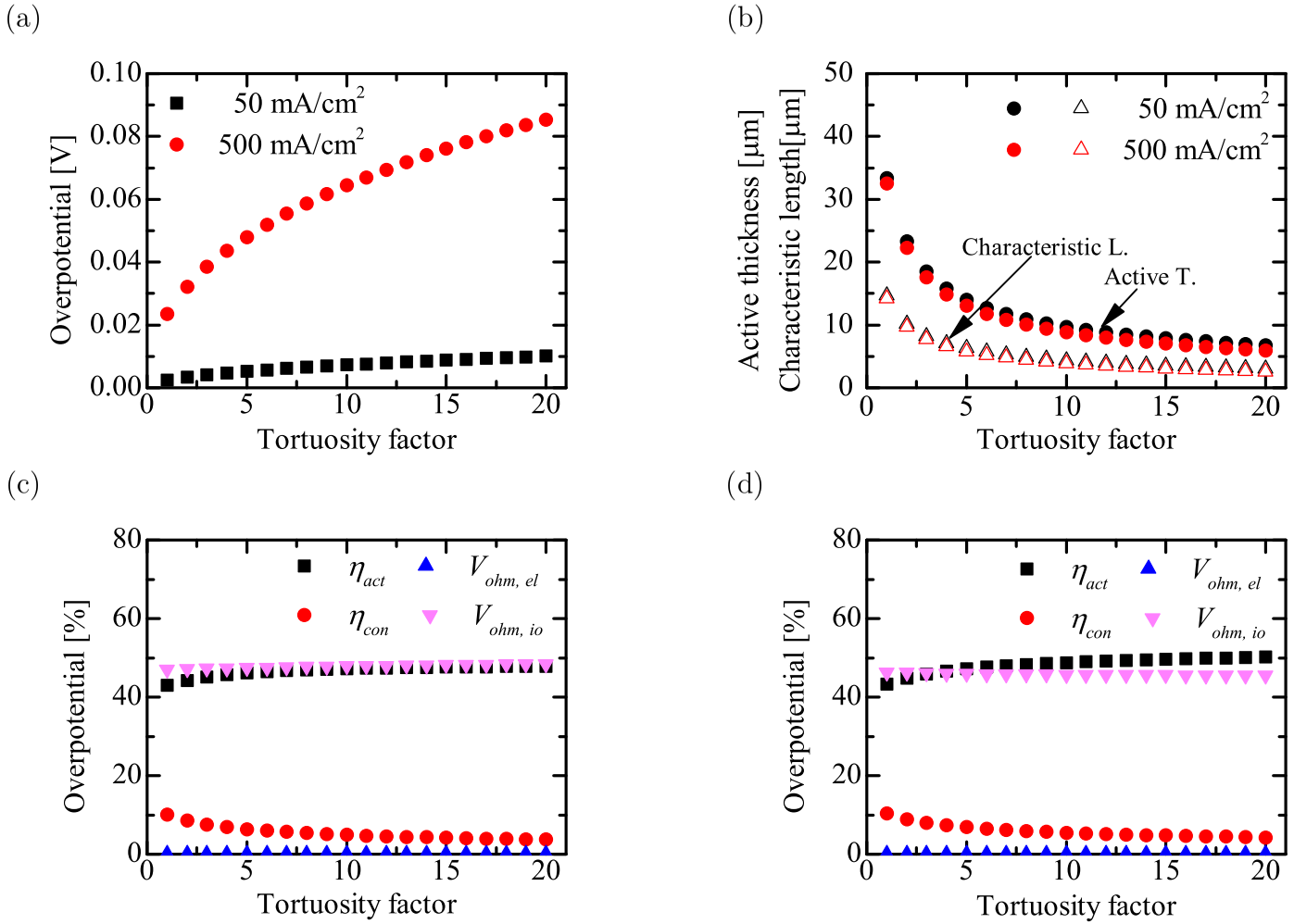

Fig. 6.4. Effect of the tortuosity factor of the YSZ phase on (a) anode overpotential, (b) active thickness and characteristic length, (c) voltage losses at 50 mA/cm^2, and (d) voltage losses at 500 mA/cm^2. $T = 1000$ °C.

6.4.3 Effect of the TPB density

Next, the TPB density of the anode is varied from 0.1 to 4.0 μm/μm^3 to investigate the effect of the electrochemical reaction rate on the active thickness. This investigation can be interpreted as an attempt varying the exchange current density i_0 in the Butler-Volmer equation because the TPB density is only included in the equation. Therefore, the effect of other factors that are related only with the exchange current density, such as the gas partial pressures, can be deduced from the results shown below. Change of the TPB density, decrease in particular, can also be attributed to the morphologic change of the porous microstructure, such as those caused by sintering and poisoning; the results can be used to predict how the active thickness varies when the TPB density changes during the long-term operation of SOFCs.

Fig. 6.5 shows the effect of the TPB density on the (a) anode overpotential, (b) characteristic length and active thickness, (c) voltage losses at 50 mA/cm^2, and (d) voltage losses at 500 mA/cm^2 at 800 °C. Fig. 6.6 shows those at 1000 °C.

As the TPB density increases, the anode overpotential decreases on the constant current condition. Since larger TPB density indicates sufficient reaction site in the vicinity of the anode-electrolyte interface, the active thickness decreases as the TPB density becomes larger. The effect of the TPB density on the active thickness is prominent when the value is smaller than about 1 μm/μm^3. In other word, the active thickness becomes significantly thicker when the TPB density decreases below 1 μm/μm^3. This may become a critical issue when the TPB density decreases due to the morphologic change during the operation.

At 800 °C with 500 mA/cm^2 load, the anode overpotential is over 0.15 V, where the non-linearity of the Butler-Volmer equation appears. The contribution of the activation loss becomes larger in the voltage loss and the active thickness becomes significantly thinner. In the other conditions, the overpotentials are mostly on the order of 0.01 V except at lower TPB density region ($l_{tpb} < 1\mu$m/μm^3) so that the anode overpotential is equivalently shared between the activation loss and the ohmic loss.

The characteristic length becomes shorter because of the decrease in the anode overpotential.

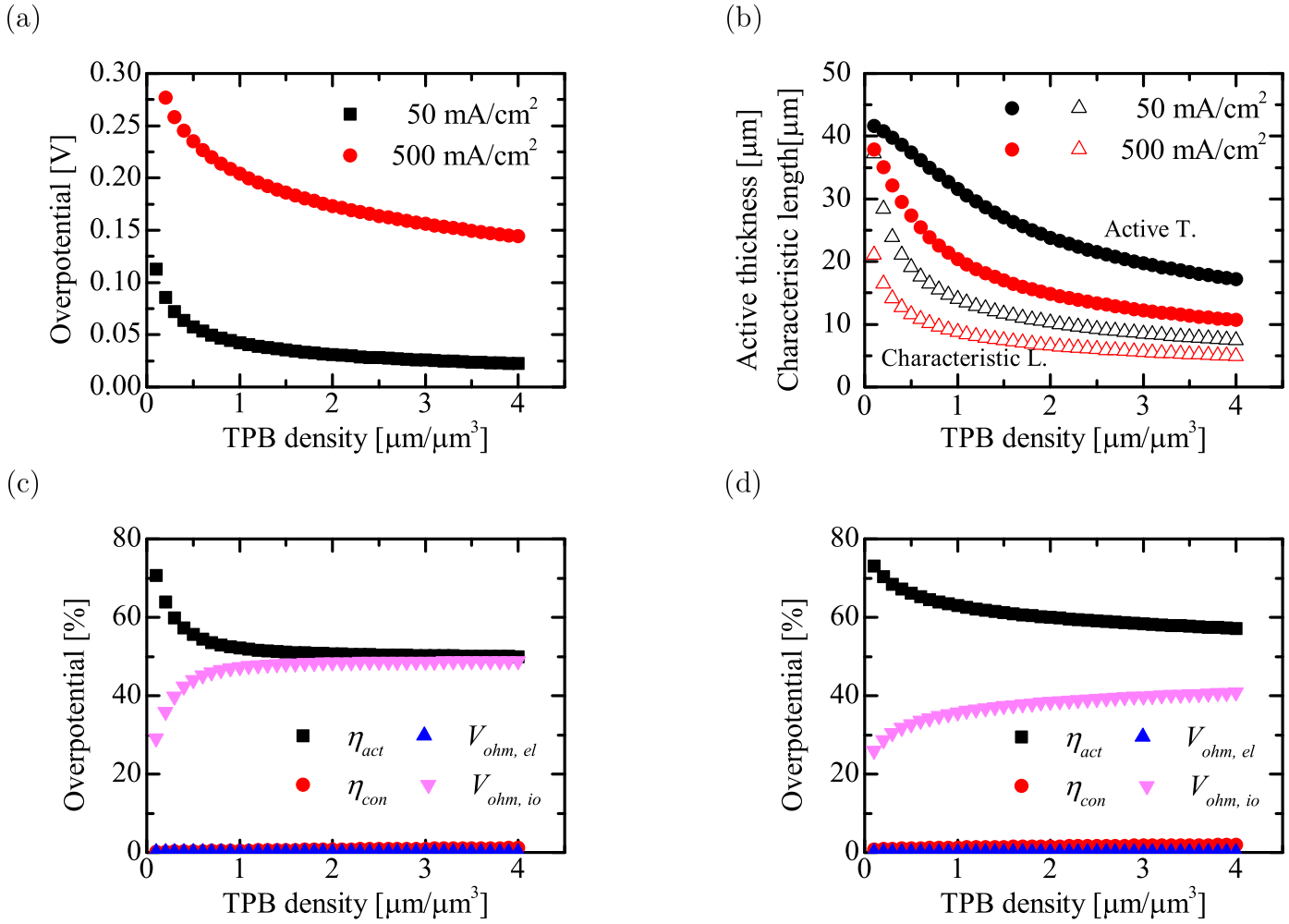

Fig. 6.5. Effect of the TPB density on (a) anode overpotential, (b) active thickness and characteristic length, (c) voltage losses at 50 mA/cm^2, and (d) voltage losses at 500 mA/cm^2. $T = 800$ °C.

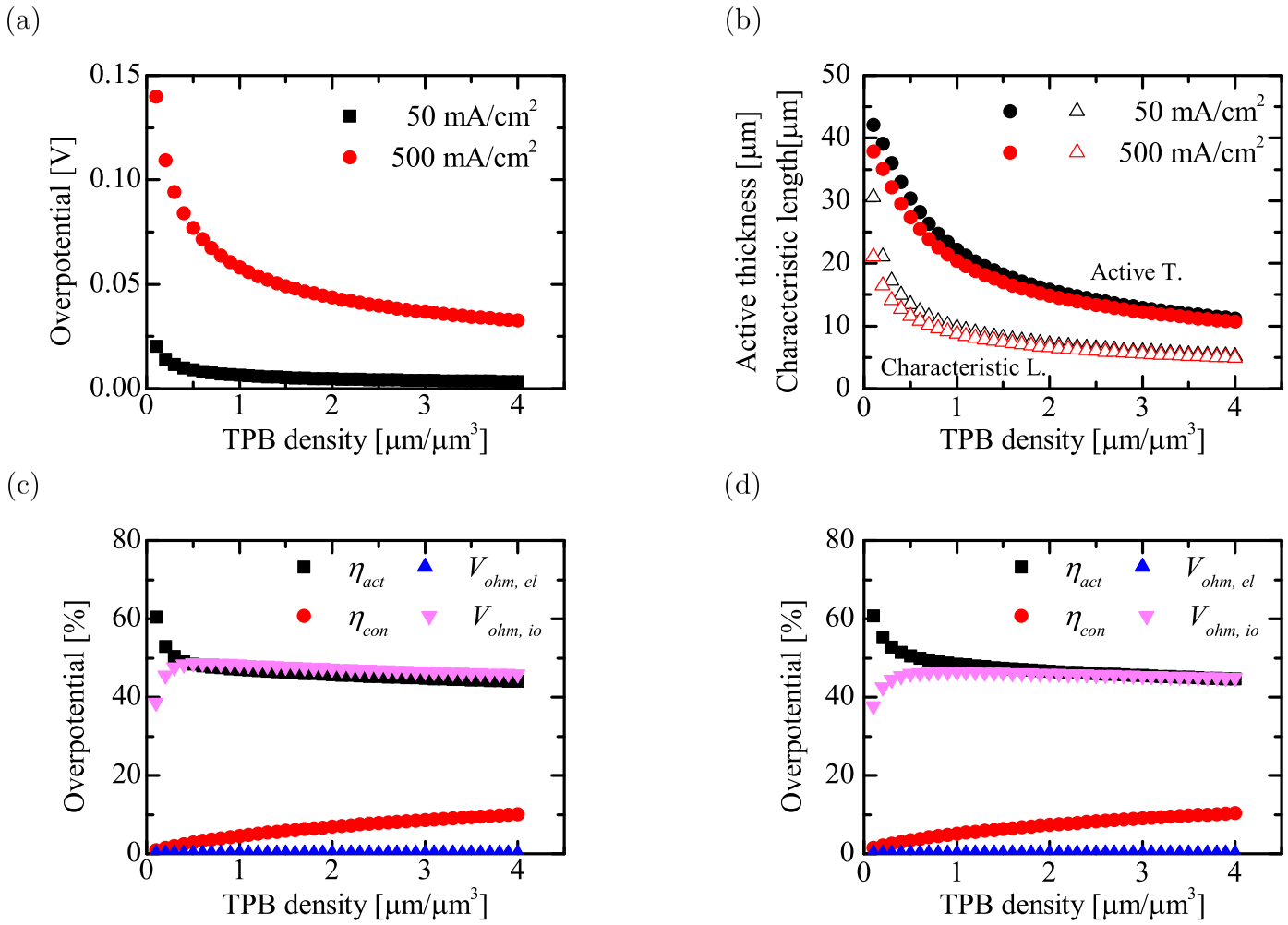

Fig. 6.6. Effect of the TPB density on (a) anode overpotential, (b) active thickness and characteristic length, (c) voltage losses at 50 mA/cm^2, and (d) voltage losses at 500 mA/cm^2. $T = 1000$ °C.

6.4.4 Effect of the temperature

Finally, the anode temperature is varied from 700 to 1100 °C to investigate the effect of the temperature on the active thickness. Both the oxide-ion conductivity and the electrochemical reaction rate change in this analysis.

Fig. 6.7 shows the effect of the temperature on the (a) anode overpotential, (b) characteristic length and active thickness, (c) voltage losses at 50 mA/cm^2, and (d) voltage losses at 500 mA/cm^2.

As the temperature increases, both the oxide-ion conductivity and the electrochemical reaction rate are improved, which significantly lowers the anode overpotential. The effect of these two factors on the active thickness is opposite from each other: expanding effect by larger oxide-ion conductivity, and shrinking effect by higher electrochemical reaction rate. The balance between the two effects determines the active thickness.

When the current density is 50 mA/cm^2, the total anode overpotential is divided almost equally between the activation loss and the ohmic loss. The active thickness decreases as the temperature increases. However, in the range of temperature from 700 to 800 °C, the activation overpotential reaches about 0.1 V, which slightly shifts the balance of the voltage losses to the activation loss, making the active thickness thinner. On the other hand, when the current density is 500 mA/cm^2, the overpotential is more than 0.1 V below 900 °C. This emphasizes the non-linearity of the Butler-Volmer equation, resulting in more electrochemical reaction in the vicinity of the anode-electrolyte interface. Consequently, the activation loss becomes prominent and the active thickness becomes thinner.

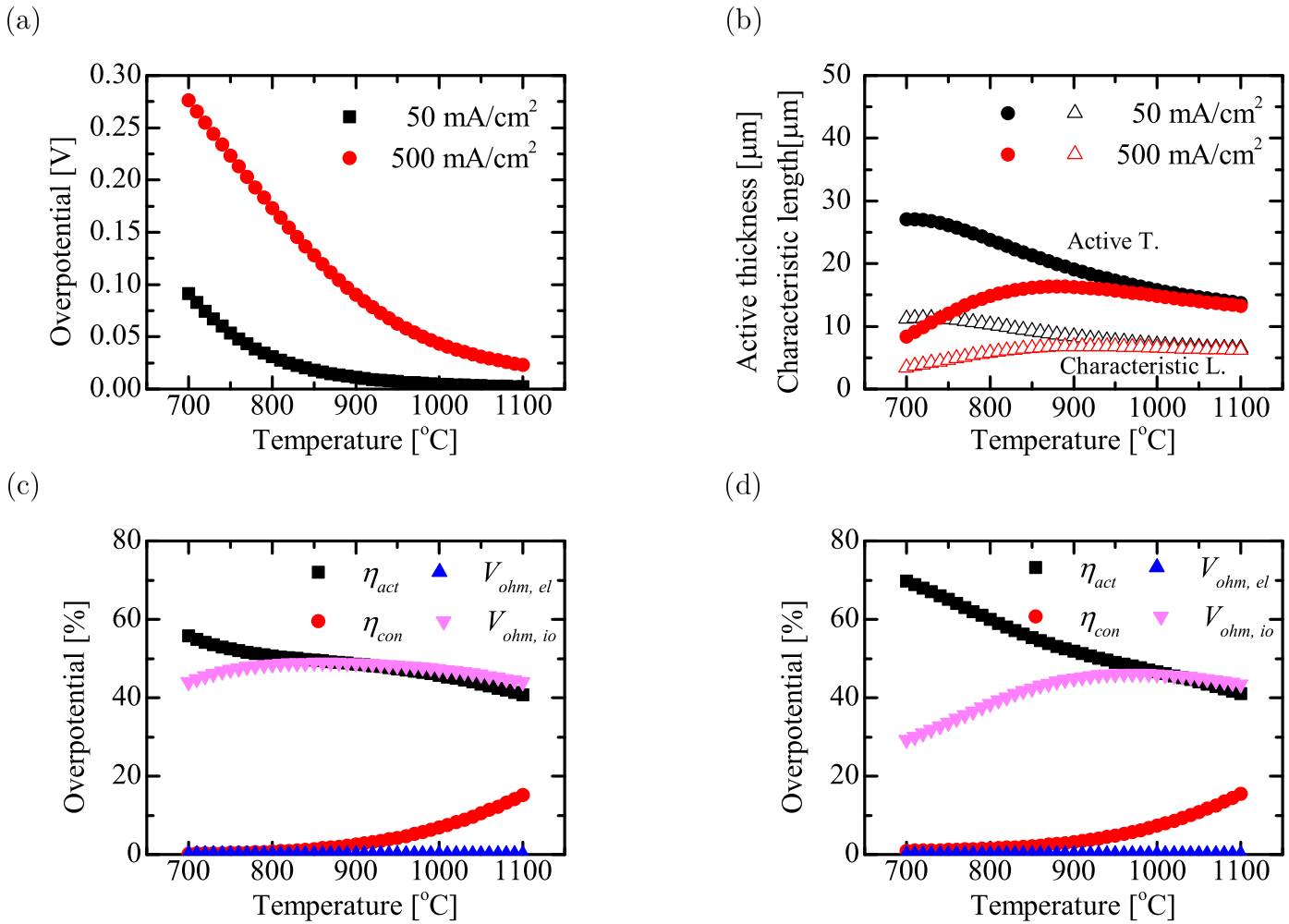

Fig. 6.7. Effect of the temperature on (a) anode overpotential, (b) active thickness and characteristic length, (c) voltage losses at 50 mA/cm^2, and (d) voltage losses at 500 mA/cm^2.

6.4.5 Relationships between the active thickness and the characteristic length

Fig. 6.8 shows the relationships between the active thickness and the characteristic length. The active thickness is found to have a linear dependency on the characteristic length. Moreover, the lines are almost at the same position regardless of the varied parameters. Although the active thickness depends on various factors, its tendency can be ordered using the characteristic length introduced in this chapter. The deviation from the linear line in the region of large characteristic length is attributed to the fact that the anode thickness is 50 μm.

The regression line of the data points over $0 < l_{io} < 15$ is as follows:

$$l_{90} = 2.27 l_{io} + 0.466 \tag{6.10}$$

where the mean square deviation is 0.983.

This result indicates the possibility that the characteristic length can be used as a designing parameter of SOFC electrodes, with which to predict and control the active thickness in the electrodes.

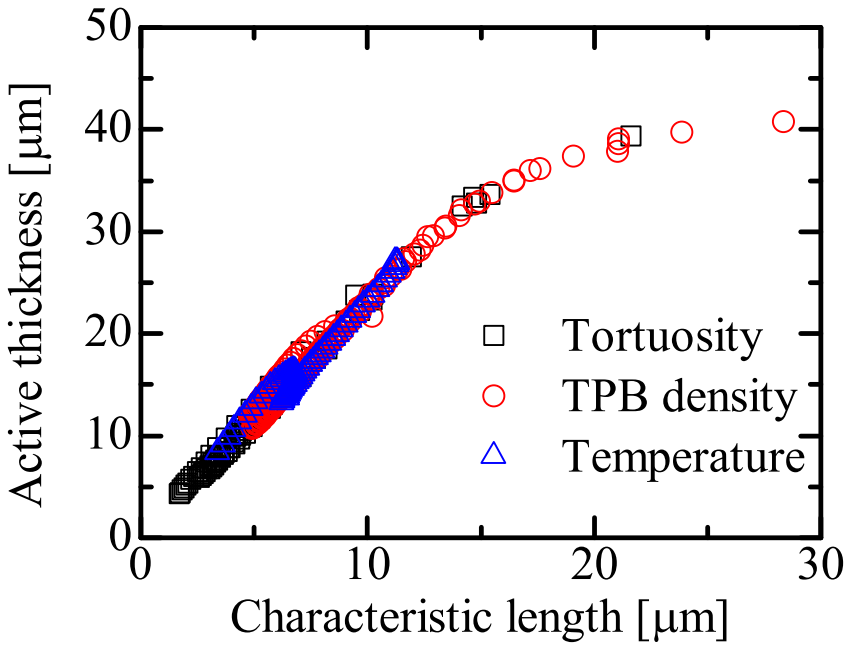

Fig. 6.8. Relationships between the active thickness and the characteristic length.

6.5 Conclusions

One-dimensional numerical simulation with the homogenized porous structure model is conducted to estimate the active thickness in the Ni-YSZ anode. Effect of the microstructure and the operating conditions is systematically investigated. The characteristic length of the oxide-ion conduction is introduced by taking the ratio between the two major factors determining the active thickness: the effective oxide-ion conductivity and the electrochemical reaction rate. Main conclusions drawn in the present chapter can be stated as follows:

1. The behavior of the active thickness strongly depends on the anode overpotential. If the anode overpotential is smaller than about 0.1 V, where the Butler-Volmer equation can be approximated by a linear function, the charge-transfer resistance and the ion-conduction resistance is independent of the overpotential. In this situation, the total anode overpotential is divided almost equally between the activation loss and the ohmic loss associated with the oxide-ion conduction.

2. If the anode overpotential is larger than about 0.1 V, the non-linearity of the Butler-Volmer equation appears; the charge-transfer resistance becomes smaller as the overpotential becomes larger. In this situation, the electrochemical reaction preferably occur rather than the oxide-ion conduction, shifting the balance of the voltage losses to the activation loss, subsequently, the active thickness becomes significantly thinner. Higher anode overpotential can be caused by various operating conditions and microstructural parameters: high current load, high tortuosity factor of the YSZ phase, low TPB density, and low temperature.

3. Under the anode overpotential smaller than 0.1 V, the behavior of the active thickness is as follows. (a) Smaller tortuosity factor of the YSZ phase makes the active thickness thicker because the oxide ion can be transported further from the anode-electrolyte interface. This effect is prominent when the tortuosity factor is less than 5. (b) Larger TPB density makes the active thickness thinner because the oxide ions supplied from the electrolyte can be immediately consumed at the TPB in the vicinity of the anode-electrolyte interface. This effect is prominent when the TPB density is less than 1 μm/μm^3. (c) Larger temperature makes the active thickness significantly thinner .

4. The active thickness is found to have a linear dependency on the characteristic length; therefore, the characteristic length is possibly used for designing parameter in the fabrication process of SOFC electrodes.

Bibliography

[1] M. Juhl, S. Primdahl, C. Manon, M. Mogensen, Performance/Structure Correlation for Composite SOFC Cathodes, *Journal of Power Sources* **61** (1996) 173–181.

[2] S. Primdahl, M. Mogensen, Oxidation of Hydrogen on Ni/Yttria-Stabilized Zirconia Cermet Anodes, *Journal of The Electrochemical Society* **144** (1997) 3409–3419.

[3] M. Brown, S. Primdahl, M. Mogensen, Structure/Performance Relations for Ni/Yttria-Stabilized Zirconia Anodes for Solid Oxide Fuel Cells, *Journal of The Electrochemical Society* **147** (2000) 475–485.

[4] J. Kong, K. Sun, D. Zhou, N. Zhang, J. Mu, J. Qiao, Ni-YSZ Gradient Anodes for Anode-Supported SOFCs, *Journal of Power Sources* **166** (2007) 337–342.

[5] H. Moon, SD. Kim, E.W. Park, S.H.Hyun, H.S. Kim, Characteristics of SOFC Single Cells with Anode Active Layer via Tape Casting and Co-firing, *International Journal of Hydrogen Energy* **33** (2008) 2826–2833.

[6] K. Chen, X. Chen, Z. Lu, N. Ai, X. Huang, W. Su, Performance of an Anode-Supported SOFC with Anode Functional Layers, *Electrochimica Acta* **53** (2008) 7825–7830.

[7] S. Sunde, Monte Carlo Simulations of Polarization Resistance of Composite Electrodes for Solid Oxide Fuel Cells, *Journal of The Electrochemical Society* **143** (1996) 1930–1939.

[8] S.H. Chan, Z.T. Xia, Anode Micro Model of Solid Oxide Fuel Cell, *Journal of The Electrochemical Society* **148** (2001) A388–A394.

[9] K. Yuan, Y. Ji, J.N. Chung, Physics-Based Modeling of a Low-Temperature Solid Oxide Fuel Cell with Consideration of Microstructure and Interfacial Effects, *Journal of Power Sources* **194** (2009) 908–919.

[10] Q. Cai, C.S. Adjiman, N.P. Brandon, Investigation of the Active Thickness of Solid Oxide Fuel Cell Electrodes Using a 3D Microstructure Model, *Electrochimica Acta* **56** (2011) 10809–10819.

[11] N. Shikazono, D. Kanno, K. Matsuzaki, H. Teshima, S. Sumino, N. Kasagi, Numerical Assessment of SOFC Anode Polarization Based on Three-Dimensional Model Microstructure Reconstructed from FIB-SEM Images, *Journal of The Electrochemical Society* **157** (2010) B665–B672.

[12] K. Matsuzaki, N. Shikazono, N. Kasagi, Three-Dimensional Numerical Analysis of Mixed Ionic and Electronic Conducting Cathode Reconstructed by Focused Ion Beam Scanning Electron Microscope, *Journal of Power Sources* **196** (2011) 3073–3082.

[13] M. Kishimoto, H. Iwai, M. Saito, H. Yoshida, *Journal of Power Sources* **196** (2011) 4555–4563.

[14] A. Konno, H. Iwai, M. Saito, H. Yoshida, A corrugated mesoscale structure on electrode-electrolyte interface for enhancing cell performance in anode-supported SOFC, *Journal of Power Sources* **196** (2011) 7442–7449.

Chapter 7

Conclusions

7.1 Conclusions

In Chapter 2, three-dimensional observation and the following image processing and quantification techniques were developed and employed to the Ni-YSZ anodes of SOFCs. The three-dimensional microstructure of the porous anodes were directly observed with the dual-beam FIB-SEM technique. Then the quantification techniques were developed to characterize the porous microstructure. The anodes with four different compositions were examined and the fundamental understandings of the complex nature of the porous anode were obtained. The structure size available for the quantitative analysis was more than 10 μm^3. Use of the low acceleration voltage of the electron beam (1-2 kV) and the in-lens secondary electron detector provided the clear contrast between the three phases. Infiltration with epoxy resin was effective to eliminate the background effect from the cross-sectional images. The volume fraction, percolation probability, tortuosity factor, and particle/pore size were obtained with in-house C-language-based program, while the TPB density and the surface information were quantified using the commercial image processing software Avizo. Error analysis was conducted for the quantification of the tortuosity factor and the TPB density and showed the number of voxels required to resolute the characteristic structure of the porous anode: 20 for the tortuosity factor and 10 for the TPB density. Analysis on the anodes with four different compositions provided fundamental insights on the composite anode microstructure. For example, low volume fraction with large particle size of a phase resulted in sparse distribution of the phase, making the connectivity worse. On the other

hand, low volume fraction with small particle size of a phase resulted in complex porous configuration even though the phase was spatially well-connected. Tortuosity factor, which was important to consider various transport phenomena in porous materials, was affected by other microstructural parameters such as percolation probability and surface-to-volume ratio.

In Chapter 3, one-dimensional numerical simulation of the SOFC anode was conducted considering the various transport phenomena in the porous electrode, which were linked by the electrochemical reaction at the TPB. The microstructural parameters of the porous anode quantified in Chapter 2 were applied to the model to evaluate the effective transport coefficients and the electrochemical reaction rate. Numerical results were compared with the experimental counterparts under various operating conditions to validate the proposed model. For the fundamental understanding of the effects of the microstructure on the overall anode performance, sensitivity analysis was conducted varying the microstructural parameters, and the rate-limiting process in the anode was identified.

In Chapter 4, sub-grid-scale models used for the three-dimensional numerical analysis in SOFC electrodes were developed. The main function of the SGS model was to maintain the quality of the voxel-based structural information in a resampled structure used as calculation grid systems by considering the structure with a characteristic scale that is smaller than the grid size. Improvement of the simulation accuracy and reduction of the computation load can be expected with the SGS models. Four types of SGS models were developed and their effect and applicability were investigated. They were featured by (1) volume conservation, (2) interfacial connectivity, (3) power law with a constant power index, and (4) power law with an adaptive power index, respectively. The validity of the proposed SGS models were investigated through the diffusion simulation. By introducing the ratio between the grid size and the characteristic scale of the porous structure as an adoptive power index (SGS4), the structural complexity in the grids was successfully evaluated in wide range of grid sizes. The SGS4 exerted its effect preferably in accordance with the grid size.

In Chapter 5, Ni-YSZ composite anodes with three different compositions were examined and compared through the electrochemical measurement, microstructural analysis, and nu-

merical simulation. The porous microstructure of the examined anodes was directly observed using the FIB-SEM, and used for the microstructural investigation and the three-dimensional simulation with the aid of the SGS models developed in Chapter 4. It was found that the amount and distribution of the effective TPB was essentially important to explain the anode performance, instead of the commonly-used total TPB density. The Ni:YSZ = 30:70 anode showed significantly lower performance because of the higher ohmic resistance compared with the others. This was because the low Ni volume content caused poor Ni connectivity, which shifted the effective TPB far away from the anode-electrolyte interface. On the other hand, the Ni:YSZ = 70:30 anode showed similar performance to that of the Ni:YSZ = 50:50 anode, even though they were expected to have different porous structure. This was because the sufficient amount of the effective TPB was distributed around the anode-electrolyte interface in the both anodes. Although the connectivity of the YSZ phase in the Ni:YSZ = 70:30 anode was poor, it was enough to secure the oxide-ion transport from the electrolyte to the TPB located close to the anode-electrolyte interface. The three-dimensional numerical simulation of the anode overpotential using the obtained porous structure qualitatively reproduced the experimental results. Combined with the distribution of the charge-transfer current and the effective TPB, the simple optimizing policy for the Ni-YSZ anode was proposed.

In Chapter 6, one-dimensional numerical simulation with homogenized porous structure model was conducted to evaluate the active thickness in the Ni-YSZ anode. Effect of the microstructure and the operating conditions was systematically investigated. The non-linearity of the Butler-Volmer equation used for the electrochemical reaction model had a significant influence on the behavior of the active thickness when the anode overpotential is over 0.1 V. The characteristic length of the oxide-ion conduction was newly introduced by taking the ratio between the two major factors determining the active thickness: the effective ion conductivity and the electrochemical reaction rate. The active thickness was found to have a linear dependency on the characteristic length; therefore, the characteristic length is possibly used for a designing parameter in the fabrication process of SOFC electrodes.

7.2 Suggestions for future works

In this thesis, numerical model that considers the various transport phenomena and the electrochemical reaction in the anode is proposed and applied to the investigation of the states of the anode, from which several optimization policies for the porous microstructure are proposed. However, in order to improve the accuracy and to expand the applicability of the model, various physical and chemical processes with much wider scale need to be considered.

The use of the SGS models can make it possible to precisely predict the transport phenomena inside the complex porous materials. However, the electrochemical reaction model used in this study has more to be improved. As discussed in Chapter 3, the model is not able to predict the experimental results of the anode overpotentials under high humidified or low temperature conditions. This can be attributed to the fact that the model simplified the electrochemical reaction around the TPB to the overall reaction. In reality, the electrochemical reaction in the anodes consists of a group of various elementary heterogeneous reactions such as the adsorption of the gas molecules on the solid surface, dissociation to atoms, charge transfer, and desorption from the solid surface; the overall reaction model assumes that one of the elementary reactions is rate-limiting the whole reaction. However, the rate-limiting process may depend on the operating conditions such as temperature and gas compositions. Therefore, for the accurate evaluation of the electrochemical reaction rate, it is essentially important to consider the elementary chemical reactions at the atom/molecule scale.

At the same time, the calculation domain is required to be expanded to the milli-scale order so that it can represent the distribution of the cell temperature and gas compositions along the cells. In the practical operation of the SOFCs, hydrocarbons are often used for the fuel as well as hydrogen. In such a case, a lot more chemical and physical processes get involved in the phenomena in the cells, such as steam reforming of hydrocarbons, electrochemical oxidation of hydrogen and carbon mono-oxide, and the cooling effect by the air flow. These phenomena makes the states of the cells significantly complicated, and often results in uneven distributions of the cell temperature and the gas compositions, which has a negative impact on the stable operation of SOFCs. For example, solid carbon formation in the anodes is quite sensitive to the fuel compositions; more carbon may form if steam con-

tent is lower. Since the steam is consumed through the steam reforming of methane, which mainly occurs on the upstream of the cells, carbon may preferably form on the downstream of the cells. The carbon deposited in the anode blocks the TPB and inhibits the diffusion through the pore phase, decreasing the anode performance. Such phenomena can only be predicted through the cell-scale analysis.

Therefore, the multi-scale modeling of the SOFC electrodes/cells is strongly required for improving the simulation accuracy and expanding its applicabilities; the linkage between atom/molecular-scale chemical reactions, micro-scale transport in porous material, and milli-scale distributions on the cells needs to be emphasized. Cooperation between wide variety of scientific fields such as material, (electro)chemistry, and mechanical engineering is essentially important to accomplish this challenging issue.

Nomenclature

A	pre-exponential factor	
d_h	hydraulic diameter	m
d_p	mean pore diameter	m
D_{lm}	molecular diffusion coefficient	$m^2\ s^{-1}$
D_K	Knudsen diffusion coefficient	$m^2\ s^{-1}$
E	electric potential	V
F	Faraday constant	$C\ mol^{-1}$
i	area-specific current density	$A\ m^{-2}$
i_{tpb}	charge-transfer current density	$A\ m^{-3}$
i_0	exchange current density per unit volume	$A\ m^{-3}$
$i_{0,\mathrm{tpb}}$	exchange current density per unit TPB length	$A\ m^{-1}$
k_1, k_2, k_3, k_4	mixture diffusion coefficient	$m^2\ s^{-1}$
K	permeability	m^2
l_{io}	characteristic scale of oxide-ion conduction	m
l_{reac}	active thickness	m
l_{tpb}	TPB density	$m\ m^{-3}$
L	anode thickness (Chapter 3, 5, 6)	m
	characteristic scale (Chapte 4)	m
L_{grid}	average grid size (Chapter 4)	m
M	molecular weight	kg
N	molar flux	$mol\ m^{-2}\ s^{-1}$
n	number of electron	
P	pressure	Pa
Q	percolation probability	

$\langle r^2 \rangle$	mean square displacement	m^2
R	gas constant	J mol^{-1} K^{-1}
S	surface area	m^2
(S/V)	surface-to-volume ratio	m^2 m^{-3}
T	temperature	K
V	volume fraction	
Vol	volume	m^3
X	molar ratio	

Greek symbols

γ	Bruggeman factor	
Γ	general transport coefficient	
Δx, Δy, Δz	grid size	m
η	overpotential	V
λ	decay constant	
μ	viscosity	Pa s
σ	conductivity	S m^{-1}
Σv	diffusion volume	m^3
τ	tortuosity factor	
Φ, ϕ	electric potential	V
φ	arbitrary potential	

Subscripts

act	activation
ave	average
con	concentration
el	electron
io	ion
K	Knudsen
t	total
tpb	three-phase boundary

0	standard state
1	hydrogen
2	steam

Superscripts

bulk	bulk material or bulk fluid
eff	effective value in porous media
eq	equilibrium
local	local value defined at a grid
V	volumetric